

# PATTERN FORMATION IN NONEQUILIBRIUM STATISTICAL PHYSICS

by

**Ellák Somfai**

A dissertation submitted in partial fulfillment  
of the requirements for the degree of  
Doctor of Philosophy  
(Physics and Scientific Computing)  
in The University of Michigan  
1999

Doctoral Committee:

Professor Leonard M. Sander, Chairman  
Associate Professor Bradford G. Orr  
Professor Byron P. Roe  
Assistant Professor Alberto G. Rojo  
Professor Robert M. Ziff

# ABSTRACT

PATTERN FORMATION IN NONEQUILIBRIUM STATISTICAL PHYSICS

by  
Ellák Somfai

Chairman: Leonard M. Sander

In this thesis we explore problems in surface- and diffusion limited growth.

Molecular beam epitaxy, the technique used to grow structures on crystal surfaces, is studied with computer simulations. Our focus is the multilayer stage of this process: how the growth conditions affect the evolution of the forming mounds. We also studied heteroepitaxial systems, where the elastic effects significantly change the growth process, resulting in unusual phenomena like quantum dots.

The second area of research is the evolution of river networks. We propose a coarse grained theory, coupling the equation of the surface erosion with the conservation law of surface water flow. Computer simulation of the model produce patterns which show the statistical properties of natural rivers.

Lastly, we study diffusion limited aggregation (DLA), the discrete model of Laplacian growth. Using DLAs grown in wedge geometry, we show the existence of angular building blocks. In a different approach, using conformal maps, we study the relation between the scaling properties of the model and the Laurent expansion of the map.

## ACKNOWLEDGEMENTS

First of all I would like to thank Len Sander, my thesis advisor, for helping and supporting me throughout my years in Ann Arbor. I very much enjoyed working under his guidance, his way of approach to problems and his interest greatly shaped my thinking.

I also thank Brad Orr for advising me in the research presented in Chapter 3. I thank my collaborators, Benny Davidovitch, George Hentchel, Zeev Olami and Dave Kessler for their joint efforts, and especially Itamar Procaccia; I am indebted for his help, encouragement and enlightening conversations. I thank the people in the Weizmann Institute for hospitality, where we did the research presented in Chapter 6.

I thank my fellow grad students, Ji Li, Chris Orme, Radu Manuca and Chris Warren for interesting and helpful conversations. I wish to thank Brad Orr, Byron Roe, Alberto Rojo and Bob Ziff for being members of my dissertation committee and helping to clarify various points in the thesis.

I am thankful to Tamás Vicsek, my diploma advisor, who gave me a strong start on this field. I thank my parents and teachers who oriented me towards science. And above all I thank my wife Ani Sinkovics for her determination seeking the truth, her continuous encouragement and love ♡.

My work was supported by NSF grant DMR 9420335, DOE grant DEFG-02-95ER-45546, and the Rackham Predoctoral Fellowship.

# TABLE OF CONTENTS

<b>Acknowledgements</b> . . . . .	<b>ii</b>
<b>List of Figures</b> . . . . .	<b>v</b>
<b>Chapters</b>	
<b>1. Introduction</b> . . . . .	<b>1</b>
1.1 Overview . . . . .	1
1.2 Fractals and scale-invariance in surface growth . . . . .	2
1.3 Molecular beam epitaxy . . . . .	3
1.4 Scale-invariance in geomorphological processes . . . . .	4
1.5 Laplacian growth and diffusion-limited aggregation . . . . .	5
References . . . . .	8
<b>2. Coarsening of homoepitaxial structures in 2+1 dimensions</b> . . . . .	<b>9</b>
2.1 Introduction . . . . .	10
2.2 Monte–Carlo simulation . . . . .	10
2.3 Continuum equation . . . . .	14
2.4 Generalized free energy . . . . .	16
2.5 Coarsening . . . . .	19
2.6 Summary . . . . .	22
References . . . . .	23
<b>3. Strain in heteroepitaxial growth</b> . . . . .	<b>24</b>
3.1 Introduction . . . . .	25
3.2 Simulational methods . . . . .	28
3.3 Results . . . . .	30
3.4 Summary . . . . .	44
References . . . . .	45
<b>4. Scaling and river networks: A Landau theory for erosion</b> . . . . .	<b>46</b>
4.1 Statistical properties of river networks . . . . .	47

4.2	The model . . . . .	48
4.3	Numerical simulations . . . . .	52
4.4	Summary . . . . .	57
	References . . . . .	59
<b>5.</b>	<b>Diffusion-limited aggregation and viscous fingering in a wedge: Evidence for a critical angle . . . . .</b>	<b>61</b>
5.1	Fingering instability . . . . .	62
5.2	Finger competition . . . . .	64
5.3	The two-needle model . . . . .	66
5.4	Numerical simulations . . . . .	68
	References . . . . .	73
<b>6.</b>	<b>Diffusion-limited aggregation and iterated conformal maps . . . . .</b>	<b>74</b>
6.1	Introduction . . . . .	75
6.2	Numerical procedure . . . . .	80
6.3	Mathematical Background . . . . .	82
6.3.1	Laurent Expansion . . . . .	83
6.3.2	Statistical objects and the relations to generalized dimensions . . . . .	86
6.4	Numerical results and their interpretation . . . . .	87
6.4.1	Laurent Coefficients of $\Phi^{(n)}$ . . . . .	88
6.4.2	Multi-fractal exponents . . . . .	92
6.4.3	Fluctuations of the averages . . . . .	93
6.5	Summary and discussion . . . . .	100
	References . . . . .	102
<b>7.</b>	<b>Conclusion . . . . .</b>	<b>103</b>
<b>Appendix</b>	<b>. . . . .</b>	<b>105</b>
	References . . . . .	111

## LIST OF FIGURES

### Figure

2.1	Surfaces obtained by the Monte-Carlo simulation . . . . .	12
2.2	Time evolution of the top and the saddle point of two evolving mounds	13
2.3	Surfaces obtained by the continuum equation . . . . .	16
2.4	The equilibrium and the equilibrium part of the free energy . . . . .	18
2.5	The coarsening exponent in the simulation and in experiments . . . . .	20
3.1	Diffusion barrier of Ag adatom on stressed Ag(111) substrate . . . . .	32
3.2	Diffusion barrier of Ag adatom on stressed Ni(111) substrate . . . . .	33
3.3	The configuration to measure the effect of an island on the energy landscape . . . . .	35
3.4	Diffusion barrier of Ag on Ni(111) near a small Ag island . . . . .	36
3.5	Diffusion barrier of Ag on Ni(111) near a large Ag island . . . . .	37
3.6	Diffusion barrier of Ag on Ni(111) near a large Ni island . . . . .	39
3.7	Bonding energy to strained islands . . . . .	40
3.8	Pseudomorphic island . . . . .	41
3.9	Not pseudomorphic island with an adatom . . . . .	42
3.10	Four-fold hollow site on an island . . . . .	43
4.1	Stationary river network generated by the simulation . . . . .	53
4.2	The landscape created by the river of Fig. 4.1 . . . . .	54

4.3	The slope–area law obtained by the simulation . . . . .	55
4.4	The cumulative basin area distribution . . . . .	55
4.5	Horton’s laws . . . . .	56
5.1	Angular correlation function for DLA clusters in a wedge . . . . .	69
5.2	DLA clusters grown in wedges . . . . .	69
5.3	DLA clusters plotted with gray level proportional to the descendent measure . . . . .	71
6.1	Diagrammatic representation of the mappings . . . . .	77
6.2	Typical clusters of 10,000 particles . . . . .	81
6.3	Scaling exponents of the Laurent coefficients . . . . .	89
6.4	Scaling of $F_0$ . . . . .	90
6.5	Multifractal scaling of the harmonic measure . . . . .	93
6.6	Asymptotic distribution width of the Laurent coefficients . . . . .	94
6.7	Time-angle correlations of the field . . . . .	98
6.8	Effect of time correlations in the linear Laurent coefficient . . . . .	99
6.9	Correlations of the field . . . . .	100

# CHAPTER 1

## Introduction

### 1.1 Overview

Nonequilibrium statistical physics is one of the most rapidly growing branches of physics. The present understanding of far from equilibrium phenomena is behind that of equilibrium physics, providing a wide range of interesting problems.

In nonequilibrium systems there exists a mechanism which drives the system away from its equilibrium state. These processes give rise to rich and interesting pattern forming phenomena, which are the topic of this thesis.

A large class of nonequilibrium processes can be described as growth processes, in which a phase (or aggregate, or cluster) is growing. The main question is to understand and explain the static and dynamic properties of the growing cluster from the physics of the growth process.

In many cases the interface between the growing cluster and its environment is smooth on large scales. These objects, as well as their relation to scale-invariance is discussed in Section 1.2. An application with practical importance, molecular beam epitaxy, is introduced in Section 1.3. Systems of much larger scale, geomorphological evolution, are described in Section 1.4. Finally we introduce Laplacian growth and diffusion limited aggregation (DLA) in Section 1.5.

The following chapters contain our research results. In Chapter 2 we study homoepitaxial systems in the multilayer regime. Chapter 3 deals with heteroepitaxial systems, where strain is a significant factor. In Chapter 4 we present our coarse-grained theory for the evolution of river networks. The topic of the next two chapters is Laplacian growth and diffusion limited aggregation. Of these, Chapter 5 studies aggregates in wedge geometry, to show the existence of wedge-shaped building blocks in circular geometry. In Chapter 6 we use the approach of conformal maps to study the scaling properties of DLA clusters. Chapter 7 summarizes the results presented in this thesis, and finally in Appendix A we describe the numerical techniques to simulate large off-lattice DLA clusters.

## 1.2 Fractals and scale-invariance in surface growth

In many physical systems there exist a range of lengths such that the characteristic range of the underlying process lie outside of this range. A system could be much bigger than molecular dimensions, for example. It is natural to expect that this lack of internal scales will be reflected on the whole evolved system as well. If this range is large enough, then the description of the system on this range becomes meaningful. This description has to be without characteristic scales also, the system is *scale invariant*. Therefore the statistical quantities are also scale invariant; they are in general power laws, with crossovers marking the ends of the scaling range.

Fractals [1] are often found in these systems: these are scale invariant objects whose mass enclosed in a sphere of radius  $R$  and centered around a point of the object scales with a power of the radius:

$$M(R) \sim R^D \tag{1.1}$$

where  $D$ , the fractal dimension, is typically a fractional number (hence the term

fractal). These objects in general are self-similar: after rescaling they are statistically identical (except for the change of crossover scales) to the original.

In cases when the system has a strong orientation, often the process can be described as the evolution of an interface, which is smooth on large scales. Often these processes are called *surface growth* [2, 3]. The interface is a single valued function (*height*) of time and the lateral coordinates (the ones perpendicular to the strong orientation). Scale invariant functions are in general self-affine: they remain statistically invariant under rescaling with a different factor horizontally and vertically.

If the growth process is inherently local, then the time evolution should depend on local quantities only: the partial time derivative of the height should only depend on the height, its derivatives, possibly including some probabilistic factor (noise). This approach, usually called continuum description, is an important step towards understanding, because it is often possible to say something insightful about the solutions of these partial differential equations.

### 1.3 Molecular beam epitaxy

An important practical example of surface growth is molecular beam epitaxy (MBE). This technique is used to grow thin films on crystal surfaces, and has practical applications in the semiconductor industry. Typically a semiconductor or metal crystal with flat surface is chosen as substrate, put inside ultra-high vacuum, and bombarded with low energy atoms. The process is referred to *homoepitaxial* if the deposited atoms are of the same kind as the ones making up the crystal, and *heteroepitaxial* otherwise.

After the atoms land on the surface of the crystal, their thermal energy is large

enough for diffusion, but desorption is usually not significant (the sample is kept at  $300 - 800$  °C). When the diffusing atoms (called *adatoms*) meet, they form immobile structures called *islands*, which are the cores of the next crystal layer. Additional adatoms might join the island, or land on top of the islands. New islands may form on top of island, creating wedding cake like structures. Or the islands might grow, coalesce, and form the next crystal layer of the substrate.

A large number of materials exhibit the property that the atoms landed on top of islands are not likely to hop down. This behavior results in an effective upward current, and is responsible for the instability which creates large structures or *mounds*. These mounds grow and coalesce in time. This coarsening process is investigated in more detail in Chapter 2.

In case of heteroepitaxy, the situation is more complex. Even if the adatoms are chemically similar enough to the substrate atoms that they start to form their own crystal structure on top of the substrate, their size might be different from the substrate atoms, resulting in an elastic stress. During the evolution the system tries to minimize the excess energy resulted from this stress. One possibility is to grow high three-dimensional islands, where only the bottom of these islands is stressed. If the three-dimensional islands have narrow size distribution (*quantum dots*) and are ordered, then this could have practical importance for lasers and quantum computing. The issues of strained heteroepitaxial systems are discussed in Chapter 3.

## 1.4 Scale-invariance in geomorphological processes

Geomorphological objects are among the first in which scale invariance was observed [1]. There are various processes which form the surface of the Earth: tectonic motion, volcanic processes, erosion by ice, water and temperature fluctuation, earth-

quakes, sedimentation, mudslides etc. Out of these, we restrict our attention only to erosion by water flow, i.e. rivers.

A river system can be divided into three regions: the *production zone*, the source of most of the water the and sediments; the *transportation zone*, which is typically the meandering part of the river; and the *deposition zone*, where the river ends at a sea or ocean in a delta or estuary [4]. The production zone is the most interesting of these: this contains the branching network called *river basin*.

In natural rivers this branching network has remarkable statistical properties which cannot be explained by simple considerations. In Chapter 4 we investigate the evolution of this branching network: how the erosion of streams produces these complex patterns.

## 1.5 Laplacian growth and diffusion-limited aggregation

There exists a wide range of growth processes, where the rate limiting factor is the diffusion of some quantity. These processes can be described in terms of *Laplacian growth*. A field can be defined outside of the growing cluster, it satisfies the Laplace equation, and has a fixed value on the boundary. The local growth rate of the cluster is proportional to the gradient of the field at the boundary. This latter quantity is also called *harmonic measure*, referring to the field which satisfies the harmonic equation.

This picture in electrostatic terms is the following: the cluster is a conductor carrying unit charge, the Laplacian field is the electrostatic potential, and the growth rate is proportional to the electrostatic field or surface charge density.

Disorderly thin branching structures are produced by this process. The origin of the rich patterns is the Mullins–Sekerka instability: suppose that the boundary of

the cluster is flat with a small perturbation, then during growth the amplitude of the perturbation is increasing exponentially; the increase is faster if the wavelength of the perturbation is smaller. A small bump will grow into a large finger, but this is not stable either: it can have side fingers of any size, creating rich branched patterns.

The underlying physical process can contain possibly direction-dependent surface tension, which affects the growth process. The presence of surface tension energetically forbids large curvatures of the surface. On the other hand, at zero surface tension there are known exact solutions which produce singularities (cusps, where at one point the curvature is infinite) during finite time. Any finite surface tension is regularizing these singularities.

In many cases the growth occurs in finite chunks of material, here the *growth probability* is proportional to the harmonic measure. The discrete model of this process is the Witten–Sander model or diffusion limited aggregation (DLA)[5]. Here the aggregate consists of uniform particles, originally only a single seed. A random walker is released from infinity, which sticks to the cluster on first contact. Then a new walker is released.

The shot noise inherent in the discrete process has a significant effect on the growth process. Although the DLA model does not have explicit surface tension, the noise together with the uniform added chunks regularizes the instability.

The Witten–Sander model has attracted a good deal of attention in the scientific community. (This is demonstrated by the more than 1850 citations for the original paper — making it one of the top cited papers in condensed matter theory.) While the model has been known for almost two decades, and a large amount of empirical knowledge has been accumulated, little theoretical understanding has been achieved so far.

In Chapter 5 we study both theoretically and with computer simulations  $60\text{--}70^\circ$  wide angular regions of DLA clusters, and show that the cluster can be considered to be formed of these building blocks.

In a different approach to diffusion limited aggregation, developed only recently, the two dimensional growth is described as a sequence of conformal maps. In Chapter 6 we study the Laurent expansion of the map, and establish a relationship between the scaling properties of the model and the coefficients of the expansion. For example, the dimension of the cluster is determined by the linear coefficient, which seems to become deterministic with increasing cluster size.

## References

- [1] B. B. Mandelbrot, *The fractal geometry of nature* (Freeman, San Francisco, 1982)
- [2] T. Vicsek, *Fractal Growth Phenomena*, 2nd ed. (World Scientific, Singapore, 1992)
- [3] A.-L. Barabási and H. E. Stanley, *Fractal concepts in surface growth* (Cambridge Univ. Press, 1995)
- [4] I. Rodríguez-Iturbe and A. Rinaldo, *Fractal river basins – Chance and self-organization* (Cambridge Univ. Press, 1997)
- [5] T. A. Witten and L. M. Sander, *Phys. Rev. Lett.* **47**, 1400 (1981)

## CHAPTER 2

# Coarsening of homoepitaxial structures in 2+1 dimensions

The research presented in this chapter was done with Professor Leonard M. Sander; the numerical work was done by me, the analytical work was split between us. It was published in “Dynamics of crystal surfaces and interfaces”, edited by P. M. Duxbury and T. J. Pence. (Plenum, New York, 1997).

When thin solid films are grown by MBE, the presence of Ehrlich–Schwoebel barrier leads to the formation of mounds [M.D. Johnson et al., Phys. Rev. Lett. **72**, 116 (1994)]. As the film grows these mounds grow larger (coarsen). We study this coarsening in 2+1 dimensions by comparing simulations of an activated hopping model with solutions to the continuum equations we introduced previously. The principal mode of coarsening is the disappearance of saddle points from the surface. In 2+1 dimensions the evolution is characterized mainly by nonequilibrium terms and is not driven by capillary forces. We find that the mounds coarsen as a power law in time. In strongly nonequilibrium growth conditions a low value of the coarsening exponent ( $n = 1/6$ ) is observed, while in the weakly nonequilibrium case  $n = 1/4$ .

## 2.1 Introduction

Molecular beam epitaxy is a widely used technique for growing structures on crystal surfaces. One of the goals is to be able to control the growth process to such extent that one can make the nanostructures complex enough for a particular purpose. An ambitious example is a quantum computer [1].

In this chapter we investigate the effect of the growth parameters (near equilibrium or far from equilibrium) on the growth process. In many materials the diffusion of an adatom on a singular surface (terrace) is faster than across a step edge: the downward diffusion is suppressed by the Ehrlich–Schwoebel barrier [2]. This barrier gives rise to an instability in the growth process against mound formation, as proposed by Villain [3], and investigated by Johnson et al. [4] These 3-dimensional mounds coarsen: their lateral size  $L$  increases in time according to  $L \sim t^n$ . In this chapter we focus on the question how  $n$  depends on the growth conditions. We also show that the continuum equation proposed by the Michigan group [4, 5] is a reasonable description of the process.

## 2.2 Monte–Carlo simulation

One of our tools is an activated hopping Monte-Carlo simulation. We implemented a simple model for growth processes: the solid-on-solid model on cubic lattice. Although one expects that a model reflecting the microscopic details of the crystal structure (e.g. fcc(001)) would better describe the real situation [6], even this very simple model captures correctly the phenomenon of coarsening. Also, the cubic lattice model appears to simulate very well the more complicated semiconductor growth, where one cube stands for e.g. a 2x4 block of GaAs. In our model the atoms land on the surface at rate  $F$ . All atoms on the surface undergo activated dif-

fusion with rate  $\nu \cdot \exp(-E/kT)$ , where  $\nu = kT/h$  is the attempt frequency ( $k$  is the Boltzmann constant,  $h$  is the Planck constant), and the energy barrier,  $E$ , depends on the local neighborhood of the diffusing atom. We make a further simplification:  $E$  depends linearly on the number of nearest neighbors,  $n$ , of the atom at the initial position (the number of bonds to break), and also on the change in next-nearest neighbors,  $\Delta nn$ , if it is negative:

$$\Delta nn = \begin{cases} nn^f - nn^i, & \text{if } nn^f - nn^i < 0 \\ 0, & \text{otherwise.} \end{cases}$$

where  $nn^f$  and  $nn^i$  is the number of next-nearest neighbors in the final and initial state. The first factor takes care of island formation and attachment of adatoms to step-edges, while the second models the Ehrlich–Schwoebel barrier to some extent. The entire form of the barrier is

$$E = E_0 + n \cdot E_n - \Delta nn \cdot E_{nn} \quad (2.1)$$

where  $E_0$  is the barrier of a flat terrace. Details of the model can be found in Johnson et al. [4].

Fig. 2.1 shows surfaces obtained by this simulation. The surface is symmetric under the transformation  $h \rightarrow -h$  in case of high flux and high Ehrlich–Schwoebel barrier, while for other regions of the parameter space this symmetry is broken: the mounds have flat tops, and the valleys between them are narrow and deep. We can trace the process of coarsening. Initially the surface consists of many small mounds, they can be characterized by the maxima (tops) and the saddle points between mounds. We now focus on the coarsening, i.e. how two of these mounds merge. The mounds grow in time, and they compete with each other for the base area. Eventually one of them becomes large by a fluctuation. Then the saddle point between the mounds approaches the smaller maximum and annihilates it (Fig. 2.2): this is the

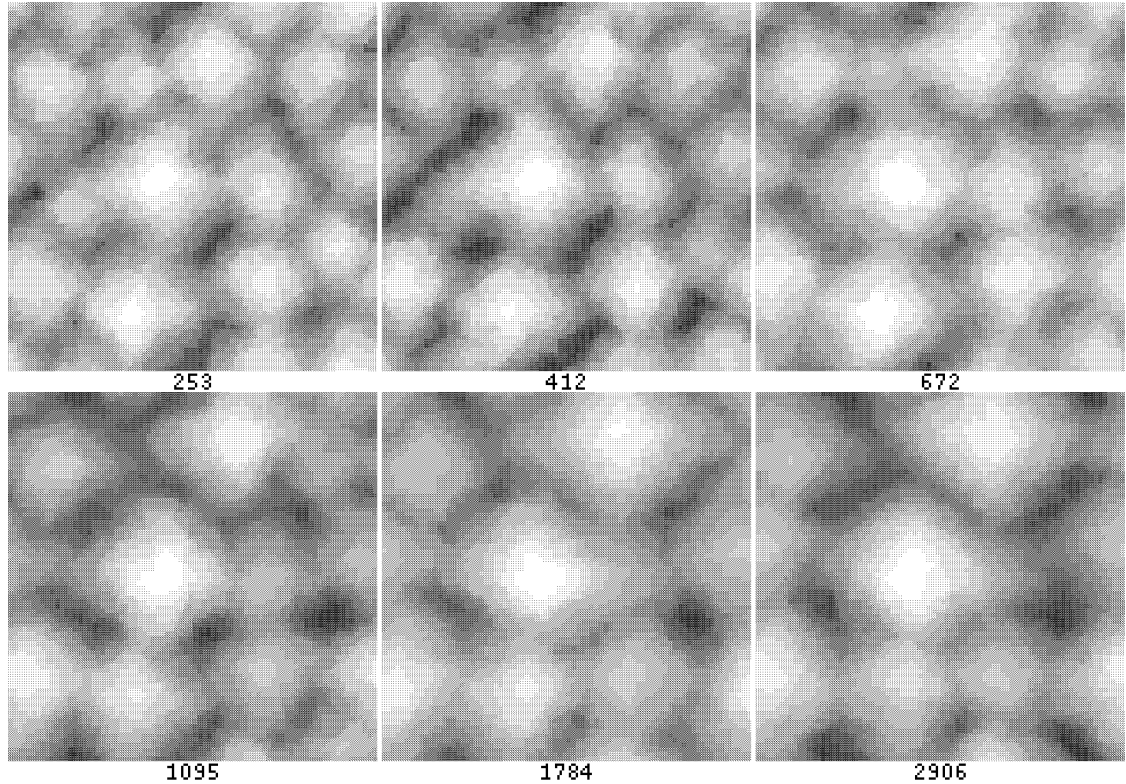


Figure 2.1: Snapshots of the time evolution of the surface obtained by the simulation, the flux of the incoming atoms is  $F = 1 \frac{\text{ML}}{\text{sec}}$ , and the strength of the Ehrlich–Schwoebel barrier is  $S = 0.653$ . In this regime of the parameter space the surface grows symmetrically with respect to the transformation  $h \rightarrow -h$ . The number of deposited monolayers is shown under the images.

most important step of the coarsening process. What is left is one large mound, which rearranges itself to be more-or-less symmetric. There can be fluctuations in the other direction: the top of a mound can split and merge again as observed by Šmilauer and Vvedenski [7].

The coarsening process (growth of dominant wavelength) takes place during the approach to equilibrium as well. We carried out simulations verifying this. We started the process with two-dimensional sine wave initial conditions, and with no incident flux, so that the surface relaxed towards a plane. After a short transient

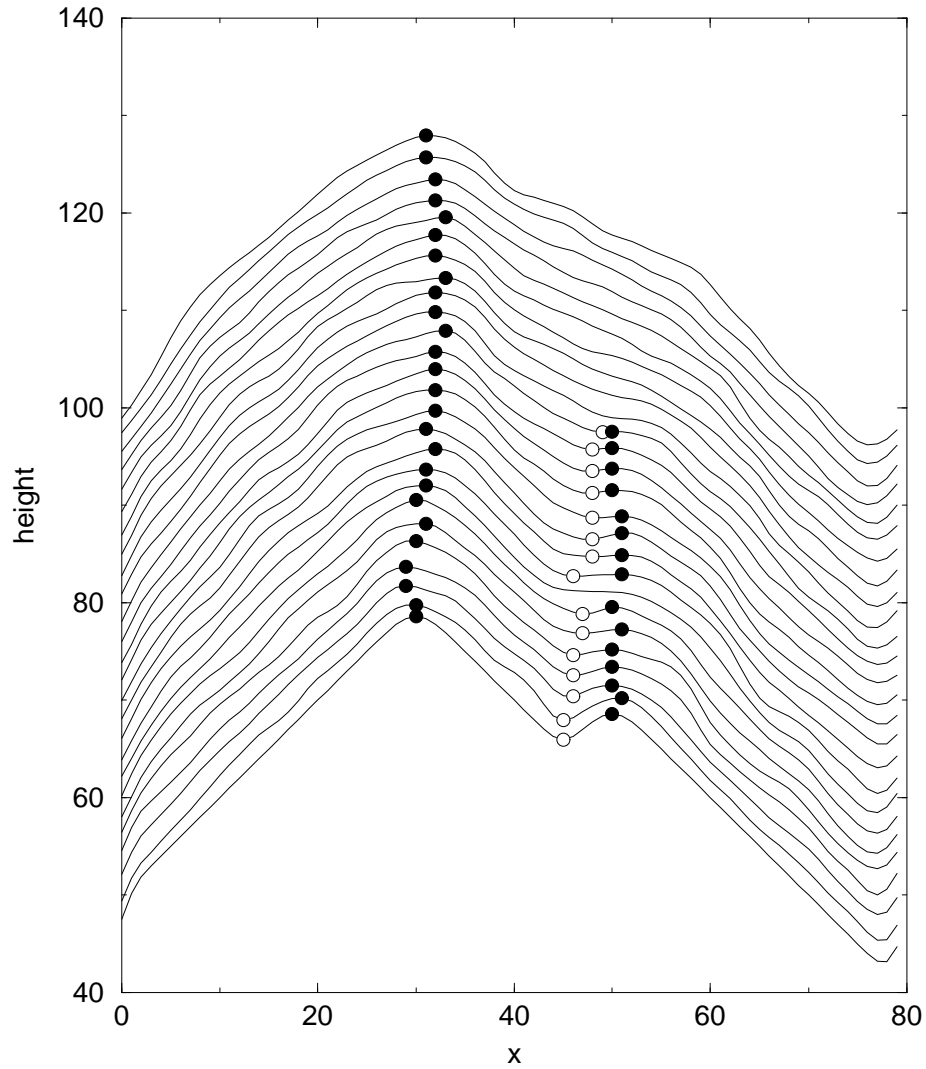


Figure 2.2: Time evolution of the top ( $\bullet$ ) and the saddle point ( $\circ$ ) on a cross-sectional view of two evolving mounds. The saddle point annihilates the top of the small mound, while the maximum of the large mound only fluctuates. Both the height and the lateral position are measured in lattice units.

(during which the surface rearranged its profile according to the strength of the Ehrlich–Schwoebel barrier) the root-mean-square width decreased as  $w \sim \exp(-st)$ , where the wavelength-dependence of the exponent,  $s$ , is

$$s = 4D_4 \left( \frac{2\pi}{L} \right)^4 \quad (2.2)$$

showing that the equilibrium coarsening is dominated by diffusion processes [8]. That is, we have  $\partial h / \partial t = -D_4 \nabla^4 h$ , the Mullins equation. We have verified that this equation holds for our Monte-Carlo model, and we have measured  $D_4$ .

### 2.3 Continuum equation

A different way to approach the coarsening process is to concentrate on the long wavelength properties and analyze them in the framework of a continuum equation. The height  $h(\vec{x}, t)$  of the surface is measured from its mean height. Changes in height arise from the divergence of the surface mass current:

$$\frac{\partial h}{\partial t} = -\nabla \cdot \vec{j}. \quad (2.3)$$

The surface current consists of a non-equilibrium part driven by the incident flux and the Ehrlich–Schwoebel barrier, and the equilibrium part driven by capillary forces:

$$\vec{j} = \frac{FS\sigma^2 \nabla h}{1 + (\sigma \nabla h)^2} + D_4 \cdot \nabla \nabla^2 h + D_6 \cdot \nabla \nabla^2 \nabla^2 h + \dots \quad (2.4)$$

The parameters are the flux,  $F$ , of the incoming atoms; the strength,  $S$ , of the Ehrlich–Schwoebel barrier ( $S = R - T$  with  $R$  being the probability of reflection and  $T$  the probability of transmission across a step edge). The length,  $\sigma$ , is the mean distance between nucleation centers on a terrace, and  $D_4$  is the strength of the equilibrium capillary forces. The last term in the current is the next term in the expansion series consistent with the symmetry.  $D_4$  corresponds to healing of edges,

while  $D_6$  may correspond to the healing of corners. This last term is negligible near equilibrium compared to the  $D_4$  term, which is why the classic Mullins theory takes the leading  $D_4$  term only.

To give a physical interpretation of the non-equilibrium part of the current [4], let us assume that the Ehrlich–Schwoebel barrier is infinitely strong (no atoms can jump down a step), and the up steps are perfect sinks. In this case for small slopes  $\nabla h$ , only the atoms that land in strips of width  $\sigma$  will reach the up steps, the rest will attach to islands on the terrace, and do not contribute to the net mass current. In this case the total current is the fraction of the incoming flux which contributes to the current, multiplied by the mean migration length of the adatoms:  $\vec{j} = F\sigma^2\nabla h$ . For the large slope limit, every incoming atom contributes to the current, but the migration length is only  $1/|\nabla h|$ , yielding  $j = F/|\nabla h|$ . The generalization for finite Ehrlich–Schwoebel barriers ( $S < 1$ ) is simply to multiply the current by  $S$ . A convenient interpolation between these expressions for the non-equilibrium current is given in Eq. (2.4).

The present form (2.4) of the surface current is odd in  $h$ , so a surface growing from this current will be symmetric under the transformation  $h \rightarrow -h$ . Another feature of this current is that in the absence of curvature it is finite for nonzero slopes  $\nabla h$ . Other terms in the current, which we did not include, could make the current zero [9] for a given slope  $m_0$ . This stabilizes the slope of the growing structures around  $m_0$ , and explains the phenomena of selected slope. Although the selected (or “magic”) slope has been observed in many experiments, it is not necessarily present in every case and is not believed to be important in the coarsening process: coarsening occurs not only in cases where a selected slope is achieved, but also in different experiments where the slope grows indefinitely.

By integrating Equations (2.3) and (2.4), neglecting the  $D_6$  term, with ran-

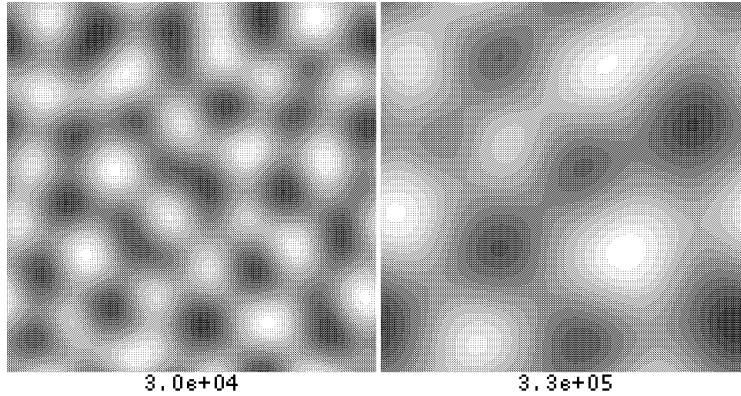


Figure 2.3: Typical images of the surfaces obtained by the integration of the continuum equation. The rescaled time is shown below the images.

dom initial conditions, mounds similar to those of the simulation can be obtained (Fig. 2.3). These mounds also coarsen in time. However, there has not been direct test of this equation as a description of multilayer growth. In particular, Eq. (2.4) was derived by fitting to Monte-Carlo data in the submonolayer regime. In this chapter we show that certain aspects of multilayer growth by the Monte-Carlo model are well represented by Eq. (2.3) and (2.4).

Results of Ref. 5 show that integrating these equations generates coarsening: the time dependence of the lateral size,  $r_c$ , of the mounds scales with a power of time,  $r_c \sim t^n$ , with exponent  $n = 1/4$ . This exponent is associated with the leading  $D_4$  term. Similarly, Stroscio et al [10] found  $n = 1/6$  numerically when only the  $D_6$  term was present. A detailed analytical proof is given by Golubovic [11].

## 2.4 Generalized free energy

In order to quantitatively compare the simulation with the continuum equation, we introduce a generalized free energy of the surface, and write the equation of motion in variational form.

By appropriate rescaling of the variables  $\vec{x}$ ,  $t$  and  $h$  to  $\vec{X}$ ,  $T$  and  $H$ , the parameters

in the equation of motion can be scaled out, leading to a dimensionless equation. Considering the present form (2.4) of the current, without the  $D_6$  term, the equation of motion of the surface can be written in form of a functional derivative:

$$\frac{\partial H}{\partial T} = -\frac{\delta \mathcal{F}[H]}{\delta H} \quad (2.5)$$

where

$$\mathcal{F}[H(X, T)] = \frac{1}{2} \int \left( -\log(1 + (\nabla_X H)^2) + (\nabla_X^2 H)^2 \right) d^2 X \quad (2.6)$$

which we call free energy. It is a functional of the rescaled height  $H$ .  $\mathcal{F}$  consists of a non-equilibrium and an equilibrium term, like the current. This free energy does not coincide with the conventional free energy of the surface, but has the similar property that in our non-equilibrium growth conditions  $\mathcal{F}$  is the quantity driving the system, and is a monotonically decreasing function of time. It is important to point out, that contrary to the previous claims [5], in case of a current that produces asymmetric surfaces, no free energy can be found. (The lowest order term in the free energy density, which breaks the  $H \rightarrow -H$  symmetry but conserves the  $\vec{X} \rightarrow -\vec{X}$  symmetry and the translation invariance in  $H$  and  $X$  would be 3rd order in  $H$  and 6th order in  $X$ , thus can be excluded from our consideration.)

At this point we are able to compare the coarsening process of the Monte-Carlo simulation with that of the continuum equation, (2.5). We rescale the surfaces obtained in the simulation to the dimensionless variables  $H(\vec{X}, T)$ , and compare the time evolution of the free energy associated with the rescaled surface of the simulation (with different parameter values) with the free energy of the continuum equation. As we expect, the free energy (Fig. 2.4) decreases in time. But it turns out that the equilibrium part itself increases, so it cannot drive the process. This is different from the case of spinodal decomposition, which also shows power law coarsening and

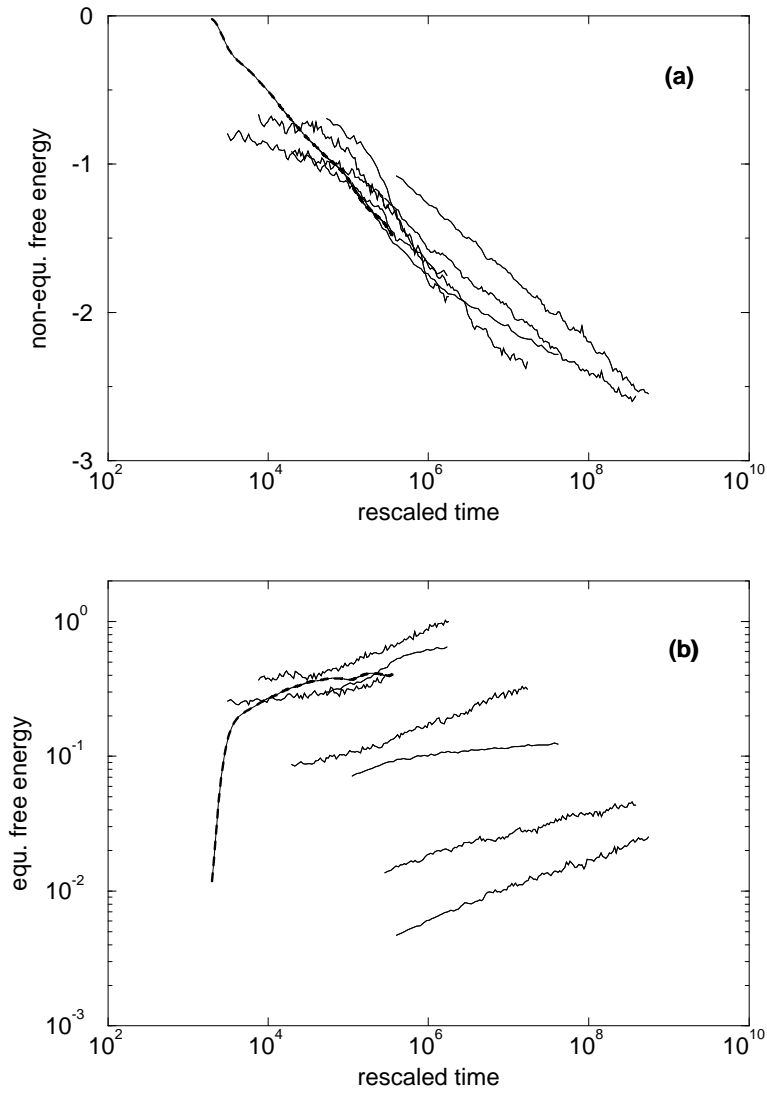


Figure 2.4: The (a) nonequilibrium and the (b) equilibrium part of the free energy. (The free energy itself is the sum of these two.) The dashed line corresponds to the continuum equation, the solid lines are the rescaled curves of the simulation for different parameter values ( $F$ ,  $S$ ).

which can be mapped on to this problem in 1+1 dimensions. In that case minimization of the surface energy drives the process. Here the surface energy increases in time.

It can be seen from the comparison that the non-equilibrium part (Fig. 2.4a), which in most cases dominates the free energy, is consistent with that of the continuum equation. But on the other hand, although the equilibrium part (Fig. 2.4b) more-or-less coincides with the result of the continuum equation for some parameter values of the simulation, for an another domain of the parameter space it does not. This could mean (and later we will argue that it does) that the  $D_6$  term of Eq. (2.4) *is* important in those cases. We will give an explanation for this later in this chapter.

## 2.5 Coarsening

An another way of describing the coarsening process is to study the time dependence of the characteristic feature separation  $r_c$  (the lateral size of the mounds, defined as the first zero crossing of the correlation function  $\langle h(0)h(\vec{r}) \rangle$ ). In most cases  $r_c$  scales as a power of time,

$$r_c \sim t^n \tag{2.7}$$

where  $n$  is the coarsening exponent. As we mentioned before, for diffusion dominated growth  $n = 1/4$ , and this is the case for the continuum equation, in the absence of the  $D_6$  term [5, 9].

But in the coarsening process of the Monte-Carlo simulations (Fig. 2.5) the exponent is  $n = 1/6$  for a domain of the parameter space  $(F, S)$ , while for other regions it is  $n = 1/4$ . The region where the value of the coarsening exponent does not equal to the value of the diffusion dominated case is the high flux, high Ehrlich–Schwoebel barrier corner of the parameter space. In this regime the growth conditions are

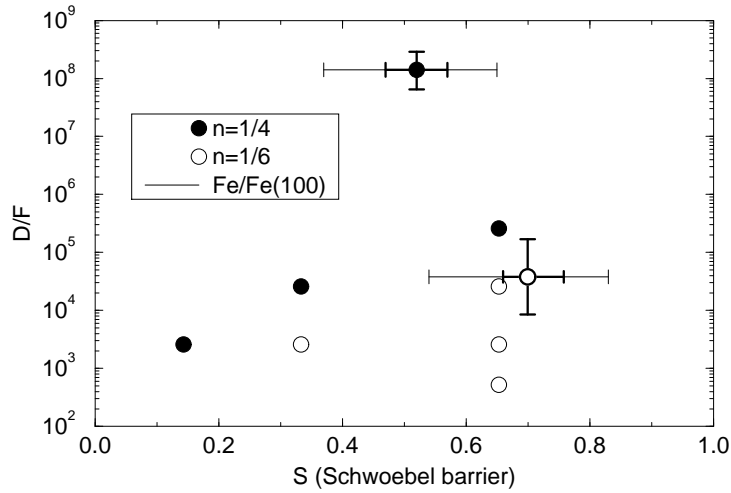


Figure 2.5: The value of the coarsening exponent  $n$  of the Monte-Carlo surfaces and two experimental surfaces as a function of the growth parameters. The points ( $\circ$ ) where  $n = 1/6$  coincide with those simulations where the equilibrium part of the free energy *did not* match that of the continuum equation. The error bars show the parameter range/uncertainty of an Fe/Fe(100) experiment of Ref. [10] ( $\circ$ : measured  $n = 0.16 \pm 0.04$ ) and Ref. [12] ( $\bullet$ : measured  $n = 0.23 \pm 0.02$ ). The estimate of the Ehrlich–Schwoebel barrier is taken from Ref. [13] (thin line) and Ref. [14] (thick line).

strongly out of equilibrium: the high Ehrlich–Schwoebel barrier restricts the free diffusion of the adatoms, and the high flux also keeps the system far from equilibrium, the adatoms do not have enough time to find a preferred equilibrium position. This coincides with the region where the equilibrium free energy did not match the equilibrium free energy of the continuum equation. In this far from equilibrium regime the  $D_6$  term of the current could be significant,  $D_6$  can depend on the flux and the Ehrlich–Schwoebel barrier. This term can dominate the coarsening, and give  $n = 1/6$  if the  $D_4$  term of Eq. (2.4) is missing, as first suggested by Stroscio et al. [10]. The presence of the  $D_6$  term, which we neglected in our continuum equation, is the explanation for the fact, that the equilibrium part of the free energy of the far from equilibrium simulations deviates from that of the continuum equation.

Experimental results support this parameter-space dependence of the coarsening exponent as well. In case of Fe/Fe(100) homoepitaxial growth (where there are estimates for the value of the Ehrlich–Schwoebel barrier), at room temperature  $n = 1/6$  has been measured [10] ( $n = 0.16 \pm 0.02$ ), while at elevated temperature [12] the exponent is  $1/4$  ( $n = 0.23 \pm 0.02$ ). These results are in excellent agreement with our predictions (Fig. 2.5).

In the near-equilibrium regime,  $n = 1/4$  and both parts of the free energy (thus the free energy itself also) coincide with that of the continuum equation. In these cases Equations (2.3), (2.4) and (2.5) give a good description of the evolution of the surface, the correct roughening behavior, and the correct functional form of the free energy. It should be noted that in order to fit the free energy of the continuum equation to that of the simulations, we used only one free fitting parameter (the time offset of the continuum equation, since its random initial conditions are arbitrary), all other parameters were either input parameters of the Monte-Carlo model or measured

directly in the simulation, as in the case of  $D_4$ , above.

## 2.6 Summary

We have investigated the coarsening process in homoepitaxial systems using Monte-Carlo simulations and continuum equations. From the geometric aspects of coarsening, the scenario for merging two mounds is the following: after initial competition between the mounds, the saddle point between them annihilates with the maximum of the smaller mound, then the one big mound rearranges itself to be symmetric.

In case of relaxation to equilibrium, the process is diffusion-dominated and the presence of the  $D_4$  term is verified. For non-equilibrium conditions we have two cases: For weakly out of equilibrium (low flux, low Ehrlich–Schwoebel barrier) the  $D_4$  term is still present and dominates the long-time coarsening, characterized by  $n = 1/4$ . However, for strongly out of equilibrium cases (high flux, high Ehrlich–Schwoebel barrier) the  $D_4$  term seems to be dominated by the  $D_6$  term, causing coarsening with exponent  $n = 1/6$ .

We would like to thank Brad Orr, Chris Orme and Ji Li for useful discussions, and also Mark Johnson and Chris Orme for letting us to use their computer programs. This work was supported by NSF grant DMR 9420335.

## References

- [1] S. Lloyd, *Science* **261**, 1569 (1993); J.I. Cirac, P. Zoller, *Phys. Rev. Lett.* **74**, 4091 (1995).
- [2] G. Ehrlich and F.G. Hudda, *J. Chem. Phys.* **44**, 1039 (1966); R.L. Schwoebel, *J. Appl. Phys.* **40**, 614 (1969).
- [3] J. Villain, *J. Phys. (Paris) I* **1**, 19 (1991).
- [4] M.D. Johnson, C. Orme, A.W. Hunt, D. Graff, J.L. Sudijono, L.M. Sander and B.G. Orr, *Phys. Rev. Lett.* **72**, 116 (1994).
- [5] A.W. Hunt, C. Orme, D.R.M. Williams, B.G. Orr and L.M. Sander, *Europhys. Lett.* **27**, 611 (1994).
- [6] J.G. Amar and F. Family, *Phys. Rev. B* **54**, 14742 (1996).
- [7] P. Šmilauer and D.D. Vvedenski, *Phys. Rev. B* **52**, 14263 (1995).
- [8] W.W. Mullins, *J. Appl. Phys.* **28**, 333 (1957).
- [9] M. Siegert and M. Plischke, *Phys. Rev. Lett.* **73**, 1517 (1994); M. Siegert, in: *Scale Invariance, Interfaces and Non-Equilibrium Dynamics*, A. J. McKane, ed., Plenum, New York (1994).
- [10] J.A. Stroschio, D.T. Pierce, M. Stiles, A. Zangwill and L.M. Sander, *Phys. Rev. Lett.* **75**, 4246 (1995).
- [11] L. Golubovic, *Phys. Rev. Lett.* **78**, 90 (1997).
- [12] K. Thürmer, R. Koch, M. Weber and K.H. Rieder, *Phys. Rev. Lett.* **75**, 1767 (1995).
- [13] J.G. Amar and F. Family, *Phys. Rev. B* **52**, 13801 (1995).
- [14] M.C. Bartelt and J.W. Evans, *Phys. Rev. Lett.* **75**, 4250 (1995).

## CHAPTER 3

# Strain in heteroepitaxial growth

In this chapter we use atomistic simulations with an empirical potential (EAM) to study the elastic effects of heteroepitaxial islands on adatom diffusion. We measure the diffusion barrier on pure stressed substrate and near a misfit island, as well as the detachment barrier from islands of different size.

The numerical work presented in this chapter was done by me, and the analytical work was shared with Leonard M. Sander and Bradford G. Orr.

### 3.1 Introduction

Molecular beam epitaxy is used extensively to grow thin films on crystal surfaces. Although homoepitaxial systems give rise to interesting questions, as seen in Chapter 2, the case of heteroepitaxy is much more complex.

One of the main consequences of the fact that the substrate and the adlayers are made of different atoms is the stress generated in the adlayers. Suppose that the lattice constant of the crystal made of adatoms is larger than the substrate lattice constant (the adatoms are “larger” than the substrate atoms). Then if the adlayers are *pseudomorphic* (follow the periodic order of the substrate without dislocations), they have to be compressed. The size difference is not necessarily the only source of stress: the compressive stress of few monolayers of Ag on Pt(111) is measured to be five times larger than expected from the size difference [1]. The reason is presumably charge transfer from the adlayers to the substrate due to their chemical difference.

In close to equilibrium conditions the growth is layer-by-layer (also called Frank–van der Merwe [2]), if this is the energetically most favorable configuration. However, since the elastic energy of the stressed layer is proportional to its height, the excess elastic energy (over the configuration of relaxed adlayers) will overcome the barrier of creating a dislocation network at the bottom of the adlayers for relaxation. Thus pseudomorphic growth cannot be stable for arbitrarily large thickness.

Relaxed layer-by-layer growth is not the only possibility to overcome the excess elastic energy. If the adatoms form tall, 3-dimensional islands, the lattice constant in the majority of an island can be close to its bulk value, and only the bottom of the island is stressed. In case of Volmer–Weber growth [3], the 3-dimensional islands nucleate right on the substrate, while in the Stranski–Krastanow scenario [4] first few

layers grow epitaxially (*wetting layers*), continued by the growth of 3-dimensional islands on top of them.

The typical growth conditions in MBE are not necessarily close to equilibrium. In this case the dynamical effects greatly modify the above thermodynamic considerations. If the dynamical effects dominate the process, then the nucleation dynamics on different layers and the interlayer transport become important [5].

The 3-dimensional islands are important for practical applications, as they are a good candidate for lateral electron confinement. Certain semiconductor systems (e.g. InAs on GaAs) develop 3-dimensional island structure, where the size distribution of the islands is narrow, free of dislocations, and their spatial distribution is relatively ordered [6]. Since this ordering takes place during epitaxy without fabrication (e.g. high resolution lithography), they are often called *self-organized quantum dots*. The self-organization can be enhanced by alternately growing GaAs and the strained InAs: this results in a 3-dimensional structure where the successive layers of InAs are increasingly more ordered [7].

However, the uniformity of current InAs quantum dots is insufficient for laser applications. It has been suggested recently that the size distribution of the quantum dots is similar to the distribution of the 2-dimensional islands, it follows the same renormalized curve for a range of island densities, and therefore strain does not seem to be relevant factor determining the size distribution [8].

An atomic level simulation of strained epitaxial systems has been done by Orr, Kessler, Snyder and Sander [9]. In this pioneering work the dynamic Monte-Carlo method has been applied in one dimension, which incorporated linear elasticity. The surface particles were able to hop to neighboring sites, with the hopping probability depending upon both the bond and strain energy. The lattice was locally relaxed

after each motion, with global relaxation after fixed number of timesteps. The elastic lattice was modelled with harmonic forces between nearest and next-nearest neighbors.

It has been observed that tall islands form, and that their lateral size is smaller with increasing misfit. The kinetics determine the morphology: the thermodynamic effects can reach only up to the diffusion length: the typical distance a walker diffuses during the deposition of a monolayer. On larger scales the surface is smooth — as rough as it would be without strain.

Schroeder and Wolf [10] studied the effect of strain on surface diffusion. They observed that the activation barrier is with good approximation a linear function of strain over a wide range: compressive strain enhances diffusion, while tensile strain hinders it. The strain changed mostly the energy of the saddle point, the stable sites were not affected considerably. The strain field of a coherent two-dimensional island is not uniform (the edges are more relaxed than the center), therefore this is reflected on the diffusion of adatoms on top of the island. In this work simple cubic, fcc and bcc lattice has been used with Lennard–Jones potential.

It is tempting to write down a mean-field theory using self-consistent rate equations. Refs. [11, 12] model the process with the following dynamical variables: the density of adatoms, the density of “typical size” 2-dimensional (2d) islands, and the density of “typical size” 3-dimensional (3d) islands. The attachment, detachment, diffusion, and 2d/3d conversion rates (see later) are given in terms of 6 parameters: the critical island size, the surface diffusion barrier, the Ehrlich–Schwoebel barrier[13], the binding energy of a critical island, the attachment barrier (same for 2d and 3d islands), and one more parameter  $E_0$  with dimensions of energy. The

elastic effects are taken into account in the detachment barrier from a 2d island:

$$E_{\text{detach}} = E_0 \frac{\log r}{r} \quad (3.1)$$

( $r$  is the island radius), and also in the assumption that as soon as an island nucleates in top of a 2d island, it immediately transforms to 3d island. The parameters are selected to match an InP/GaAs(001) metal-organic vapor phase epitaxy process, and an adequate description is achieved.

In the research summarized in this chapter we study the effects of misfit strain on the energy landscape observed by the diffusing adatoms, and also how that affects the growth process.

## 3.2 Simulational methods

In our simulations we use a substrate of slab geometry, which is periodic in the lateral directions, has open surface at the top, and bounded by a frozen lattice from below. The atoms of the substrate and the adlayers or adatoms are allowed to relax according to the potential described below, but we did not introduce dislocations to the substrate. The relaxation is achieved by using conjugate gradient methods.

It is necessary to have the relaxable substrate as deep as wide, because the elastic effects penetrate roughly isotropically[10]. If the lattice was shallower, then that would cut off the deformation field such a way that the effective range of the elastic deformation in the lateral direction would be limited to the depth, losing possibly important long range effects. This restriction has severe consequences on the lattice sizes that are computationally tractable.

For interatomic potential, we used the embedded atom method (EAM). It belongs

to the class of pair functionals: the form of the potential is

$$E_{\text{tot}} = \frac{1}{2} \sum_i \sum_{j(\neq i)} \phi^{(ij)}(R_{ij}) + \sum_i F^{(i)}(\rho_i^{\text{host}}) \quad (3.2)$$

The upper index in parenthesis denotes dependence only through the type of the atom.  $\phi^{(ij)}(R)$  is the pair-potential part,  $F^{(i)}(\rho^{\text{host}})$  is the embedding function, its argument is the “electron density at the host atom”, given by

$$\rho_i^{\text{host}} = \sum_{j(\neq i)} \rho_j(R_{ij}) \quad (3.3)$$

where  $\phi^{(ij)}$ ,  $F^{(i)}$  and  $\rho_j$  are given functions.

The rationale of this type of potential is the following[15]. For the transition metals (for which the potential is to be used) there is a relatively well defined separation of positively charged ions and nonlocal conduction electrons. The interaction of the ions is described by  $\phi^{(ij)}$ . The ions are embedded into the electron density contributed by their neighbors (the name *embedded atom* comes from this), and their interaction with the electron field is given in  $F^{(i)}$ .

To write down the pair repulsion term, the ions are considered as charged spheres of effective charge  $Z^{(i)}(R)$ :

$$\phi^{(ij)}(R) = \frac{Z^{(i)}(R)Z^{(j)}(R)}{R} \quad (3.4)$$

and the effective charge is given in parametric form:

$$Z(R) = Z_0(1 + \beta R^\nu)e^{-\alpha R}. \quad (3.5)$$

$Z_0$  is the number of outer  $d$  and  $s$  electrons;  $\alpha$ ,  $\beta$  and  $\nu$  (the last one is integer) are to be fitted. The electron contribution  $\rho_j(R)$  is estimated from the Hartree-Fock wavefunctions of the outer  $d$  and  $s$  electrons. Finally the embedding function  $F^{(i)}$  is

defined such that the equation of state of the isotropically compressed or expanded metals follow the universal function ( $a$  is lattice constant):

$$E(a) = -E_{\text{sub}}(1 + a^*)e^{-a^*}, \quad (3.6)$$

where  $a^*$  is a measure from the deviation from equilibrium lattice constant:

$$a^* = \frac{a - a_0}{a_0} \left( \frac{9B\Omega}{E_{\text{sub}}} \right)^{1/2}. \quad (3.7)$$

$a_0$  (the equilibrium lattice constant),  $B$  (bulk modulus),  $E_{\text{sub}}$  (sublimation energy), and  $\Omega$  (equilibrium volume per atom) are supplied directly by experimental values, the electron orbitals are taken from Roothaan–Hartree–Fock tables of ground state atoms, and the rest of the parameters are fitted according to other experimental values (shear moduli, vacancy-formation energy, mixing enthalpies between different metals). The parameters used in our simulation are given in Ref. [15].

This pseudopotential provides reasonable values for a row of bulk properties. There is some concern that it is similarly appropriate for surface simulations. In EAM, the atoms are considered spherical (which is good approximation for bulk transition metal atoms). Surface atoms, however, are in an anisotropic environment. The universal equation of state at very much expanded state is not necessarily good description for the low coordinated surface atoms sitting in low embedding electron density. Nevertheless, EAM is still more realistic approach than pair potentials, and computationally tractable for the necessary system sizes as opposed to first principle calculations.

### 3.3 Results

First we measured the effect of strain on the diffusion barrier. The substrate lattice was compressed in the horizontal directions by a given factor, and was allowed

to relax vertically. Then an adatom was placed on top, and the whole system was allowed to fully relax. Fig. 3.1 shows the energy of the system when a Ag adatom was placed on a stable, metastable and bridge point of a stressed Ag(111) substrate. The diffusion barrier (the difference of the bridge and the stable/metastable energy) is also plotted.

Around zero stress the barrier was close to be a linear function of the lattice constant, with increasing barrier for tensile strain. This is the expected behavior: under compressive strain the energy landscape becomes more uniform, while under tensile strain the adatom feels more the separate attracting potential of the surface atoms. For large tensile strain this trend breaks down: the surface becomes softer, bringing down bridge energies, resulting in decreased diffusion barrier.

The same procedure has been applied to the Ag/Ni(111) heterodiffusion system, the barriers and energies are depicted on Fig. 3.2. While the behavior of the diffusion barrier is qualitatively the same as in the Ag self-diffusion case, the dependence of energies on strain is different. Around zero stress, here the stable sites are unaffected, and the bridge energy is changing. From this we can draw the conclusion that whether the energy of the stable sites or the bridge point changes under stress is system dependent, no general statements can be made.

To test the reliability of our procedure, we plot on Fig. 3.1a the diffusion barrier measured by the effective medium theory also (the values are from Ref. [16]). While the EAM values are consistently lower by about 10 meV, the general trend of the curves is very similar.

Our primary goal is to study the elastic effects of an island on the energy landscape observed by the diffusing adatoms. To pursue this we deposited a large hetero-island and an adatom on the substrate, and computed the energy of the system for different

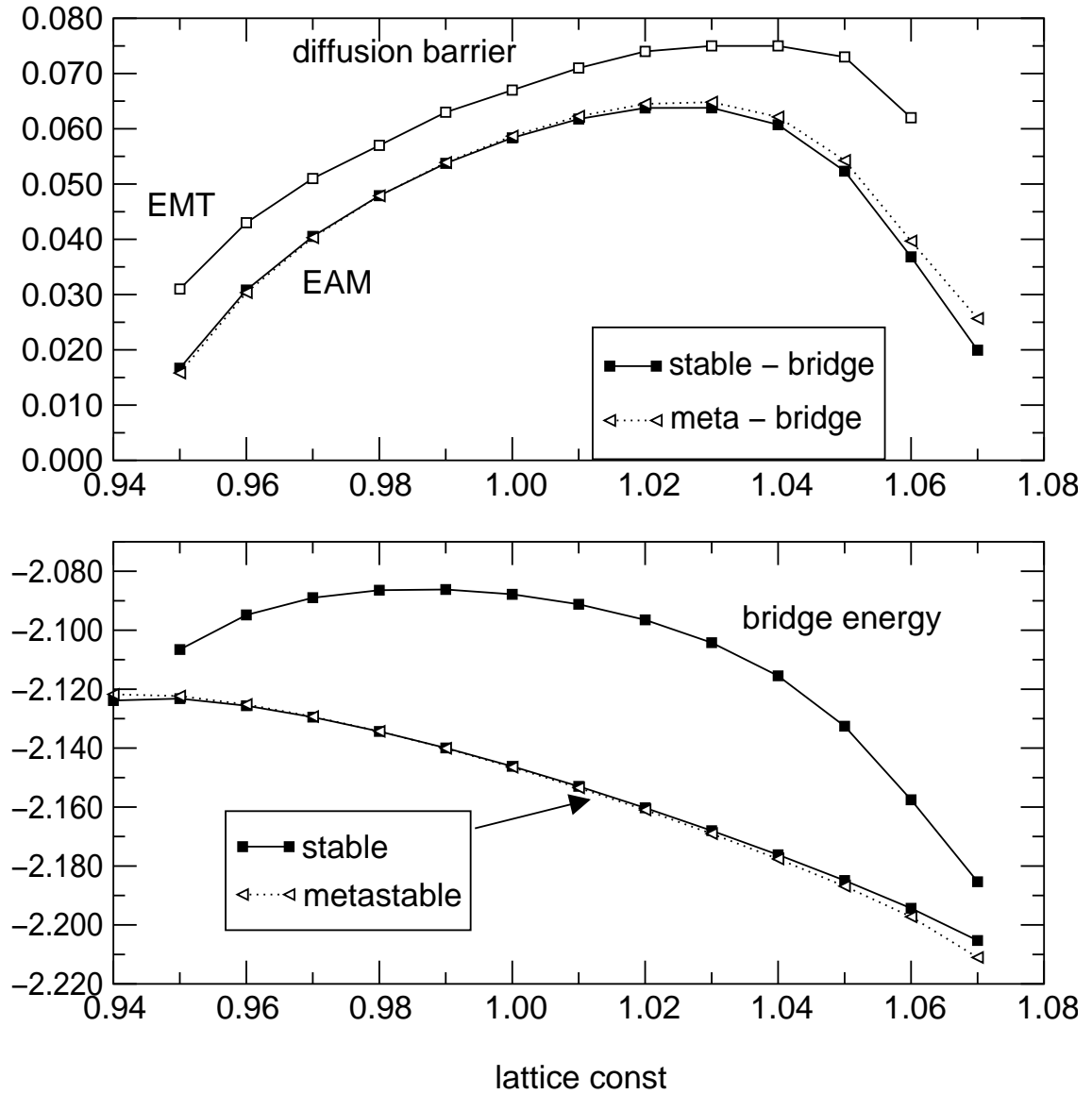


Figure 3.1: Diffusion barrier of Ag adatom on stressed Ag(111) substrate. a) Comparison of the diffusion barrier obtained by EAM potential and effective medium theory (from Ref. [16]). The barrier is plotted against the ratio of the stressed and equilibrium lattice constant. b) The effect of strain on the bridge energy and the stable and metastable energy of the same system. Note that around zero stress, the bridge energy is relatively constant, while the stable/metastable energy is changing.

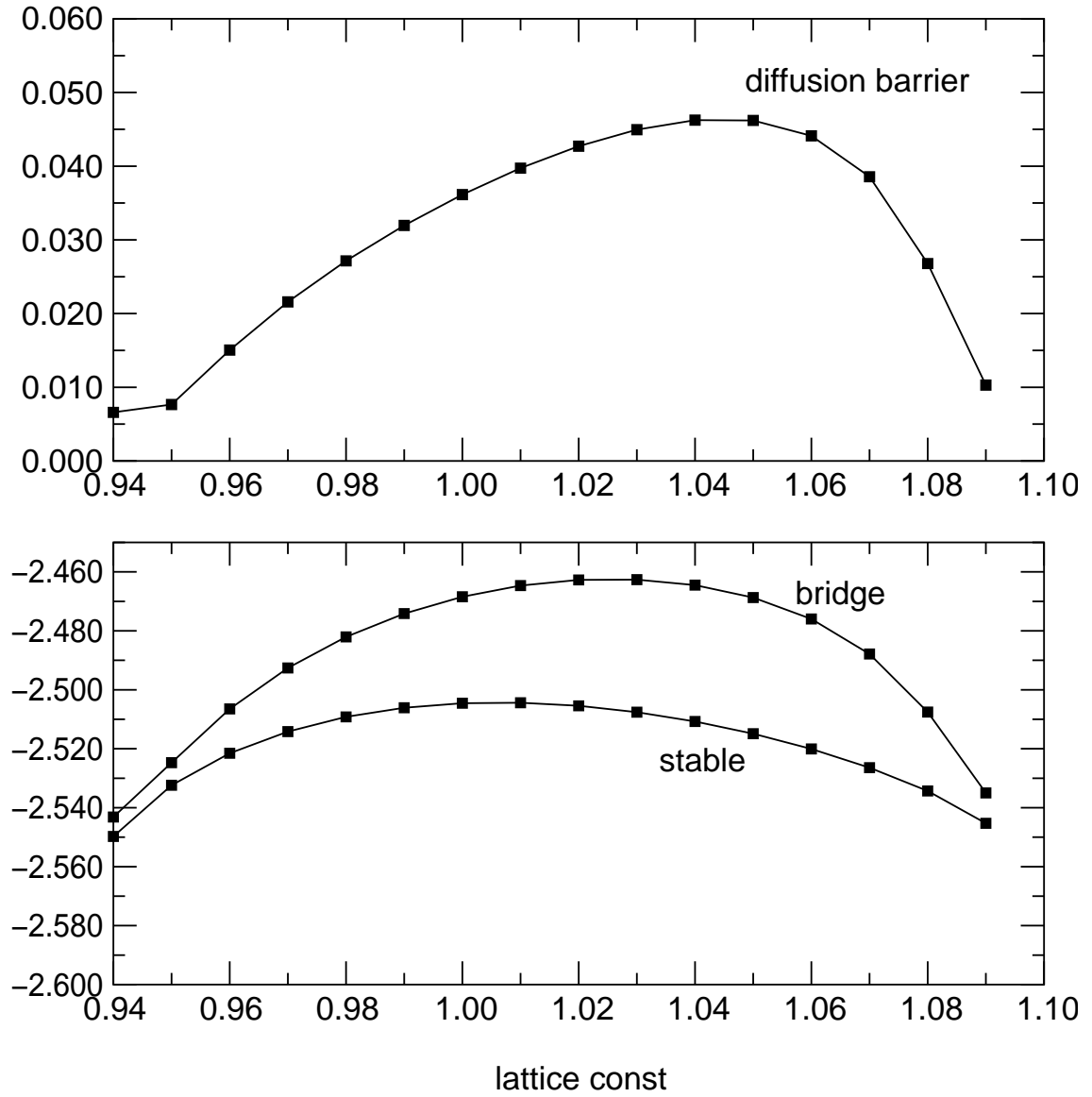


Figure 3.2: Diffusion barrier of Ag adatom on stressed Ni(111) substrate. a) diffusion barrier and b) bridge and stable energies as function of the ratio of the stressed and equilibrium lattice constant. This case the stable energy is constant near equilibrium, and the bridge energy is changing.

positions of the adatom, the configuration is shown on Fig. 3.3.

On Fig. 3.4 we plot the diffusion barriers of a Ag adatom on top of Ni(111) substrate, as a function of the distance from a Ag island of radius 4 atoms. The misfit between Ag and Ni is 16%, the Ag island is compressed. We had to select metals of this large misfit in order to see effects of the misfit on the system sizes computationally available —  $32^3$  in this calculation. There are two different barriers: one seen by an adatom diffusing away from the island, and a different one for approaching it. The oscillation is due to the nature of the lattice: on top of an fcc(111) lattice an adatom can be in the fcc position (stable) or hcp position (metastable). The diffusion barrier is measured between the bridge point and the stable or metastable site.

According to the results, near the island it is easier to diffuse away from a stable site, and easier to diffuse inward from a metastable site. The island does not have a strong attractive or repulsive long-range effect on the adatom. However if the adatom is very close, it can only diffuse inwards: it is captured by the island.

The small island of the previous result was pseudomorphic to the substrate. For larger islands this is not the case. Fig. 3.5 shows the diffusion barriers near an island of radius 7 atoms, which is already not pseudomorphic, as can be seen on Fig. 3.3. The distortion of the energy landscape is much larger in this case, and the attraction of the island can be felt at larger distances. The effect of the island is not only attraction (the outward barriers larger than the inward ones) but also enhancing diffusion near the island: the diffusion barriers in both direction are decreased. Probably this is due to the fact that the substrate near the compressed island is also compressed.

To check that how much of this effect is due to the presence of the compressed hetero-island, we repeated the previous calculation with homoepitaxial island: the

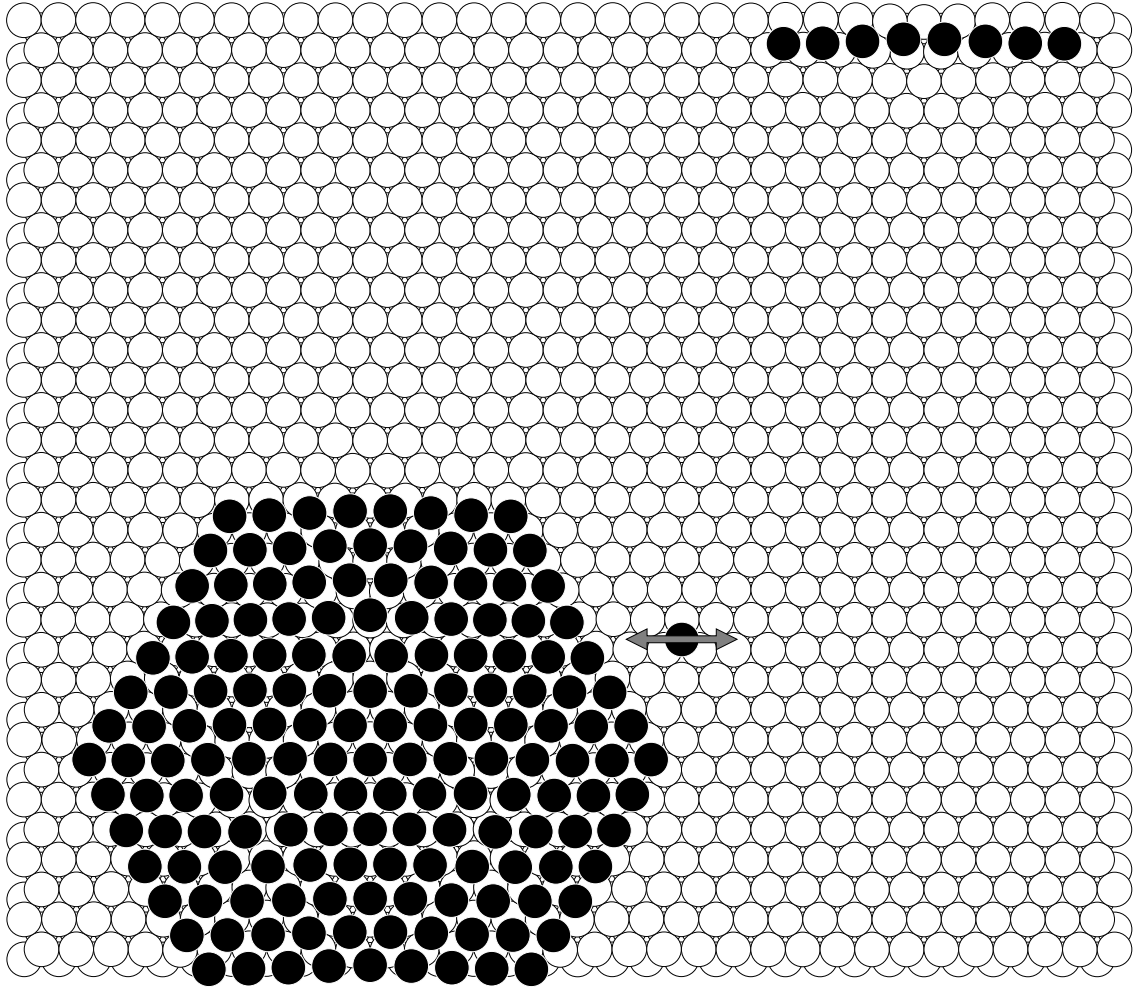


Figure 3.3: The configuration to measure the effect of an island on the energy landscape. White circles denote substrate atoms, black ones are the hetero atoms. The hexagonal island is of radius 7 on this figure, the black atoms on the top right corner are part of the island because of the periodic boundary conditions. The adatom is moved in the direction of the arrow.

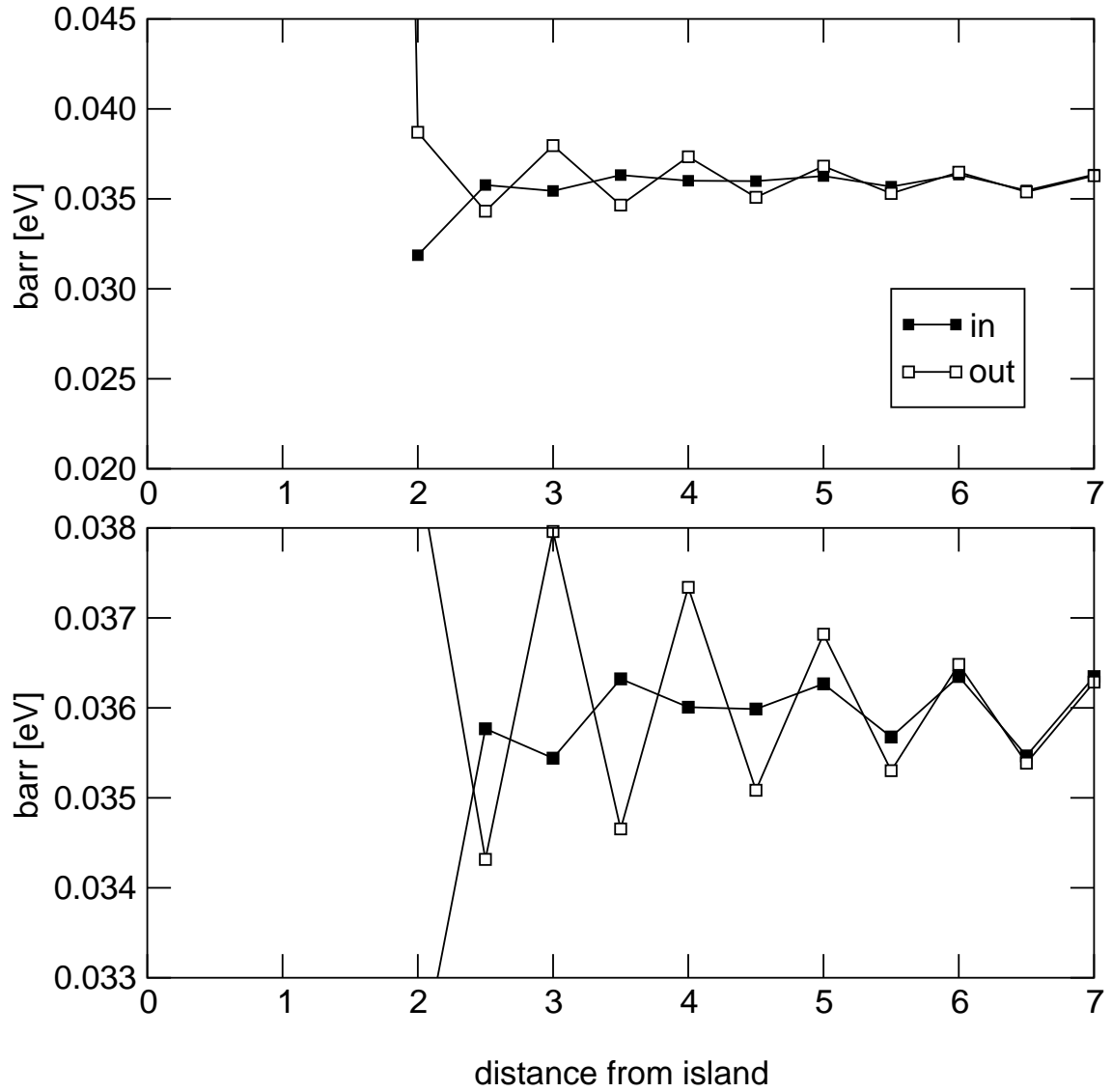


Figure 3.4: Diffusion barrier of Ag on Ni(111) near a small Ag island (radius is 4 atoms). The island is pseudomorphic. The bottom figure is magnification of the top figure around the equilibrium barriers.

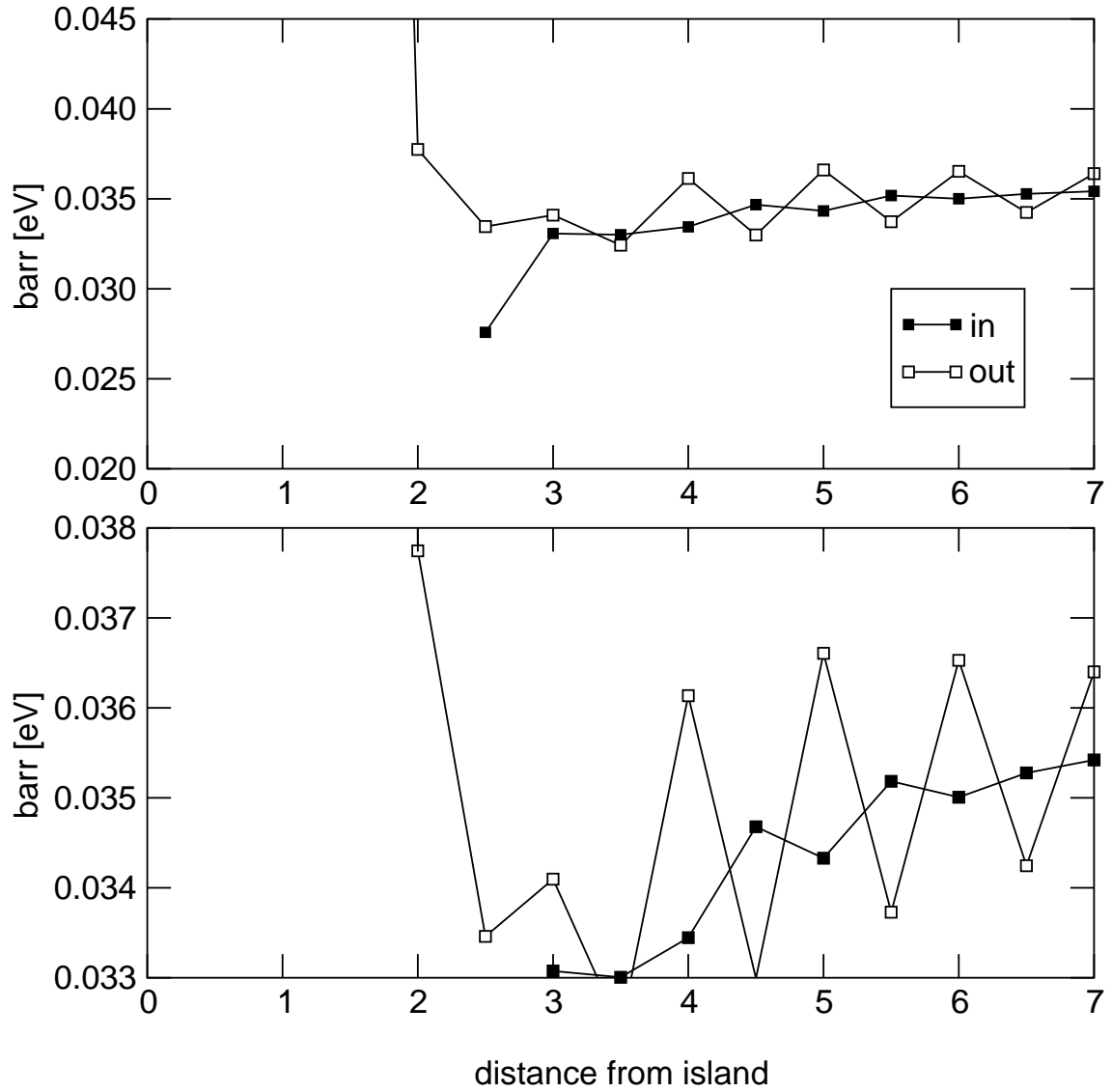


Figure 3.5: Diffusion barrier of Ag on Ni(111) near a large Ag island (radius is 7 atoms as in Fig. 3.3). The island is not pseudomorphic. The scale of the plots is the same as on the previous figure.

large Ag island has been replaced with same size Ni island. The obtained barriers (Fig. 3.6) show even smaller effect than the case of the small hetero-island. On a considerable range the energy landscape is deformed: the outward and inward directions are not equivalent (as in a sawtooth potential) but there is no global attraction or repulsion.

The detachment barrier from a strained island has also been measured. Fig. 3.7 shows the bonding energy as a function of island size, it is the same as detachment barrier up to its sign. The trend is decreasing barrier for larger islands.

It has to be noted that the bonding energy of the island of radius 5 is very different compared to the nearby sizes. The explanation is the following. The bonding energy is defined as the energy of the island with an adjacent adatom, the zero point is when the adatom is infinitely far away. The island of this size is at the borderline of pseudomorphic and not pseudomorphic islands. When we measured the energy of the island in itself, the relaxation converged to a pseudomorphic state, see Fig. 3.8. But when the adatom was added, this was enough perturbation that the system converged to a not pseudomorphic state (Fig. 3.9). Thus the addition of the adatom triggered a much lower energy state, hence the large negative bonding energy. It is possible that the bare island also has a lower energy non-pseudomorphic state, but we did not do a detailed search.

We also tried to obtain an energy landscape on top of an island. This was quite difficult, because the island atoms are very soft, deform very much in the presence of an adatom on top, and there is no well defined stable, metastable and bridge site. Fig. 3.10 depicts a case when a the adatom is in a deformed four-fold hollow site.

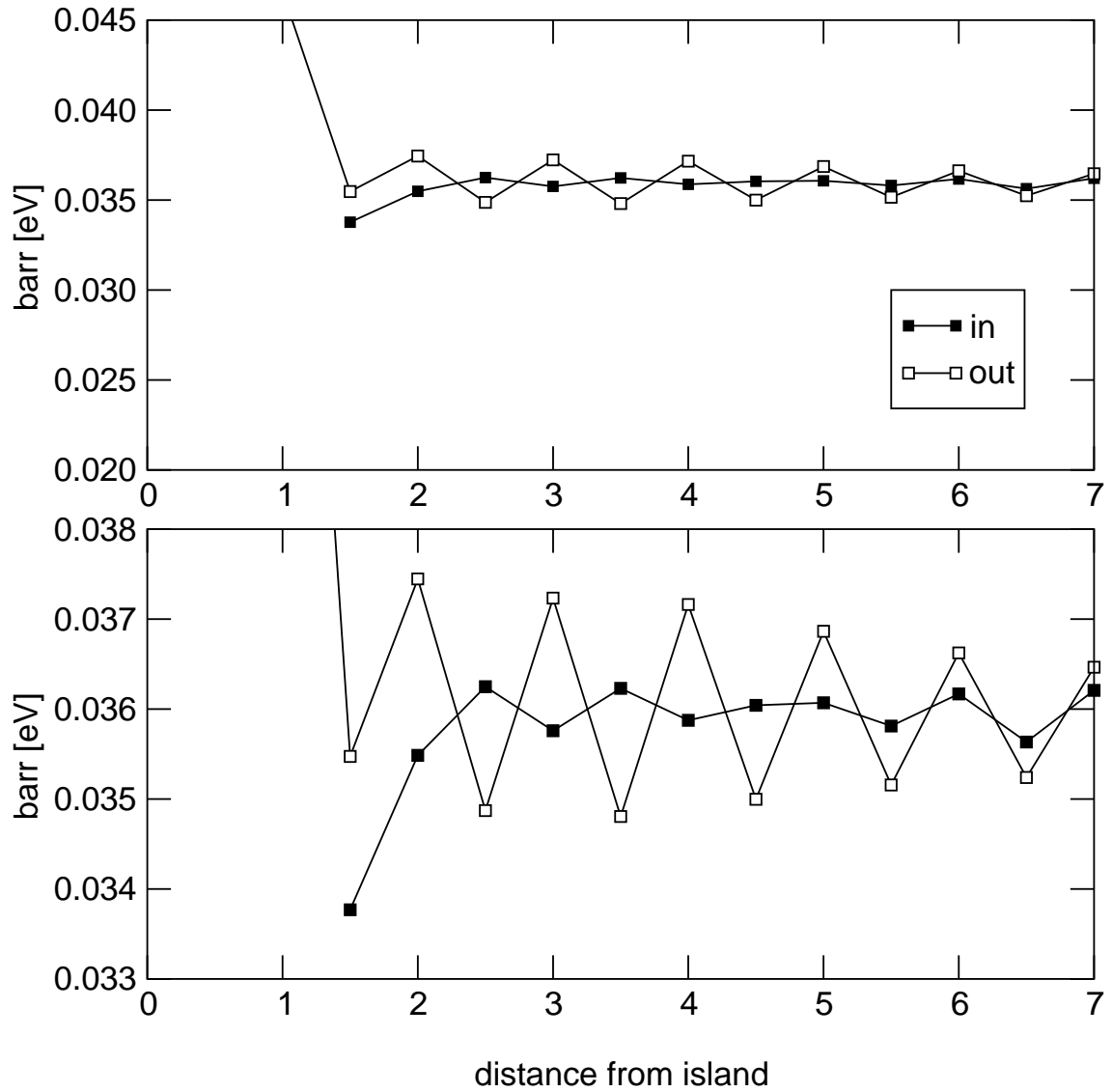


Figure 3.6: Diffusion barrier of Ag on Ni(111) near a large Ni island (radius is 7 atoms). Same scale as previous figure.

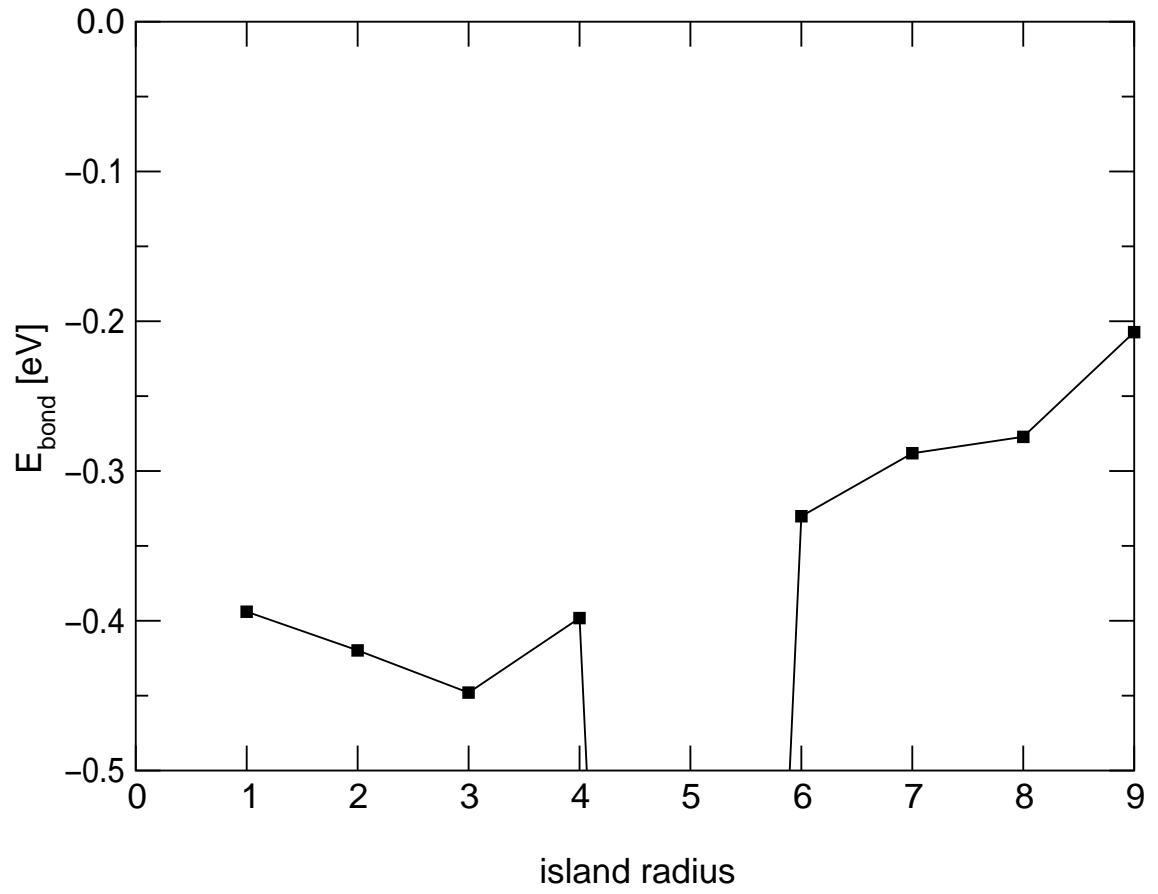


Figure 3.7: Bonding energy to strained Ag islands as a function of island radius. The case of radius=5 is explained in the text.

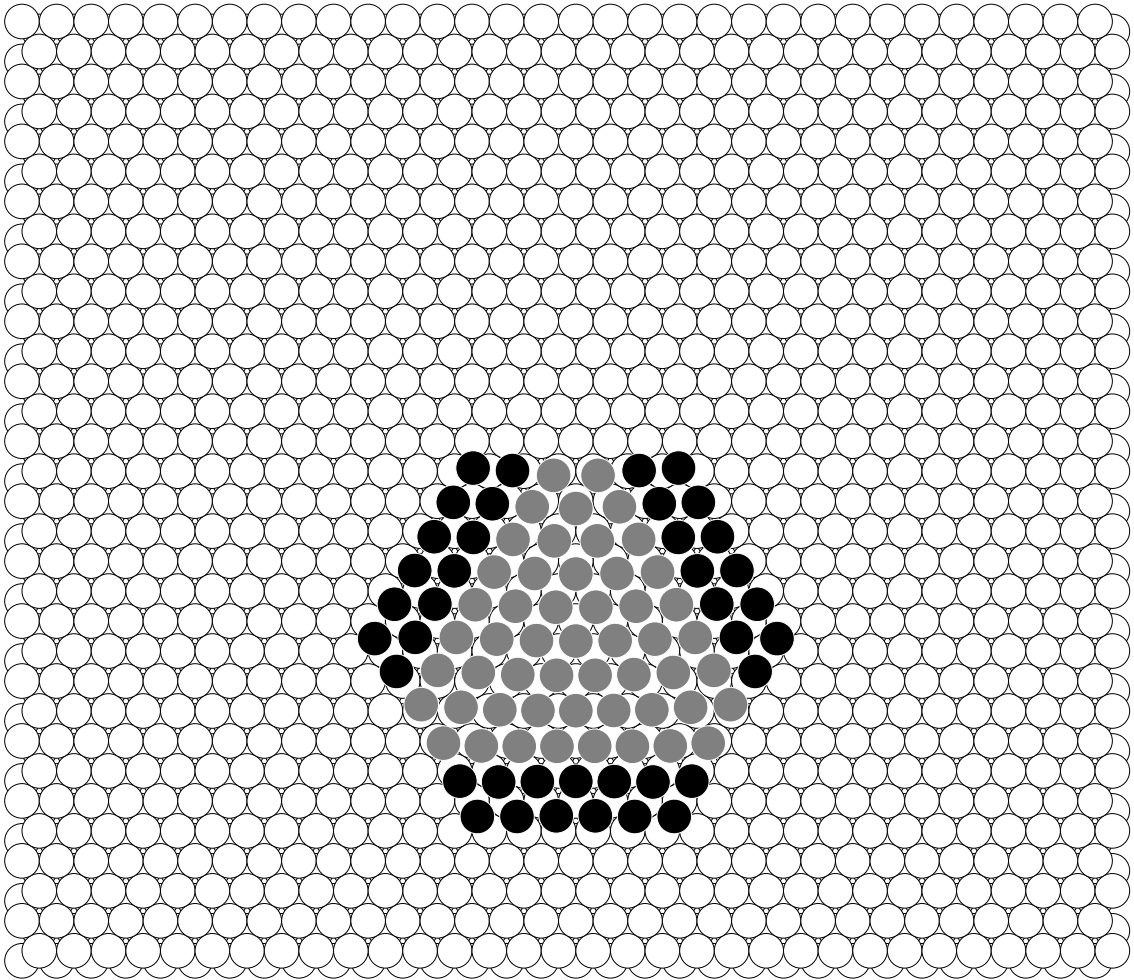


Figure 3.8: Relaxed island of radius 5. The “pseudomorphic atoms” are grey. (An atom is considered pseudomorphic if it is closer to the stable site extrapolated from the lattice than to other stable or metastable sites.) The majority of the island is pseudomorphic, only the edges are pushed out. Note the deformed edges.

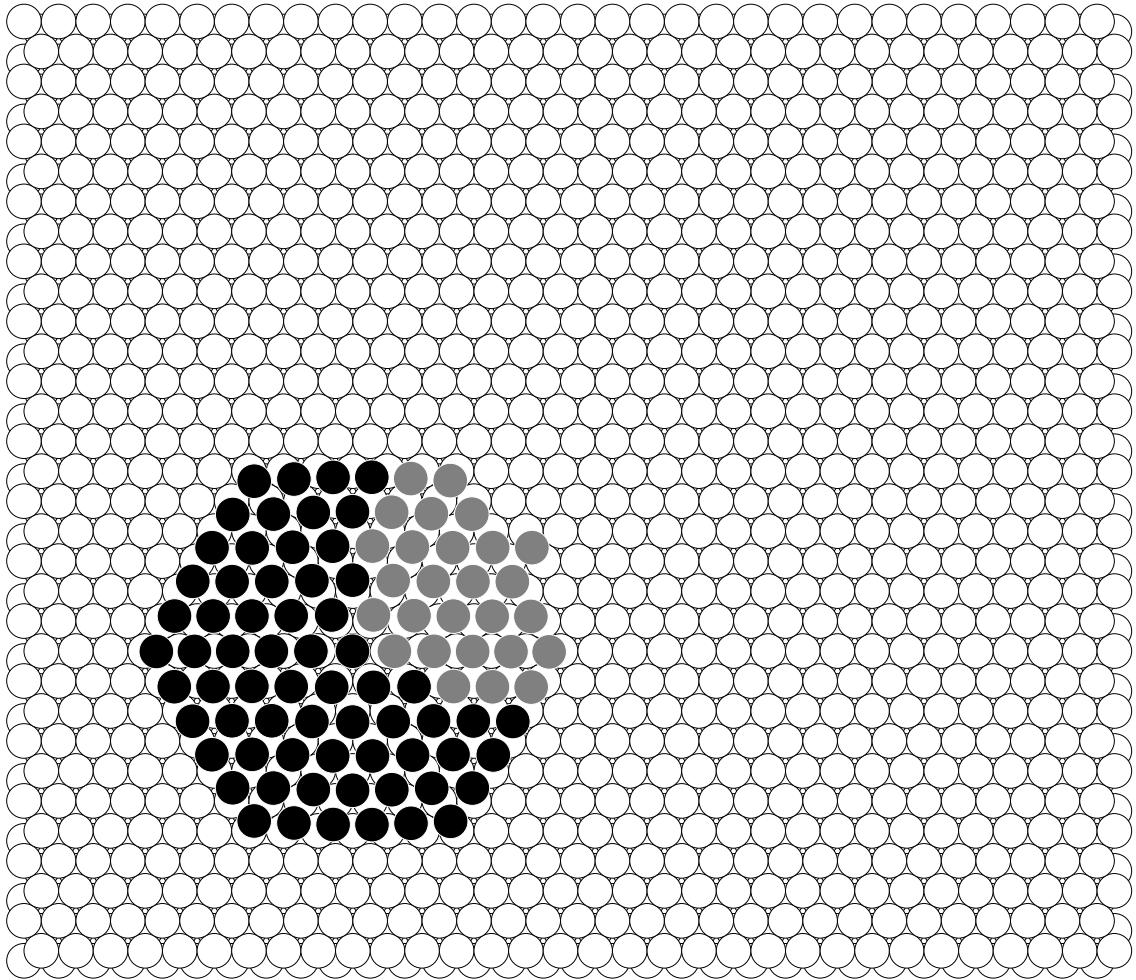


Figure 3.9: Relaxed island of radius 5 with adjacent adatom — compare with previous figure. The “pseudomorphic atoms” are grey. The perturbation of the adatom was enough that the nearby part of the island is pseudomorphic only. The other parts are also relaxed, with smooth dislocation network connecting the relaxed parts.

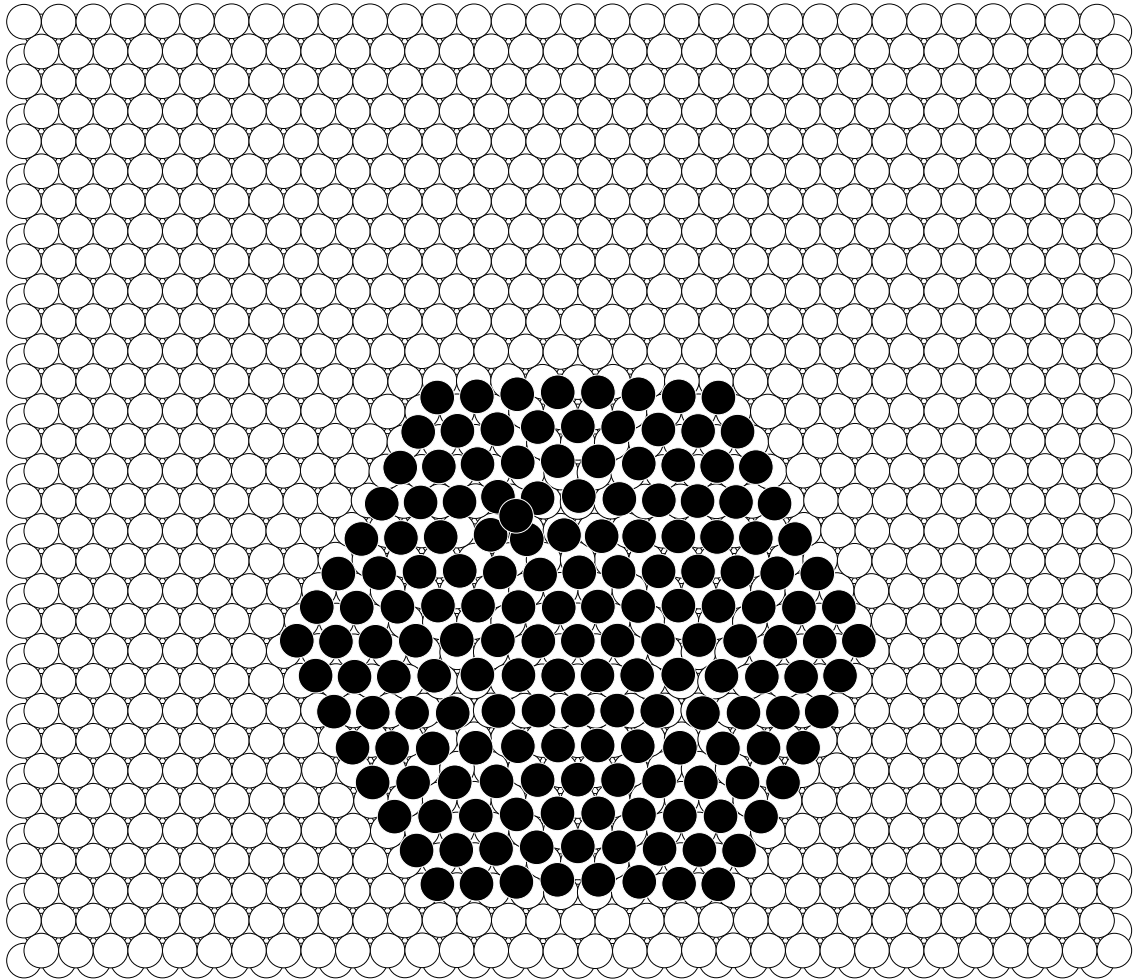


Figure 3.10: Unusual deformations like this four-fold hollow site occur on top of an island.

### 3.4 Summary

In this chapter we studied the elastic effects of heteroepitaxial islands on diffusion using atomistic simulations with EAM potential. Compressive strain enhances diffusion, small tensile strain hinders it, but large tensile strain also tend to enhance it. Whether the energy of the stable site changes or the bridge energy, depends on the system.

The energy landscape near a compressed island is deformed: the island attracts the adatom, and the diffusion is increased near the island. Even homoepitaxial island deforms the energy landscape, but the change is much smaller, and only the symmetry of the potential is broken.

The detachment barrier from a compressed island decreases with larger island size. The diffusion barriers on top of an island is hard to measure, because the island is soft and distorted near an adatom, there is no well defined diffusion path.

## References

- [1] A. Grossmann, W. Erley, J. B. Hannon, and H. Ibach, *Phys. Rev. Lett.* **77**, 127 (1996); A. Grossmann, W. Erley, J. B. Hannon, and H. Ibach, *Phys. Rev. Lett.* **78**, 3587 (1997).
- [2] F. C. Frank and J. H. van der Merwe, *Proc. Roy. Soc. London A* **198**, 205 (1949).
- [3] M. Volmer and A. Weber, *Z. Phys. Chem.* **119**, 277 (1926).
- [4] I. N. Stranski and Von L. Krastanow, *Akad. Wiss. Lit. Mainz Math.-Natur. Kl. Iib* **146**, 797 (1939).
- [5] see e.g. H. Röder, K. Bromann, H. Brune and K. Kern, *Surf. Sci.* **376**, 13 (1997).
- [6] R. Nötzel, J. Temmyo and T. Tamamura, *Nature* **369**, 131 (1994); R. Nötzel et al., *Appl. Phys. Lett.* **65**, 2854 (1994).
- [7] J. Tersoff, C. Teichert, and M. G. Lagally, *Phys. Rev. Lett.* **76**, 1675 (1996).
- [8] Y. Ebiko, et al., *Phys. Rev. Lett.* **80**, 2650 (1998).
- [9] B. G. Orr, D. Kessler, C. W. Snyder, and L. M. Sander, *Europhys. Lett.* **19**, 33 (1992).
- [10] M. Schroeder and D. E. Wolf, *Surf. Sci.* **375**, 129 (1997).
- [11] H. T. Dobbs, D. D. Vvedensky, A. Zangwill, J. Johansson, N. Carlsson, and W. Seifert, *Phys. Rev. Lett.* **79**, 897 (1997).
- [12] H. T. Dobbs, D. D. Vvedensky, and A. Zangwill, *Appl. Surf. Sci.* **123/124**, 646 (1998).
- [13] G. Ehrlich and F.G. Hudda, *J. Chem. Phys.* **44**, 1039 (1966); R.L. Schwoebel, *J. Appl. Phys.* **40**, 614 (1969).
- [14] M. S. Daw and M. I. Baskes, *Phys. Rev. B* **29**, 6443 (1984)
- [15] S. M. Foiles, M. I. Baskes, and M. S. Daw, *Phys. Rev. B* **33**, 7983 (1986).
- [16] H. Brune, K. Bromann, H. Röder, and K. Kern, *Phys. Rev. B* **52**, R14380 (1995).

## CHAPTER 4

# Scaling and river networks: A Landau theory for erosion

The research presented in this chapter was done with Professor Leonard M. Sander; the numerical work was done by me, and the analytical work by Professor Leonard Sander. It was published in *Phys. Rev. E* **56**, R5 (1997).

We propose a coarse-grained theory for the formation of a river network in the form of a Langevin equation for the erosion of the landscape coupled to a conservation law for the surface water flow. We claim that this is the universal form for the large-scale behavior. We show by simulations of a discrete model which represents the same dynamics that the slope-area law, the basin size distribution law, and Horton's laws agree with real rivers. We discuss the relationship to optimal channel networks and to self-organized criticality.

Natural river networks have attracted a good deal of attention in the physics and geophysics communities, and a large number of models have appeared which attempt to give an explanation for the remarkable statistical properties of these systems [1, 2, 3, 4]. The spirit of much of this work is to try to abstract from the details of the geological processes a simple description which will account for the large-scale, coarse-grained properties of the network. In this chapter we present a new model of this type. Our model is similar to that of Inaoka and Takayasu [2] and of Sinclair and Ball [3] but also has significant differences. Our theory is intended to serve as a unified model of erosion and is based on a continuum formulation which we believe to capture the important features that survive on coarse-graining. If we are correct, much of the previous work will have the same large-scale properties as the work we present here.

## 4.1 Statistical properties of river networks

The remarkable statistical properties of river basins have been known for some time [5, 6]. We will focus on a few of the laws which we consider to be central, and which we have verified for the model to be presented. The most important of these is the slope–area law: which was derived from field observations [7]: the slope of the river bed  $s$  scales with a power of the basin area  $Q$ :

$$s \sim Q^{-\theta} \tag{4.1}$$

where the value of the exponent  $\theta \approx 0.5$  has been carefully measured [7]. The distribution of the drainage area also obeys power law:  $P \sim Q^{-\beta}$  where  $P$  is the fraction of the landscape for which the drainage area is larger than a given value  $Q$ . The value of the exponent is  $\beta \approx 0.43$  [4, 8].

The best known of the statistical properties are Horton’s laws [9] which are relations between the number and length of different parts of the network. They say, in effect, that the streams form a random branching fractal. Consider the Strahler scheme for ordering the streams (i.e., up ends of the streams are order 1; when two or more streams of same order join, the order increases by one; when streams of different order join, the higher stream order prevails.) Let  $N_\omega$  denote the number of streams of order  $\omega$ , and  $L_\omega$  their averaged length. Horton’s laws state that the branching ratio  $R_B = N_\omega/N_{\omega+1}$  and the length ratio  $R_L = L_{\omega+1}/L_\omega$  are independent of  $\omega$ . The fractal dimension [10] of the network is given by  $d_c \cdot \log(R_B)/\log(R_L)$ , where  $d_c$  is the fractal dimension of the individual streams [11]. For many networks the values  $R_B \approx 4$ ,  $R_L \approx 2$  are found [9] along with  $d_c \approx 1.1 - 1.2$  [11, 12]. Our model will turn out to obey all these laws.

## 4.2 The model

We start with the observation that landscapes seem to have scale invariance [13]: they are close to being self-affine fractals. This means that if we consider a topographic map and rescale the coordinates,  $\mathbf{r}$  on the map so that  $\mathbf{r} \mapsto b\mathbf{r}$ , and the height differences by  $\Delta h \mapsto b^\alpha \Delta h$ , where  $\alpha < 1$  we get a statistically identical landscape. Since erosion by rivers are among the processes that form landscapes, the scale invariant statistical properties of mature river networks should have a close connection with the scale invariance of the landscape.

Now let us focus on the erosion process, and make some simplifying assumptions (which could be easily modified): we assume that the only source of water is from a uniform rainfall and neglect underground flows. The land is geologically uniform and initially structureless. We also assume that the material washed away by the

river is carried entirely to the sea, and is not redeposited. This is the limit of slow erosion and fast flows.

To formulate the coarse-grained erosion law we use an argument which is standard in the theory of random rough surfaces [14] and which, in turn, is based on the classic work of Landau and Ginsburg [15]. We note first that the absolute height of the landscape should play no role in the local erosion. Thus we write:

$$\partial h/\partial t = F(\nabla h, \nabla^2 h, |\nabla h|^2, \dots) + \eta(\mathbf{r}, t) \quad (4.2)$$

where  $\eta(\mathbf{r}, t)$  is a noise term which accounts for small scale random processes.

Further, we argue that the functional,  $F$ , is analytic in the gradients: it is the result of averaging over local fluctuating processes<sup>1</sup>. Now we are interested in large-scale statistical properties. When we rescale a self-affine surface the gradients *decrease*. Thus we should be able to expand  $F$  in a power series:

$$F = A + \mathbf{B} \cdot \nabla h + C|\nabla h|^2 + D\nabla^2 h + \dots \quad (4.3)$$

We can interpret these terms. The first is a uniform change in height which might correspond to geological uplift. For our case we can set  $A = 0$ . The second term involves a vector,  $\mathbf{B}$ , which introduces a preferred global direction of water flow. Since local flows have no preferred direction (except down) we must set  $\mathbf{B} = 0$ . The third term corresponds to erosion proportional to  $s^2$ , the squared slope. This sort of law has been considered in the literature [16] along with others. It has a special significance since it is the lowest order term, and thus the dominant one when we rescale. The last one which we keep can be thought of sedimentation and smoothing:

---

<sup>1</sup>This is the weakest part of our argument. For near-equilibrium dynamics  $F$  is related to the Landau free energy and is necessarily analytic. For our case the rigorous justification of the method is less evident. We do get interesting results, as we will see.

it rounds hilltops and fills valleys [17]. The equation for the landform is:

$$\partial h/\partial t = C|\nabla h|^2 + D\nabla^2 h + \dots + \eta(\mathbf{r}, t). \quad (4.4)$$

This is the KPZ equation [18] which has been extensively studied. There has been a previous application of this equation to river networks [19]. In this form it is clear that the equation can generate self-affine landscapes. The higher order terms represented by the dots are *irrelevant* in the sense that they disappear upon rescaling.

The other ingredient in our theory is the water. We define  $\mathbf{q}$  as the flux of water per unit width of landscape. Our assumptions (uniform rainfall and no ground water) imply that  $q \propto Q$ , where  $Q$  is the basin area. The vector  $\mathbf{q}$  satisfies the following:

$$\nabla \cdot \mathbf{q} = R \quad (4.5)$$

where  $R$  is the rainfall/unit area. Further, water runs downhill. Thus:

$$\hat{\mathbf{q}} \equiv \mathbf{q}/q \propto -\nabla h. \quad (4.6)$$

Finally, we insist that there be no erosion in the absence of water. That means that the coefficient,  $C$  of the erosion term must be a function of  $q$ , that vanishes as  $q \rightarrow 0$ . There is no particular reason why  $C$  should be analytic, so we propose on the basis of simplicity, an erosion rate linear in the flow:  $C = -cq$ . Putting this all together we get:

$$\partial h/\partial t = -cq|\nabla h|^2 + D\nabla^2 h + \eta(\mathbf{r}, t). \quad (4.7)$$

Equations (4.5, 4.6, 4.7) constitute our Landau theory.

Formulations similar to this one have been proposed before. A theory of this type was given by Smith and Bretherton [20] some time ago, and discussed by Tarboton et al. [6] in the context of stream initiation. Our equations differ from theirs in

that they conserve sediment so that the right-hand side of Eq. (4.7) is of the form  $-\nabla \cdot [\hat{\mathbf{q}}q^m s^n]$ . Our Eq. (4.7) corresponds (up to an irrelevant term) to  $m = n = 2$ . The recent work of Sinclair and Ball [3] proposes a set of equations like ours with a term of the form  $q^a s^b$  of which our equation is a special case. (As we will see, our solution to these equations is quite different from that of Ref. [3]).

Because the landform generated by Eq. (4.7) is coupled to the water flow (which changes with the landscape) the solutions to the coupled set are quite unlike those of the ordinary KPZ equation. With suitable boundary conditions, the landscape will approach a dynamic steady state where the river network and the landform do not change. This steady state is a feature of many of the models which have been proposed. It corresponds to the simple statement that large rivers are long-lived<sup>2</sup>.

To understand the steady state we use the approach of Smith and Bretherton [20] who point out that an obvious kind of steady state is one in which the erosion is uniform everywhere. If we neglect smoothing and noise (as we will do from this point on), we can write:

$$\partial h / \partial t = \text{Const.} = -cq|\nabla h|^2 \quad (4.8)$$

which amounts to having  $s \propto 1/q^{1/2}$ , that is, exactly the slope-area law<sup>3</sup> of Eq. (4.1). If this state is attained it will have the observed slope-area law in a natural way, and is certainly stationary<sup>4</sup>. It remains to show that featureless landscapes tend towards this state, and that it is stable. To investigate this question we turn to

---

<sup>2</sup>We are not considering the meandering instability which causes large rivers to change course.

<sup>3</sup>Since only the ratio of the exponents of  $q$  and  $|\nabla h|$  is significant here, other combinations like  $q^2|\nabla h|^4$  would yield the same slope-area law. The choice of the exponents in Eq. (4.7) is motivated by finding the lowest order permitted term that produces the right slope-area relation.

<sup>4</sup>In contrast, Sinclair and Ball consider another kind of state in which the height at each point decreases as a power law. This may be appropriate for the late stages of erosion (the formation of a peneplain) where the boundary conditions dominate the behavior throughout the river basin. We give a more local approach. The resulting slope-area law is different in the two cases.

numerical solutions of a discrete model which is an approximate realization of our set of equations.

### 4.3 Numerical simulations

Our discrete model is very similar to that of Refs. [2, 3] (though our boundary conditions are not). We consider a triangular lattice of mesh points which represents our landscape. Every point has two variables: the height  $h$  and the flow  $q$ . The water flows on the bonds of the lattice, and every node has one outflowing bond, the one which is the steepest. At every time step (doing parallel updates) the drainage area is calculated from the landscape, and the height is decreased according to the erosion rule:  $\Delta h = -|\nabla h|^2 \cdot q \cdot \Delta t$ . The gradient is measured on the outflowing edge. If there are no lakes in the initial height distribution (no nodes with all neighbors higher than itself), then using sufficiently small  $\Delta t$ , no lakes are created. Thus we were able to ignore the special treatment of lakes, which are generally present only in the initial stages of the erosion process, and do not affect the stationary state.

Initially the landscape is a hillside with a little noise:  $h(x, y, t=0) = s_0 \cdot (y + dy \cdot rnd(x, y))$ , where  $y$  is the North–South coordinate,  $s_0$  is the initial slope of the hillside,  $rnd()$  is uniform random number from  $[0, 1]$ , and  $dy$  is the lattice constant. These initial conditions ensure the absence of lakes. The boundary conditions are periodic in the East–West direction, infinite wall on the North side (this is the upper end of the hillside), and outflowing on the South side. The slope of the outflowing edges on the outflowing side are taken to be fixed. With these boundary conditions the stationary state is such that the whole landscape erodes with the same rate everywhere. We can think of this as representing a plateau which has been upthrust and which starts to erode. This boundary condition is in contrast with fixed *height*

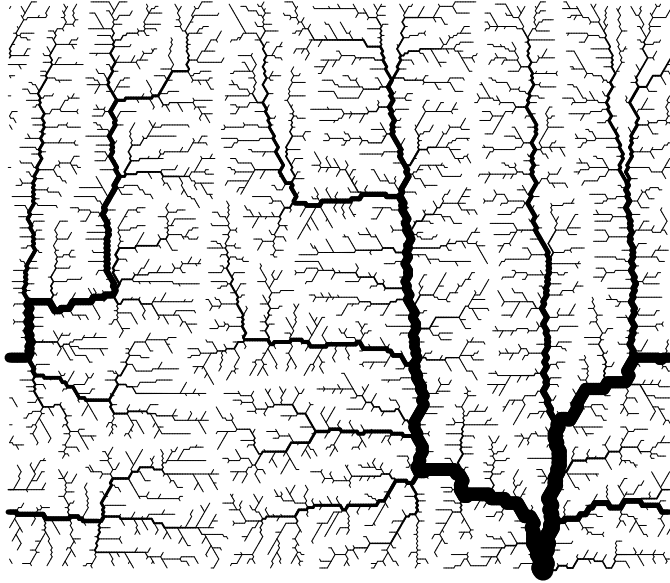


Figure 4.1: A typical stationary river network on a 256 x 256 triangular lattice. For better visualization, the stream is drawn with line width proportional to the square root of the discharge. Only streams with discharge  $q \geq 10$  are displayed.

at the outflowing edge used by other authors [2, 3]: in that case the stationary state occurs when nearly all of the material has been washed away and a different slope-area law holds [3].

In our simulations we find that the initial stages of river formation corresponds to rivers valleys that start at the bottom edge and elongate, compete, and eventually reach a stationary state with one large river. Fig. 4.1 depicts a typical stationary river network. Taking the lattice constant to be unit length, the slopes at the outflowing edge also one, and measuring the discharge as the number of the nodes in the basin area, the rivers reach the stationary state at around unit time. The corresponding landscape is shown on Fig. 4.2.

The following statistical results were obtained by averaging 20 independent simulations of size 256 x 256. As expected, the slope–area law (Fig. 4.3) holds with

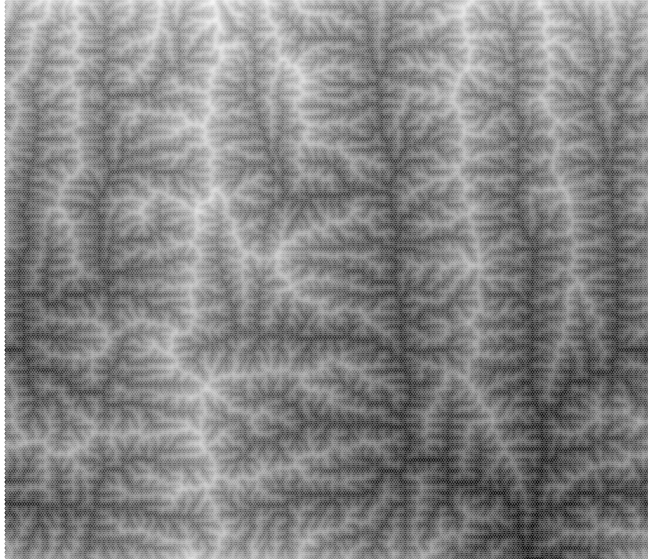


Figure 4.2: The landscape created by the river of Fig. 4.1. The grayscale is proportional to height, with white corresponding to high.

exponent  $1/2 \pm 10^{-6}$ . The great accuracy is understandable if we accept that the slope–area law is an attractive fixed point of the dynamics: if any node does not satisfy the law, it will erode faster or slower than its neighbors towards a height which satisfies the law. The cumulative distribution of the basin area is depicted on Fig. 4.4. The value of the exponent is  $\beta = 0.45 \pm 0.02$ . Horton’s laws are shown on Fig. 4.5, the branching ratio is  $R_B = 4.0 \pm 0.2$ , the length ratio is  $R_L = 2.3 \pm 0.1$ . The dimension of the individual streams  $d_c$  is measured [12] from the scaling of the average river length with the system size:  $\langle l_i \rangle \sim L^{d_c}$  (where  $l_i$  is the distance of site  $i$  from the root on the network). Using  $L = 64, 128$  and  $256$ , we obtained  $d_c = 1.05$ , giving network fractal dimension  $1.85 \pm 0.15$ . This value of the fractal dimension is somewhat lower than the expected 2 for space filling networks. The probable explanation is the low value of  $d_c$ : in our hillside initial conditions the rivers are “stretched” in North–South direction, making them more linear ( $d_c$  closer to 1).

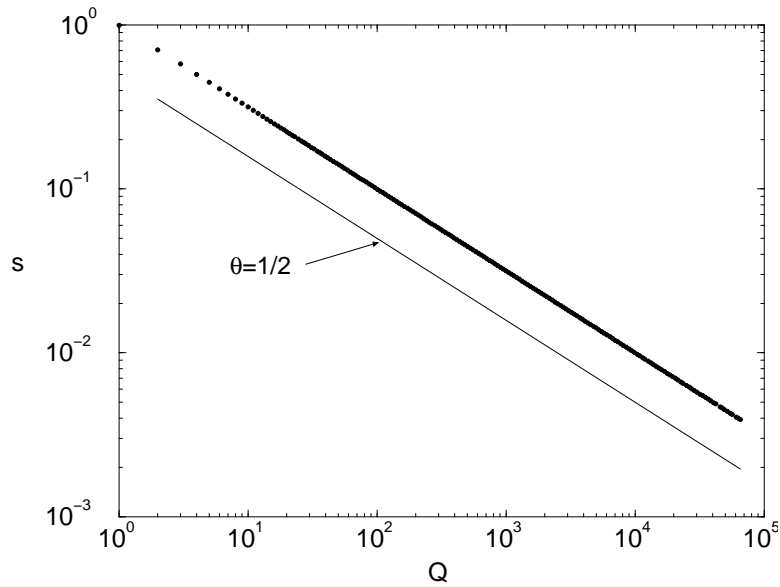


Figure 4.3: The slope–area law obtained by the simulation. The exponent is  $\theta = 1/2 \pm 10^{-6}$ . The great accuracy is the consequence of the attractive nature of the fixed point of the dynamics.

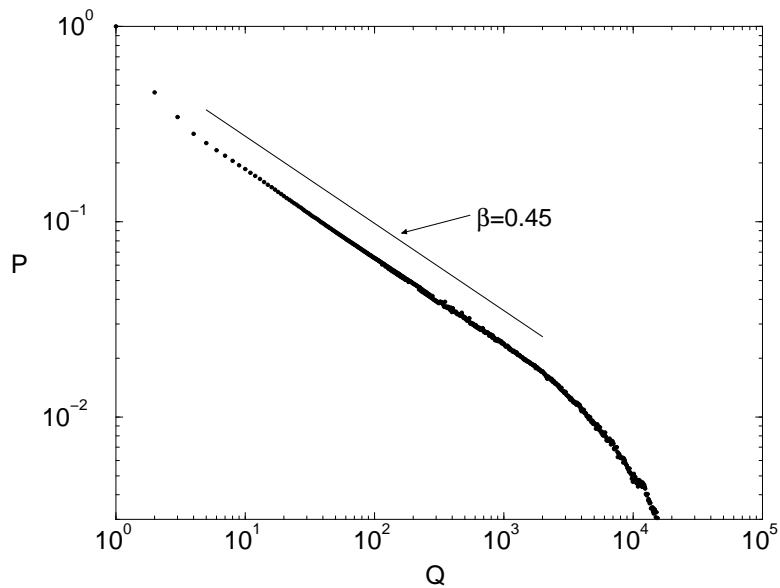


Figure 4.4: The cumulative basin area distribution  $P(Q)$  (the fraction of the landscape for which the drainage area is larger than a given  $Q$ ). The value of the exponent,  $\beta = 0.45 \pm 0.02$  agrees with Ref. [4].

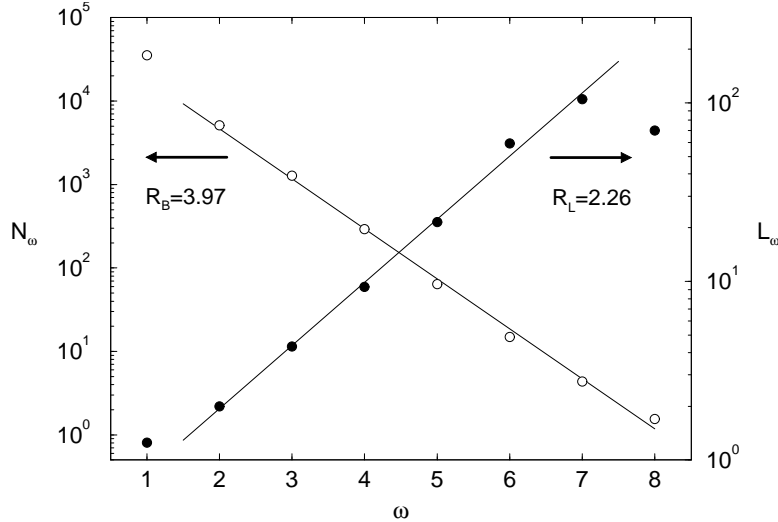


Figure 4.5: Horton's laws for the branching ratio ( $\circ$ ):  $R_B = 4.0 \pm 0.2$ , and the length ratio ( $\bullet$ ):  $R_L = 2.3 \pm 0.1$ . With stream dimension  $d_c = 1.05$ , the fractal dimension of the network is  $D = d_c \cdot \log(R_B)/\log(R_L) = 1.85 \pm 0.15$ , somewhat lower than the expected space filling  $D = 2$ .

There is another approach [4, 21] to the problem of river networks which appears quite different from ours, namely the idea that rivers are *optimal channel networks* (OCN's): connected branching patterns which minimize a functional that represents dissipation. It is well known that for systems far from equilibrium no functional exists in general which gives the dynamics in the usual sense that  $\partial h/\partial t = \delta\mathcal{F}/\delta h$ . If there were such a functional we could understand OCN's by noting that  $\partial h/\partial t = 0$ , the stationary state, would occur if  $\mathcal{F}$  is at a minimum. However, our equations are not of this form.

The solution to this quandary was given by Sinclair and Ball [3] who point out that a functional can exist which gives the stationary state, but not the complete dynamics. It is easy to see that the height function,  $h$ , and flow  $\mathbf{q}$  which minimize:

$$\mathcal{F}[h, \mathbf{q}] = \int \left\{ h \cdot (\nabla \cdot \mathbf{q} - R) + q^{1/2} \right\} d^2x. \quad (4.9)$$

obey both Eq. (4.5) and Eq. (4.1). However this variational principle does not

produce the dynamics (Eq. (4.7)). There is no free energy which would produce the dynamics of the initial stages of the erosion.

In the erosion process there are sudden large-scale events which have some similarity with the avalanches of self-organized critical (SOC) systems [22]. In fact, there is a formulation of SOC dynamics [23] which resembles ours in that it involves a Langevin-like equation whose parameters are a dynamical variable (cf.  $C = -cq$ ). However, our theory does not represent SOC processes, though there are similarities. The events in our system which are most like avalanches are river basin capture: when part of the basin area gets connected to another river. These change a macroscopic part of the flow pattern and are fast and nonlocal like avalanches, and they are essential during the evolution of the river network. But they completely disappear from the stationary state, and are not dominant for the formation of the large-scale structures. In SOC the avalanches are the only means to transmit information between the different parts of the system, and dominate any large-scale structure. In our case it is the river network itself, while eroding slowly, which transmits information.

#### 4.4 Summary

In summary, our treatment of river networks differs from earlier work in that it emphasizes the properties of the dynamics which should survive coarse-graining. We make a strong claim, that the dynamics given by Eq. (4.5, 4.6, 4.7) is a universal theory for the large-scale structure. We have shown that, at least, there is a reasonably satisfactory agreement with the empirical statistical laws that are gleaned from field observations of real rivers. We hope that generalizations of our work to allow ground water, storms, etc., could shed some light on how these processes affect landscapes, and could even, in the best case, give useful information on, for example,

the statistics of floods.

We would like to thank F. Mackintosh, P. Olmsted, and D. Turcotte for useful discussions. This work was supported by DOE grant DE-FG02-95ER45546.

## References

- [1] R. L. Leheny and S. R. Nagel, *Phys. Rev. Lett.* **71**, 1470 (1993); S. Kramer and M. Marder, *Phys. Rev. Lett.* **68**, 205 (1992); T. Sun, P. Meakin and T. Jossang, *Phys. Rev. E* **51**, 5353 (1995).
- [2] H. Inaoka and H. Takayasu, *Phys. Rev. E* **47**, 899 (1993).
- [3] K. Sinclair and R. C. Ball, *Phys. Rev. Lett.* **76**, 3360 (1996).
- [4] A. Rinaldo *et al.*, *Phys. Rev. Lett.* **76**, 3364 (1996).
- [5] D.L. Turcotte, *Fractals and chaos in geology and geophysics* (Cambridge University Press, 1992);
- [6] D. G. Tarboton, R. L. Bras and I. Rodriguez-Iturbe, *Geomorphology* **5**, 59 (1992)
- [7] L. B. Leopold and T. Maddock, *U.S. Geol. Surv. Prof. Paper* 252 (1953).
- [8] I. Rodriguez-Iturbe, R. L. Bras, E. Ijjasz-Vasquez, and D. G. Tarboton *Water Resour. Res.* **28**, 988 (1992).
- [9] R. E. Horton, *Geol. Soc. Am. Bull.* **65**, 275 (1945); A. E. Scheidegger, *Water Resour. Res.* **4**, 167 (1968); **4**, 1015 (1968); D. G. Tarboton, R. L. Bras and I. Rodriguez-Iturbe, *Water Resour. Res.* **24**, 1317 (1988).
- [10] J. G. Masek and D. L. Turcotte, *Earth and Planet. Sci. Lett.* **119**, 379 (1993).
- [11] D. G. Tarboton, R. L. Bras and I. Rodriguez-Iturbe, *Water Resour. Res.* **26**, 2243 (1990).
- [12] S. S. Manna and B. Subramanian, *Phys. Rev. Lett.* **76**, 3460 (1996).
- [13] B. B. Mandelbrot, *The fractal geometry of nature* (Freeman, San Francisco, 1982); A. Czirók, E. Somfai and T. Vicsek, *Phys. Rev. Lett.* **71**, 2154 (1993).
- [14] A.-L. Barabási and H. E. Stanley, *Fractal concepts in surface growth* (Cambridge Univ. Press, 1995).
- [15] L. D. Landau and E. M. Lifshitz, *Statistical physics* (Pergamon Press, 1980).
- [16] J. C. Luke, *J. Geophys. Res.* **77**, 2460 (1972); **79**, 4035 (1974).
- [17] W. E. H. Culling, *J. Geol.* **68**, 336 (1960); **71**, 127 (1963).
- [18] M. Kardar, G. Parisi, and Y.-C. Zhang, *Phys. Rev. Lett.* **56**, 889 (1986).
- [19] D. Sornette and Y.-C. Zhang, *Geophys. J. Int.* **113**, 382 (1993).
- [20] T. R. Smith and F. P. Bretherton, *Water Resour. Res.* **8**, 1506 (1972).

- [21] E. J. Ijjasz-Vasquez *et al*, *Adv. Water Resources* **16**, 69 (1993).
- [22] P. Bak, C. Tang and K. Wiesenfeld, *Phys. Rev. Lett.* **59**, 381 (1987).
- [23] L. Gil and D. Sornette, *Phys. Rev. Lett.* **76**, 3991 (1996).

## CHAPTER 5

# Diffusion-limited aggregation and viscous fingering in a wedge: Evidence for a critical angle

The research presented in this chapter was done with D. A. Kessler, Z. Olami, J. Oz, I. Procaccia, and Leonard M. Sander; large part of the numerical work was done by me, while the analytical work was shared between the collaborators. It was published in *Phys. Rev. E* **57**, 6913 (1997).

We show that both analytic and numerical evidence points to the existence of a critical angle of  $\eta \approx 60^\circ - 70^\circ$  in viscous fingers and diffusion-limited aggregates growing in a wedge. The significance of this angle is that it is the typical angular spread of a major finger. For wedges with angle larger than  $2\eta$ , two fingers can coexist. Thus a finger with this angular spread is a kind of building block for viscous fingering patterns and diffusion-limited aggregation clusters in radial geometry.

The diffusion limited aggregation (DLA) [1, 2] model is a simple idealization of a common natural process, the formation of natural objects where the rate-limiting step is diffusion. In the simplest examples (say, solidification from solution, or diffusion limited electrochemical deposition) particles random walk and then stick to a growing aggregate. Diffusion-limited growth of this type gives rise to remarkable morphologies which are ramified, disorderly, and, in the case of infinite diffusion length, fractal. It is this complexity which is the major interest in the model. Despite more than a decade of work in this field [2] very little theoretical understanding has been achieved. In this chapter we attempt to contribute to such understanding by demonstrating the existence of a kind of building block for the pattern: there seems to be a characteristic angular spread for the fingers which make up the structure.

## 5.1 Fingering instability

The fundamental origin of the complexity of DLA patterns has been known from the outset: it is in a *fingering instability*: diffusion-limited growth is generically linearly unstable for flat growing surfaces, and forms fingers. The proliferation of the fingers gives rise to the fractal pattern in a way which we seek to clarify here. Another physical system that displays the fingering instability is the displacement of an inviscid fluid by a viscous one, the viscous fingering problem. It has been suspected since the work of Paterson [3] that the large scale features of DLA patterns are similar to those in radial viscous fingering. They both obey the *Laplacian growth* equations:

$$\nabla^2 \phi = 0 \tag{5.1}$$

$$\hat{n} \cdot \nabla \phi = \hat{n} \cdot \vec{v} \tag{5.2}$$

Here  $\phi$  denotes the diffusing field, i.e. the probability density to ever find a random walker at point  $\mathbf{r}$  in the case of DLA or the pressure at  $\mathbf{r}$  in viscous fingering. The normal velocity of growth of the pattern is  $\hat{n} \cdot \vec{v}$ . The boundary value on the surface of the growing pattern,  $\phi_s$ , is given by the Gibbs-Thomson relation  $\phi_s = \gamma\kappa$  for the case of viscous fingering where  $\gamma$  is the surface tension. DLA differs by having the boundary condition set implicitly by the finite size of the accreting particles and by the fact that the patterns are affected by shot noise. Some authors have argued [4] that neither of these facts affect the large-scale features of the pattern, and that radial viscous fingering patterns are identical to DLA clusters in a coarse-grained sense. We adopt this point of view.

This idea is attractive because the theory of viscous fingering is quite well developed [5]. In particular, it is clear that viscous fingers in a channel geometry are not fractal [6], and attain a steady state of a single finger. The striking difference from the radial case, where there is no indication that a steady state is ever achieved, led Ben-Amar and collaborators [7] to investigate the wedge geometry. The general result is that in a wedge of any angle the selected finger grows in a self-similar way. For fixed surface tension they are stable for a finite time, and they then become unstable against tip-splitting. This idea was used by Sarkar [8] to give an estimate for the fractal dimension of DLA by counting the tip-splittings.

However, we think that Sarkar's estimate left out a crucial effect: that of finger competition. Our view is that this is the key to the whole problem: if fingers split in a wedge that is too narrow, they will compete, and one will die. The result will be a finger with sidebranches. On the other hand, if the wedge is wide enough, then the fingers will not compete, and there will be two branches to the pattern. The wedge angle,  $\alpha$  at which this begins to happen will be twice the typical angle

between fingers, which we call  $\eta$ . As a pattern grows the fingers will split until they form channels of angle  $\eta$  for their neighbors. There is some experimental support for this idea [9] in the mode of tip-splitting seen for various angles. However, the experimental evidence is ambiguous because the dynamic range of a real fingering experiment is limited. Here we will try to verify our ideas by giving an analytic estimate for  $\eta$ , and then show that these are reasonable by considering simulations of DLA clusters in a wedge.

## 5.2 Finger competition

To begin, consider two steady-state viscous fingers side by side in a wedge with periodic boundary conditions at the sides. We will attempt to estimate how large the angle must be so that there is no competition between them. For example, for  $\alpha = 2\pi$  the fingers grow independently.

We now look at the stability of the two finger solution in order to see if there is competition. We prepare one finger slightly longer than the other, and ask, in the linear regime, if there is a different growth rate for the two. We can see how the calculation goes by using the mapping, due to Ben-Amar and Brener, [10], between the wedge problem and the problem of diffusive (i.e. not Laplacian) growth in a channel. We first map the wedge to a strip using:  $\tilde{z} = [2/\alpha] \ln z$ . This transforms a wedge of angle  $\alpha$  centered around the  $x$ -axis in the  $z$  plane to a strip of width 2 in the  $\tilde{z}$  plane. Since the transformation is conformal, the field is Laplacian in the new variables. Eq. (2) becomes:

$$\hat{n} \cdot \tilde{\nabla} \phi = \exp(\alpha \tilde{x}) \hat{n} \cdot \vec{v}. \quad (5.3)$$

The Gibbs-Thomson condition on the interface is complicated in the new coordinates

except for small surface tension, in which case it becomes:

$$\phi_s = \gamma \tilde{\kappa} \exp(-\alpha \tilde{x}/2) \quad (5.4)$$

If we define  $\Phi \equiv \phi \exp(-\alpha \tilde{x})$  then  $\Phi$  satisfies, up to terms of order  $\alpha^2$ , a quasi-static diffusion equation in the frame moving with Peclet number  $\alpha$ :

$$\nabla^2 \Phi + 2\alpha \frac{d\Phi}{dx} = \alpha^2 \Phi \approx 0 \quad (5.5)$$

Eq. (5.3) now reads  $\hat{n} \cdot \tilde{\nabla} \Phi = \hat{n} \cdot \vec{v}$ . Thus we have two steady-state fingers growing in a channel with finite diffusion constant and with boundary condition on the interfaces  $\Phi_s = \gamma \tilde{\kappa} \exp(-3\alpha \tilde{x}/2)$ . This equation implies a space-dependent effective curvature. Thus our problem is not exactly the same as that of dendrites in a channel, but it is qualitatively the same<sup>1</sup>. For the question of competition, the exact form of the surface-tension is probably not important. From Eq. 5.5 it follows that  $1/\alpha$  plays the role of a diffusion length: the field is screened over distances larger than  $1/\alpha$  and two fingers that are separated by larger distance cannot compete. This is an indication that a critical angle exists.

We have verified this insight by a numerical stability analysis. We found that for small  $\alpha$  (weak screening) fingers compete, and for large wedge angle they do not. The numerical value for the threshold that we compute in this way ( $\alpha \approx 0.5$ ) is too large to be trusted because of the small  $\alpha$  approximation.

---

<sup>1</sup>We have made a further approximation here. In our stability analysis we use the steady state solution to the dendrite problem. For the wedge and for the channel there are two solutions for each surface tension corresponding to different finger widths. In the wedge, the solution with the smaller width is the stable one, and the opposite is true in the channel. However, for the question of finger competition, we think it does not matter which solution one looks at, since the two solutions differ only in their local tip structure. Finger competition is a more global question.

### 5.3 The two-needle model

In order to go further we do a different estimate which is more qualitative, but not restricted to small angles. Consider, again, two viscous fingers in a wedge of opening angle  $\alpha$ . We now replace the problem with a simpler one that we can solve analytically, that of two *needles* in the wedge. In complex notation, the tips of the needles are at  $z_1 = l_1 e^{i\alpha/4}$ ;  $z_2 = l_1 e^{3i\alpha/4}$ . The Laplacian field  $\phi$  vanishes on the needles, and we suppose that there is a cutoff (finite tip size)  $a$  and that the growth rate of the needles is given by the flux of the Laplacian field,  $\nabla\phi$  at the tips:  $z = z_i + ae^{i\theta_i} = z_i + \delta z_i$ ;  $\theta_{1,2} = \alpha/4, 3\alpha/4$ .

We solve by a series of conformal maps. First we map the  $z$  plane into the  $u$  plane with  $u = z^\beta$ ;  $\beta = 2\pi/\alpha$ . The two needles are now one needle along the imaginary axis. Now center the needle. Define  $L = [l_1^\beta + l_2^\beta]/2$ , and arrange things so that the needle goes from  $-L$  to  $L$  by putting  $w = u - [l_1^\beta - l_2^\beta]/2$ . Then we can map the line segment onto the unit circle by putting  $w = [Li/2][\tilde{z} + 1/\tilde{z}]$ . Now the two needles have been mapped onto points on the exterior of the unit circle ( $\tilde{z}_1 = 1, \tilde{z}_2 = -1$ ).

It is now clear that the potential can be written  $\phi = \text{Re}\psi$ ;  $\psi = \phi_o \ln(\tilde{z})$ , where  $\phi_o$  is proportional to the incoming flux. This potential satisfies periodic boundary conditions. To get the growth rate it is sufficient to find  $d\psi/dz$  because  $|d\psi/dz|^2 = |\nabla\phi|^2$ . By a straightforward computation we can write down the growth rate of tip  $i$ :

$$d\psi/dz|_i = |d\Phi/dz| \propto \frac{l_i^{\beta-1}}{[Ll_i^{\beta-1}a]^{1/2}} \propto \frac{l_i^{[\beta-1]/2}}{[l_1^\beta + l_2^\beta]^{1/2}}. \quad (5.6)$$

Whenever one finger is longer than the other, the longer one will get more flux, and, it seems, grow faster. However, we know from the computation above that there is a point at which fingers cease competing. Physically this is because the difference

between a needle and a finger is that a finger must grow in *area* if it is self-similar. Thus, even if the integrated flux to two fingers is the *same* the fatter one will grow more slowly since it will advance according to  $dA_i/dt \propto d(l_i^2)/dt \propto l_i dl_i/dt \propto G_i$  where  $G_i$  is the flux that finger  $i$  gets in competition with the other. We estimate  $G_i \propto l_i^{[\beta-1]/2}$  from the needle calculation. That is  $dl_i/dt \propto |d\Phi/dz|/l_i$ . Thus:

$$\frac{dl_1/dt}{dl_2/dt} = [l_1/l_2]^{[\beta-3]/2}. \quad (5.7)$$

When  $\beta = 3$ , that is, when  $\alpha = 120^\circ$ , the two fingers stop competing. Thus each finger occupies  $\eta = 60^\circ$ . We should note that this is exactly the criterion of Derrida and Hakim [11] who get it in a different way, namely by demanding that, for some fixed  $a$ , the *ratio* of the lengths of two spikes remain small (though the difference can be large). That is, they make the following quantity decrease, for  $l_1 > l_2$ :

$$\frac{d}{dt}(l_1/l_2) = \frac{l_1}{l_2} [(1/l_1)d\Phi_1/dz - (1/l_2)d\Phi_2/dz] \quad (5.8)$$

which is our estimate.

We can use this estimate in another way. Suppose that the fingers are fractal, so that we have  $A \propto l^D$  where  $D$  is the fractal dimension. Now repeating the calculation above, we must have  $(\beta - 1)/2 = D - 1$ , at the operating point. However, Turkevich and Scher [12] have given another criterion: if the cluster grows so that it has major branches, then the growth and the fractal dimension will be dominated by the tip angle. The result of this consideration, in our notation, amounts to saying that  $D = 1 + \pi/(\pi + \eta)$ . Using  $\beta = \pi/\eta$  we find that  $\eta$  satisfies a quadratic equation, whose solution is  $\eta = (\sqrt{2} - 1)\pi$  which corresponds to  $\eta \approx 75^\circ$ . Thus  $D = 1 + 1/\sqrt{2} = 1.71$  which is exactly the observed fractal dimension. This estimate was given by Ball [13] some years ago using a different argument.

## 5.4 Numerical simulations

To verify these estimates we turn to numerical calculations for DLA in a wedge. We grew a large number of off-lattice DLA clusters in wedges of different opening angles  $\alpha$ . For greater efficiency we used the method of hierarchical maps [14] adapted to the wedge geometry, so that our wedge was subdivided into sectors whose radii were in geometric ratios. The data which we will report involve averages over 25 realizations for each  $\alpha$ , and the number of particles,  $M$  in the wedge was determined so that  $M = 10^6 \alpha / 2\pi$ . That is, each wedge acted like a slice from a million-particle cluster. We report results for  $\alpha = 30^\circ, 60^\circ, 90^\circ, 120^\circ$ , and  $144^\circ$ .

We measured the fractal dimension of our clusters and find that it depends weakly, if at all, on  $\alpha$ . This allows us to understand the remarkable accuracy of the estimate of fractal dimension above. The Turkevich-Scher calculation implies that the fractal dimension of a finger would depend only on the tip velocity, which in turn depends on the tip structure. The invariance of the fractal dimension with  $\alpha$  indicates that the tip structure is not affected by boundaries, and thus probably not by the presence of other fingers. However, in the radial case, the large scale structure (the number of main surviving branches) adjusts via finger competition to be consistent with the local growth rate. In our estimate we gave a representation of the tip which is valid only far away – we replaced the cluster by a needle – but then used self-consistency to find the fractal dimension.

In this work our main interest is not the fractal dimension but the overall shape. To see this we computed the angular density-density correlation function,

$$c(\phi) = [\langle \rho(\theta + \phi)\rho(\theta) \rangle - \langle \rho \rangle^2]_{|\theta}. \quad (5.9)$$

Here  $\rho(\theta)$  is the density of particles in the cluster in a  $1^\circ$  sector around  $\theta$  and we

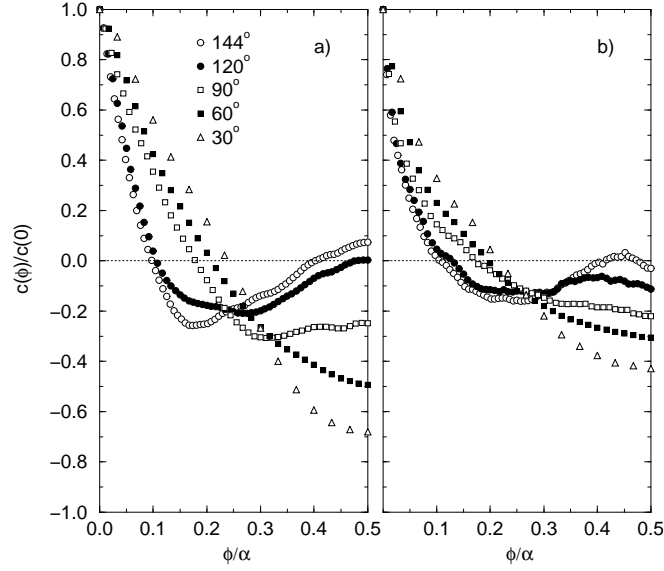


Figure 5.1: (a) Angular correlation function,  $c(\phi)/c(0)$ , for DLA clusters in a wedge of angle  $\alpha$  as a function of  $\phi/\alpha$ . (b) Correlation functions using the measure  $M_1$ .

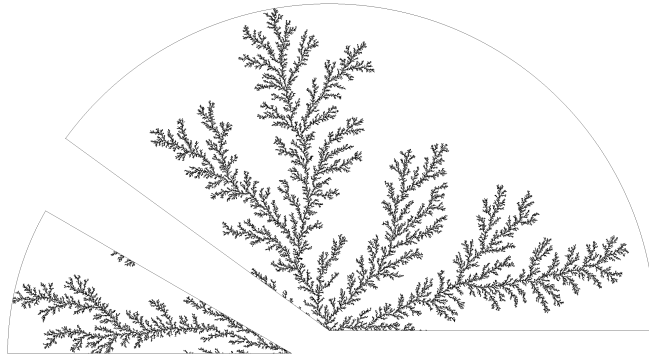


Figure 5.2: DLA clusters grown in wedges for  $\alpha = 30^\circ, 144^\circ$ .

average over the starting angle. All of the angles are taken as periodic with period  $\alpha$  so that the function is reflection-symmetric around  $\alpha/2$ . In Fig. 5.1(a) we show the correlation function averaged over 25 realizations, and in Fig. 5.2 a typical cluster for small and large angles.

There is a very clear difference between large and small  $\alpha$  in the behavior of  $c(\phi)$ . For small angles there is an anticorrelation between the origin and other angles. This corresponds to the matter being clustered in one branch. For  $\alpha$  between  $90^\circ$  and  $144^\circ$

the nature of the correlations changes. The appearance of a second peak and the positive correlation function indicates that there are now two coexisting branches [15].

We have examined the individual realizations that make up the average. The appearance of the second peak corresponds to structures which sometimes have one, and sometimes two (or more) large branches. In the case of  $120^\circ$  and  $144^\circ$  there is considerable fluctuation in the correlation functions (and the visual appearance) of each individual realization. This is a further indication that for some  $\alpha$  in this range there is a critical point.

We have seen no indication that the correlation functions depend on the cluster size. For the case of  $30^\circ$  we grew clusters ten times larger than those described above to check this, with the result that the correlations were the same. The correlation function depends on the angular spread of the wedge, not on the space available to spread out, which indicates that the branches are self-similar in shape. If we take the point at which the  $c(\alpha/2)$  crosses 0 as the criterion for determining  $\eta$  we find that the typical distance between different major branches is  $\eta = \alpha/2 \approx 60 - 70^\circ$ . This is in rough agreement with our analytic estimates, and we take this as a verification of our basic idea.

We made another check by trying to quantify exactly what we mean by a 'major branch'. We focus on the idea that for asymptotic behavior the most important feature is that some branches die, and some survive competition. To see this quantitatively we introduce a measure on DLA clusters which we call the *descendent measure*,  $M_x$ . For this quantity we weight each point according to the number of descendents it has in the last fraction  $x$  of the growth. Thus  $M_1$  measures the total number of points that grow from a given one, and, say,  $M_{0.01}$  the number of descen-

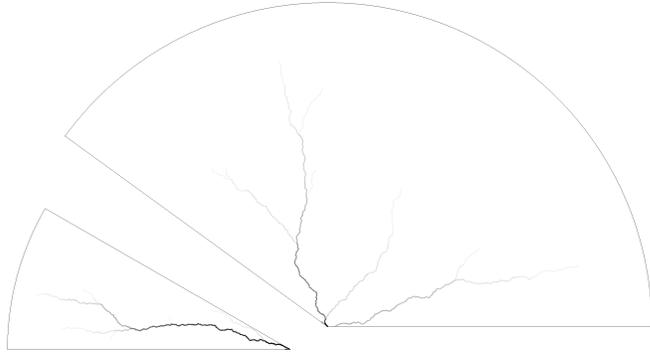


Figure 5.3: DLA clusters plotted with gray level proportional to  $M_1$  for  $\alpha = 30^\circ, 144^\circ$

dent points in a tiny active zone on the outside of the cluster. The appearance of major branches derived this way is quite robust, and doesn't depend much on  $x$ . Clusters with  $M_1$  weighting are shown in Fig. 5.3, and Fig. 5.1(b) illustrates that the correlation functions near the critical angle are not much different with the  $M_x$  weighting. The critical angle is robust, but for small angles the measure clearly localizes the main branch much more cleanly than the measure that uniformly weights the mass since it prunes sidebranches. The  $M_x$  weighting could be interesting in other contexts since it provides a definition of a backbone for DLA.

Some aspects of the idea that we have proposed here have appeared in other forms previously. For example, Arneodo and collaborators have observed some hints of a 5-fold structure in DLA [16]. This is more or less what we find since our angle  $\eta$  is close to  $2\pi/5$ . Many workers have noted that DLA clusters seem to have 5 major arms, but this qualitative impression was not supported by a quantitative estimate of the type we have given here.

We think that we should follow up our idea by checking it for radial viscous fingering in direct simulations. We hope that sophisticated methods such as the vortex sheet technique [17] could allow us to do this, though this is a computation intensive approach. The effect of the exact form of the surface tension can also be

checked, although in our opinion the role of the surface tension is only to regularize the equations; its exact form (e.g. the finite size of the DLA particles acts as an effective surface tension) is unimportant. Ideally we should also try to put this idea of a structure made up of building blocks with some typical angle into a more general theoretical context. However, we do not see any obvious relationship between what we have done and the other theoretical approaches to Laplacian growth [18].

LMS and ES are supported by DOE grant DEFG-02-95ER-45546. LMS would like to thank the Weizmann Institute of Science for hospitality and the CIES for support by a Fulbright grant. IP acknowledges partial support from the Basic Research fund administered by the Israel Academy of Sciences and Humanities. DAK acknowledges support from the Israel Science Foundation.

## References

- [1] T. A. Witten and L. M. Sander, Phys. Rev. Lett. **47**, 1400 (1981); T. A. Witten and L. M. Sander, Phys. Rev. B **27**, 2586 (1983).
- [2] T. Vicsek, *Fractal Growth Phenomena* (World Scientific, Singapore, 1992).
- [3] L. Paterson, Phys. Rev. Lett. **52**, 1621 (1985).
- [4] L. Sander, P. Ramanlal, and E. Ben-Jacob, Phys. Rev. **A32**, 3160 (1985).
- [5] P. Pelce (ed.), *Dynamics of Curved Fronts*, (Academic Press, Boston, 1988).
- [6] H. Thome, M. Rabaud, V. Hakim, and Y. Couder, Physics of Fluids A **1**, 224 (1989).
- [7] M. Ben Amar, Phys. Rev. A **43**, 5724 (1991); **44** 3673 (1991).
- [8] S. K. Sarkar, Phys. Rev. Lett., **65**, 2680 (1990).
- [9] M. Ben-Amar, V. Hakim, M. Mashaal, and Y. Couder, Physics of Fluids A **3**, 1687 (1991).
- [10] M. Ben-Amar and E. Brener, Phys. Rev. Lett. **75**, 561 (1995), Physica D **98**, 128 (1996).
- [11] B. Derrida and V. Hakim, Phys. Rev. A **45**, 8759 (1992).
- [12] L. Turkevich and H. Scher, Phys. Rev. Lett. **55**, 1026 (1985).
- [13] R. C. Ball, Physica A **140**, 62 (1986).
- [14] R. C. Ball and R. M. Brady, J. Phys. A **18**, L809 (1985).
- [15] Similar indication of coexisting branches has been found in density profiles of DLA clusters grown in wedges with reflective walls, A. Arneodo, J. Elezgaray, M. Tabard, and F. Tallet, Phys. Rev. E **53**, 6200 (1996).
- [16] A. Arneodo, F. Argoul, E. Bacry, J-F. Muzy, and M. Tabard, Phys. Rev. Lett. **68**, 3456 (1992).
- [17] T. Hou, J. Lowengrub, and M. Shelley, J. Comp. Phys. **114**, 312 (1994).
- [18] L. Pietronero, A. Erzan, and C. Evertsz, Phys. Rev. Lett. **61**, 861 (1988); T. Halsey, Phys. Rev. Lett. **72**, 1228 (1994).

## CHAPTER 6

# Diffusion-limited aggregation and iterated conformal maps

The research presented in this chapter was done with Benny Davidovitch, H.G.E Hentschel, Zeev Olami, Itamar Procaccia, and Leonard M. Sander; most of the numerical work was done by me, while the analytical work was shared between the collaborators. It was published in *Phys. Rev. E* **59**, 1368 (1999).

The creation of fractal clusters by diffusion limited aggregation (DLA) is studied by using iterated stochastic conformal maps following the method proposed recently by Hastings and Levitov. The object of interest is the function  $\Phi^{(n)}$  which conformally maps the exterior of the unit circle to the exterior of an  $n$ -particle DLA. The map  $\Phi^{(n)}$  is obtained from  $n$  stochastic iterations of a function  $\phi$  that maps the unit circle to the unit circle with a bump. The scaling properties usually studied in the literature on DLA appear in a new light using this language. The dimension of the cluster is determined by the linear coefficient in the Laurent expansion of  $\Phi^{(n)}$ , which asymptotically becomes a deterministic function of  $n$ . We find new relationships between the generalized dimensions of the harmonic measure and the scaling behavior of the Laurent coefficients.

## 6.1 Introduction

The diffusion limited aggregation (DLA) model was introduced in 1981 by T. Witten and L. Sander [1]. The model has been shown to underlie many pattern forming processes including dielectric breakdown [2], two-fluid flow [3], and electrochemical deposition [4]. The model begins with fixing one particle at the center of coordinates in  $d$ -dimensions, and follows the creation of a cluster by releasing random walkers from infinity, allowing them to walk around until they hit any particle belonging to the cluster. Upon hitting they are attached to the growing cluster. The model was studied on- and off- lattice in several dimensions  $d \geq 2$ ; here we are only interested in the off-lattice versions in two dimensions.

DLA has attracted enormous interest over the years since it is a remarkable example of the spontaneous creation of fractal objects. It is believed that asymptotically (when the number of particles  $n \rightarrow \infty$ ) the dimension  $D$  of the cluster is very close to 1.71 [5], although there exists to date no proof for this fact in spite of several interesting attempts [6, 7]. In addition, the model has attracted interest since it was among the first [8] to offer a true multifractal measure: the harmonic measure (which determines the probability that a random walker from infinity will hit a point at the boundary) exhibits singularities that are usefully described using the multifractal formalism [9]. Nevertheless DLA still poses more unsolved problems than answers. It is obvious that a new language is needed in order to allow fresh attempts to explain the growth patterns, the fractal dimension, and the multifractal properties of the harmonic measure.

Such a new language was proposed recently by Hastings and Levitov [10, 11]. These authors showed that DLA in two dimensions can be grown by iterating stochas-

tic conformal maps. We adopt their basic strategy and will see that it provides a new formulation of the problem which may lead to new insights and results.

The basic idea is to follow the evolution of the conformal mapping  $\Phi^{(n)}(w)$  which maps the exterior of the unit circle in the mathematical  $w$ -plane onto the complement of the cluster of  $n$  particles in the physical  $z$ -plane.  $\Phi^{(n)}$  is unique by the Riemann mapping theorem, provided that it satisfies the boundary condition

$$\Phi^{(n)}(w) \sim F_1^{(n)} w \quad \text{as } w \rightarrow \infty. \quad (6.1)$$

Here  $F_1^{(n)}$  is a real positive coefficient, fixing the argument of  $[\Phi^{(n)}(w)]'$  to be zero at infinity.  $\Phi^{(n)}(w)$  is related to the complex electric potential  $\Psi^{(n)}(z)$  by

$$\Psi^{(n)}(z) = \ln h^{(n)}(z), \quad (6.2)$$

where  $h^{(n)}(z) = [\Phi^{(n)}]^{-1}(z)$  is the inverse mapping. Letting  $z \rightarrow \infty$  in Eq.(6.1) it is easy to verify that Eq.(6.2) implies

$$\Psi^{(n)}(z) \sim \ln z \quad \text{when } z \rightarrow \infty \quad (6.3)$$

as it should be at  $d = 2$ .

The equation of motion for  $\Phi^{(n)}(w)$  is determined recursively. The choice of the initial map  $\Phi^{(0)}(w)$  is rather flexible, and in this chapter we select (arbitrarily) an initial condition  $\Phi^{(0)}(w) = w$ . We expect the asymptotic cluster to be independent of this choice. Then suppose that  $\Phi^{(n-1)}(w)$  is given. The cluster of  $n$  ‘‘particles’’ is created by adding a new ‘‘particle’’ of constant shape and linear scale  $\sqrt{\lambda_0}$  to the cluster of  $(n - 1)$  ‘‘particles’’ at a position which is chosen randomly according to the harmonic measure. We denote points on the boundary of the cluster by  $Z(s)$  where  $s$  is an arc-length parametrization. The probability to add a particle on an infinitesimal arc  $ds$  centered at the point  $z(s)$  on the cluster boundary is

$$P(s, ds) \sim |\nabla \Psi(s)| ds. \quad (6.4)$$

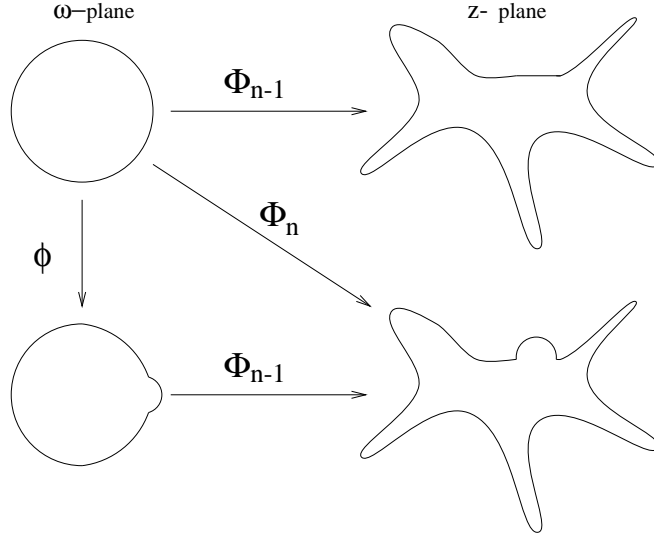


Figure 6.1: Diagrammatic representation of the mappings  $\Phi$  and  $\phi$ .

The pre-image of  $z(s)$  and  $ds$  in the  $w$ -plane are  $e^{i\theta}$  and  $d\theta$  respectively. Clearly,  $ds = |[\Phi^{(n-1)}]'(e^{i\theta})|d\theta$ . From Eq.(6.2) we conclude that

$$P(s, ds) \sim |\nabla\Psi(s)||\Phi'|d\theta = d\theta, \quad (6.5)$$

so the harmonic measure on the real cluster translates to a uniform measure on the unit circle in the mathematical plane.

The image of the cluster of  $n$  particles under  $h^{(n)}(z)$  is, by definition, just the unit circle. On the other hand, the image of the cluster of  $n$  particles under  $h^{(n-1)}(z)$  is the unit circle with a small bump whose linear scale is  $\sqrt{\lambda_0}/|\Phi'^{(n-1)}(e^{i\theta_n})|$  where  $e^{i\theta_n}$  is the image (under  $h^{(n-1)}$ ) of the point  $z_n$  on the real cluster at which the growth occurred.

Let us define now a new function  $\phi_{\lambda_n, \theta_n}(w)$ . This function maps the unit circle to the unit circle with a bump of linear scale  $\sqrt{\lambda_n}$  around the point  $e^{i\theta_n}$ . For  $w \rightarrow \infty$ ,  $\phi_{\lambda_n, \theta_n}(w) \sim w$  (with positive real proportionality coefficient). Using  $\phi_{\lambda_n, \theta_n}(w)$  the recursion relation for  $\Phi^{(n)}(w)$  is given by (see Fig. 6.1):

$$\Phi^{(n)}(w) = \Phi^{(n-1)}(\phi_{\lambda_n, \theta_n}(w)). \quad (6.6)$$

According to the above discussion  $\lambda_n$  is given by

$$\lambda_n = \frac{\lambda_0}{|\Phi^{(n-1)'}(e^{i\theta_n})|^2} \quad (6.7)$$

so the RHS of Eq.(6.6) is determined completely by  $\Phi^{(n-1)}(w)$ ; Eq.(6.6) induces the recursive dynamics of  $\Phi^{(n)}(w)$ .

The recursive dynamics can be represented as iterations of the map  $\phi_{\lambda_n, \theta_n}(w)$ ,

$$\Phi^{(n)}(w) = \phi_{\lambda_1, \theta_1} \circ \phi_{\lambda_2, \theta_2} \circ \dots \circ \phi_{\lambda_n, \theta_n}(w). \quad (6.8)$$

This composition appears as a standard iteration of stochastic maps. This is not so. The order of iterations is inverted – the last point of the trajectory is the inner argument in this iteration. As a result the transition from  $\Phi^{(n)}(w)$  to  $\Phi^{(n+1)}(w)$  is not achieved by one additional iteration, but by composing the  $n$  former maps Eq.(6.8) starting from a different seed which is no longer  $\omega$  but  $\phi_{\lambda_{n+1}, \theta_{n+1}}(w)$ .

We note that in the physical plane the “particles” are roughly of the same size. To achieve this the linear scales  $\sqrt{\lambda_n}$  vary widely as a function of  $n$  and  $\theta$ . We will see that the distribution of  $\sqrt{\lambda_n}$  and their correlations for different values of  $n$  determine many of the scaling properties of the resulting cluster. In particular their moments are related to the generalized dimensions of the harmonic measure.

There are many functions  $\phi_{\lambda, \theta}$  which conformally map the unit circle to the unit circle with a bump. A simple choice is a function which behaves linearly for large  $w$  and has a simple pole inside the unit circle which will induce a bump in the image. The pole has to be at  $w_0 = 1 - \lambda$  in order to localize the bump near  $w = 1$  and make it of linear size of the order  $\sqrt{\lambda}$ . The residue has to be  $\lambda^{3/2}$ , in order for the bump’s height to be also of the order  $\sqrt{\lambda}$ . Consider then

$$\phi(w) = (1 + \lambda)w + \frac{\lambda^{3/2}}{w - w_0}.$$

Careful thinking leads to the conclusion that this function and other similar functions are inappropriate: they have long “tails”. In other words, the unit circle is slightly distorted everywhere. This small global distortion may result in a loss of conformality or in the growth of non-constant size particles in the physical plane in numerical applications.

It was proposed in Ref. [10] that a choice for  $\phi_{\lambda_n, \theta_n}(w)$  that is free of global distortion is given by

$$\begin{aligned} \phi_{\lambda,0}(w) &= w^{1-a} \left\{ \frac{(1+\lambda)}{2w} (1+w) \right. \\ &\times \left. \left[ 1 + w + w \left( 1 + \frac{1}{w^2} - \frac{2}{w} \frac{1-\lambda}{1+\lambda} \right)^{1/2} \right] - 1 \right\}^a \end{aligned} \quad (6.9)$$

$$\phi_{\lambda,\theta}(w) = e^{i\theta} \phi_{\lambda,0}(e^{-i\theta} w), \quad (6.10)$$

The parameter  $a$  is confined in the range  $0 < a < 1$ . As  $a$  decreases the bump becomes flatter, with the identity map obtained for  $a = 0$ . As  $a$  increases towards unity the bump becomes elongated normally to the unit circle, with a limit of becoming a line (“strike” in the language of [10]) when  $a = 1$ . Naively one might think that the shape of the individual particle is irrelevant for the large scale fractal statistics; we will see that this is not the case. The dependence on  $a$  is important and needs to be taken into account. Notice that this map has two branch points on the unit circle. The advantage of this is that the bump is strongly localized. On the other hand repeated iterations of this map leads to rather complex analytic structure.

The aim of this chapter is therefore to investigate the scaling and statistical properties of such iterated stochastic conformal maps with a view to discovering the scaling properties induced by the dynamics which any analytic theory must ultimately explain. In Section II we present the numerical procedure used to generate the fractal clusters, and in Section III give the necessary mathematical background

to describe such mappings. In particular we discuss the Laurent expansion of the conformal map from the unit circle to the  $n$ -particle cluster; the coefficients of the Laurent series have interesting scaling behaviour with the size of the cluster which is intimately related to the fractal dimension of the cluster and to the generalized dimensions of the harmonic measure. In Section IV we present numerical results regarding the scaling properties of averages of the Laurent coefficients and of the size parameter  $\lambda_n$ . The results are accompanied by a theoretical analysis and interpretation. In Section V we conclude with some remarks on the road ahead.

## 6.2 Numerical procedure

The algorithm simulating the growth of the cluster is based on Ref. [10]. The  $n$  “particle” cluster is encoded by the series of pairs  $\{(\theta_i, \lambda_i)\}_{i=1}^n$ . Having the first  $n-1$  pairs, the  $n^{\text{th}}$  pair is found as follows: choose  $\theta_n$  from a uniform distribution in  $[0, 2\pi]$ , independent of previous history. Then compute  $\lambda_n$  from Eq.(6.7), where the derivative of the iterated function  $\Phi^{(n-1)}$  involves  $\phi'_{\lambda_{n-1}, \theta_{n-1}}, \phi'_{\lambda_{n-2}, \theta_{n-2}}, \phi'_{\lambda_{n-3}, \theta_{n-3}}$  etc, computed respectively at the points  $e^{i\theta_n}, \phi_{\lambda_{n-1}, \theta_{n-1}}(e^{i\theta_n}), \phi_{\lambda_{n-2}, \theta_{n-2}}(\phi_{\lambda_{n-1}, \theta_{n-1}}(e^{i\theta_n}))$ , etc. Notice that the evaluation of both  $\phi'$  and  $\phi$  after the addition of one particle involves  $O(n)$  operations since the seed changes at every  $n$ . This translates into  $n^2$  time complexity for the growth of an  $n$ -particle cluster. This is inferior to the best algorithms to grow DLA (using hierarchical maps [12], with close to linear efficiency), but the present algorithm is not aimed at efficiency. Rather, it is used since the Laplacian field and the growth probability which is derived from it are readily available at every point of the cluster and away from it. The typical time to grow a 10,000 particle cluster is 8 minutes on a 300 MHz Pentium-II.

Naively one would expect that any choice of  $0 < a < 1$  would yield DLA clusters,

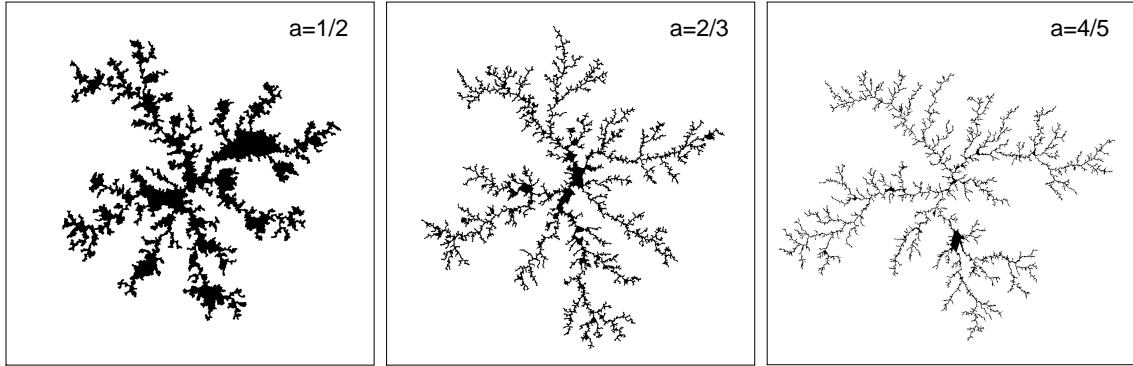


Figure 6.2: Typical clusters of 10,000 particles. The black regions represent the interiors of the images of the unit circle under the map  $\Phi^{(10,000)}$  for three values of  $a$ . The large enclosed areas for the  $a = 1/2$  cluster are the unwanted “fill-up” events discussed in Section II. However, the black area in the  $a = 4/5$  cluster is only a numerical artifact: that region is not resolved by double precision arithmetic.

since  $a$  only determines the shape of the particles (the aspect ratio is  $\frac{1}{2}a/(1-a)$  for small  $\lambda$ ), and the microscopic details of the particles (except their linear size) should not affect the global properties. Three typical clusters with particles of various aspect ratios  $a$  are shown in Fig. 6.2.

We mark in black the interior of the image of the unit circle under the conformal map  $\Phi^{(n)}(w)$ . The objects look very much like typical DLA clusters grown by standard off-lattice techniques, and in the next section we demonstrate that they have fractal dimensions in close agreement with the latter. For  $a$  significantly different from  $2/3$ , disadvantages of the algorithm get amplified. Since the functional form of  $\phi$  is fixed (only the size and position of the “bump” change), particles of constant shape and size are obtained only if the magnification factor  $|\Phi^{(n-1)}|$  (the inverse of the field) is approximately constant in the  $w$ -plane around the “bump” of  $\phi$ . If the particles are elongated along the cluster, then the variation of the field along the cluster affects the shape: large otherwise deeply invaginated regions, where  $\Phi'$

is large, are filled up with a single particle, and the resulting cluster tends to be more compact. This effect, slightly noticeable even at  $a = 2/3$ , is quite significant at the otherwise natural choice of  $a = 1/2$ , where the particles are half circles. In Fig. 6.2 we show such a cluster and point out to the area filling dark regions which represent such unwanted events. The other extreme, when the particles stick out of the cluster, leads to sensitivity to variations in the field going *away* from the cluster. Especially if a bump is grown on a tip of a branch, where the field decreases rapidly as one goes away from the tip (such that  $\Phi'$  increases significantly), then the map of the bump gets magnified, resulting in particles of very unequal sizes.

It is necessary to stress that even for  $a = 2/3$ , when this procedure appears to yield nice ramified structures, the problem of fill-ups does not go away: in a few rare cases the particle – if it happens to land on a place where  $|\Phi''|$  is large – is significantly distorted. The net effect is that large areas surrounded by the cluster (where the growth probability is small) are filled up entirely by one distorted particle. For the value of  $a = 1/2$  it appeared that the errors may be unbounded. Our numerics indicates that for  $a = 2/3$  the errors were bounded for the cluster sizes that we considered. We do not have a mathematical proof of boundedness of the errors, and our disregard of this danger is only based on the sensible appearance of our clusters at this value of  $a$ .

### 6.3 Mathematical Background

In this section we discuss the Laurent expansion of our conformal maps, and introduce the statistical objects that are studied numerically in the next section.

### 6.3.1 Laurent Expansion

Since the functions  $\Phi^{(n)}(w)$  and  $\phi_{\lambda,\theta}(w)$  are required to be linear in  $w$  at infinity, they can be expanded in a Laurent series in which the highest power is  $w$ :

$$\Phi^{(n)}(w) = F_1^{(n)}w + F_0^{(n)} + F_{-1}^{(n)}w^{-1} + F_{-2}^{(n)}w^{-2} + \dots \quad (6.11)$$

$$\phi_{\lambda,\theta}(w) = f_1w + f_0 + f_{-1}w^{-1} + f_{-2}w^{-2} + \dots \quad (6.12)$$

where

$$\begin{aligned} f_1 &= (1 + \lambda)^a \\ f_0 &= \frac{2a\lambda e^{i\theta}}{(1 + \lambda)^{1-a}} \\ f_{-1} &= \frac{2a\lambda e^{2i\theta}}{(1 + \lambda)^{2-a}} \left(1 + \frac{2a-1}{2}\lambda\right) \\ f_{-2} &= \frac{2a\lambda e^{3i\theta}}{(1 + \lambda)^{3-a}} \left(1 + 2(a-1)\lambda + \frac{2a^2 - 3a + 1}{3}\lambda^2\right) \end{aligned}$$

The recursion equations for the Laurent coefficients of  $\Phi^{(n)}(w)$  can be obtained by substituting the series of  $\Phi$  and  $\phi$  into the recursion formula (6.6). We find

$$F_1^{(n)} = F_1^{(n-1)} f_1^{(n)} \quad (6.13)$$

$$F_0^{(n)} = F_1^{(n-1)} f_0^{(n)} + F_0^{(n-1)}$$

$$F_{-1}^{(n)} = F_1^{(n-1)} f_{-1}^{(n)} + F_{-1}^{(n-1)} / f_1^{(n)}$$

$$F_{-2}^{(n)} = F_1^{(n-1)} f_{-2}^{(n)} - F_{-1}^{(n-1)} \frac{f_0^{(n)}}{(f_1^{(n)})^2} + F_{-2}^{(n-1)} \frac{1}{(f_1^{(n)})^2} \quad (6.14)$$

...

We note that the  $n$ -dependence of  $f_i^{(n)}$  follows from the dependence on the randomly chosen  $\theta_n$  at the  $n$ th step, from which follows the dependence of  $\lambda_n$  on  $n$ . The latter is however a function of all the previous growth steps, making the iteration (6.13)-(6.14) rather difficult to analyze.

A general relation between the Laurent coefficients is furnished by the so-called area theorem which applies to univalent mappings. Since our maps solve the Laplace equations with boundary conditions only at infinity and on the cluster boundary where the potential is zero, they map the  $w$  plane uniquely (and with a unique inverse) to the  $z$  plane. In other words, the pressure lines and the stream lines are non-degenerate. Such mappings have the property [13] that the area of the image of the unit disc in the  $n$ th step is given by:

$$S_n = |F_1^{(n)}|^2 - \sum_{k=1}^{\infty} k |F_{-k}^{(n)}|^2 \quad (6.15)$$

A second theorem that will be useful in our thinking is a consequence of the so-called one-fourth theorem, see Appendix A. There a statement is proven that the interior of the curve  $\{z : z = \Phi^{(n)}(e^{i\theta})\}$  is contained in the  $z$ -plane by a circle of radius  $4F_1^{(n)}$ . Now as the area  $S_n$  is obtained simply from the superposition of  $n$  bumps of roughly the same area  $\lambda_0$ , it has to scale like  $S_n \approx n\lambda_0$ , for large  $n$ . On the other hand any typical radius of the cluster should scale like  $n^{1/D}\sqrt{\lambda_0}$  where  $D$  is the dimension of the cluster. We can thus expect a scaling of  $F_1^{(n)}$  that goes like

$$F_1^{(n)} \sim n^{1/D}\sqrt{\lambda_0} \quad (6.16)$$

. We note in passing that this scaling law offers us a very convenient way to measure the fractal dimension of the growing cluster. Indeed, we measured the dimension  $D$  for a range of  $a$  in this way by averaging  $F_1^{(n)}$  over 100 clusters. We found that for a range of  $a$  spanning the interval  $[1/3, 8/9]$  the dimension is constant, around 1.7.

We can infer therefore that the sum in Eq. (6.15) which subtracts positive contributions from  $|F_1^{(n)}|^2$  contains terms that cancel the behavior of  $n^{2/D}$  (remember that  $D < 2$ ), leaving a power of unity for the scaling of  $S_n$ . Indeed, we will show

below both numerical and theoretical evidence for the scaling behavior of the  $|F_{-k}^{(n)}|^2$  for  $k > 6$  which is in agreement with  $n^{2/D}$ .

We can give a direct physical interpretation for the coefficients  $F_k^{(n)}$  by comparing them to the coefficients of the series for  $\Psi^{(n)}$ , cf. Eq.(6.2):

$$\Psi^{(n)}(z) = \ln(z) - \ln(r_0) + \sum_1^{\infty} \frac{\psi_k}{z^k} \quad (6.17)$$

The coefficient of  $\ln(z)$  is unity so that the electric flux is unity. This corresponds to the normalization of the probability. The constant  $r_0$  is the Laplace radius which is the radius of a charged disk which would give the same field far away. The rest of the  $\phi_k$ 's are conventional multipole moments.

The relations between the Laurent coefficients of  $\Psi^{(n)}$  and  $\Phi^{(n)}$  are:

$$\begin{aligned} r_0 &= F_1 \\ \psi_1 &= -F_0 \\ \psi_2 &= -F_{-1}F_1 - \frac{1}{2}F_0^2 \\ \psi_3 &= -F_{-2}F_1^2 - 2F_0F_{-1}F_1 - \frac{1}{3}F_0^3 \\ \psi_4 &= -F_{-3}F_1^3 - \frac{3}{2}F_{-1}^2F_1^2 - 3F_1F_0^2F_{-1} \\ &\quad - 3F_{-2}F_0F_1^2 - \frac{1}{4}F_0^4 \end{aligned} \quad (6.18)$$

The first line shows that  $F_1 = r_0$ , the Laplace radius, in accordance with the one-fourth theorem.

The second line shows that the dipole moment  $\psi_1$  is  $-F_0$ . We can interpret this coefficient as a distance, the wandering of the center of charge due to the random addition of the particles. We will take the point of view that this quantity is less “intrinsic” than the others to the dynamics of the DLA growth. In fact, if we set  $F_0 = \psi_1 = 0$ , (we could imagine shifting the cluster as we grow it) we can rewrite

the rest of the equations:

$$\begin{aligned}
-F_{-1} &\sim \psi_2/r_0 \\
-F_{-2} &\sim \psi_3/r_0^2 \\
-F_{-3} &\sim (\psi_4 + \frac{3}{2}\psi_2^2)/r_0^3,
\end{aligned} \tag{6.19}$$

etc. This leads to the interpretation of  $F_{-k}$  in terms of the multipole expansion of the electric field.

### 6.3.2 Statistical objects and the relations to generalized dimensions

Our growth process is stochastic. Accordingly, it is natural to introduce averages over the randomness. In our thinking there are two important averages, one over histories of the whole random trajectory  $\{\theta_i\}_{i=1}^n$ , and the other only over the random choice of  $\theta_n$  at the  $n$ th step. To distinguish between the two we denote the first by angular brackets and refer to it as “history-average”, while the second is denoted by an overbar and referred to as a “cluster-average”. There is a possibility that for very large clusters ( $n \rightarrow \infty$ ) the two averages result in the same numbers. We will refer to such a property as “self-averaging”.

The cluster average of moments of  $\lambda_n$  offers a relationship to the generalized dimensions of the harmonic measure [14]. The latter are defined by dividing the plane into boxes of size  $\epsilon$ , and estimating the probability for a random walker to hit the piece of the boundary of the cluster which is included in the  $i$ th box by

$$p_i(\epsilon) = |E_i|\epsilon, \tag{6.20}$$

where  $|E_i|$  is the modulus of the electric field  $|\nabla\Psi_i|$  at some point in the  $i$ th box.

The generalized dimensions are defined by the relation

$$\sum_{i=1}^{N(\epsilon)} p_i^q(\epsilon) \sim \left(\frac{\epsilon}{R}\right)^{(q-1)D_q} \tag{6.21}$$

where  $N(\epsilon)$  is the number of boxes of size  $\epsilon$  that are needed to cover the boundary, and  $R$  is the linear size of the largest possible box, which is of the order of the radius of the cluster. Substituting (6.20) we find

$$\epsilon^{q-1} \sum_{i=1}^{N(\epsilon)} |E_i|^q \epsilon \sim \left(\frac{\epsilon}{R}\right)^{(q-1)D_q} \quad (6.22)$$

Taking  $\epsilon$  very small, of the order of  $\sqrt{\lambda_0}$ , and assuming that the field is smooth on this scale we have:

$$\int_0^L |E_i|^q ds \sim (\sqrt{\lambda_0})^{1-q} n^{(1-q)D_q/D} \quad (6.23)$$

where  $L$  is the length of the boundary,  $ds$  is an arc-length differential, and we have used the scaling law  $n \sim S_n/\epsilon^2 \sim (R/\epsilon)^{1/D}$ .

The connection to our language is obtained by considering the cluster average of powers of  $\lambda_n$ . We grow a cluster of  $n-1$  particles, perform repeated random choices of growth sites (without growing), and compute  $\lambda_n$  for each choice. The cluster average can be represented as an integral over the unit circle,  $\overline{\lambda_n^q}$ , and is given by

$$\overline{\lambda_n^q} \equiv (1/2\pi) \int_0^{2\pi} \lambda_n^q(\theta) d\theta . \quad (6.24)$$

Recalling Eq. (6.7) we observe that  $\lambda_n^q(\theta) = \lambda_0^q |E(\theta)|^{2q}$ . The last relation, Eq.(6.5), and Eq.(6.23) imply the scaling relation

$$\overline{\lambda_n^q} \sim n^{-2qD_{2q+1}/D} . \quad (6.25)$$

## 6.4 Numerical results and their interpretation

In this section we present results on three topics:

- (i) The coefficients of the Laurent expansion. The scaling behaviour of these quantities is described and discussed in the first subsection.
- (ii) The microscopic fluctuations in the conformal map. We show that the assumption of self-averaging is valid for Eq.(6.25) and that the multi-fractal exponents are

in a good agreement with the known ones.

(iii) Distribution functions of the Laurent coefficients. We analyze numerically the width of those functions and find that  $F_1^{(n)}$  tends to a deterministic function of  $n$ . We attribute this effect to non-trivial temporal correlations in the field, and give some evidence of their existence.

#### 6.4.1 Laurent Coefficients of $\Phi^{(n)}$

All the coefficients of the Laurent series of  $\Phi^{(n)}(w)$  are complex numbers except  $F_1$  which is real by the choice of zero phase at infinity, see Eq.(6.1). Most of our discussion below pertains to the amplitudes of the coefficients  $F_k$ . We need to stress, however, that the phases are not irrelevant. If we attempted to use the correct amplitudes with random phases, the resulting series will in general not be conformal.

One of the main results of this chapter is that in addition to the expected scaling behavior of the linear coefficient  $F_1^{(n)}$  (given in Eq. (6.16) the rest of the amplitudes of the Laurent coefficients  $|F_{-k}^{(n)}|$  exhibit also a scaling behavior. We find numerically that in the mean the magnitudes of the Laurent coefficients scale as powers of  $n$ :

$$\langle |F_k^{(n)}|^2 \rangle = a_k n^{x_k}. \quad (6.26)$$

The exponents  $x_k$  are given in Fig. 6.3. We first discuss the consequences of the scaling behavior of  $F_1^{(n)}$ .

#### Scaling of $F_1$

The scaling behavior (6.16) has immediate consequences for the scaling behavior of the bump areas  $\lambda_n$  that are the subject of the next subsection. The connection appears from the recursion Eq.(6.13) of  $F_1^{(n)}$  which together with  $f_1 = (1 + \lambda)^a$  reads

$$F_1^{(n)} = \prod_{k=1}^n [1 + \lambda_k]^a. \quad (6.27)$$

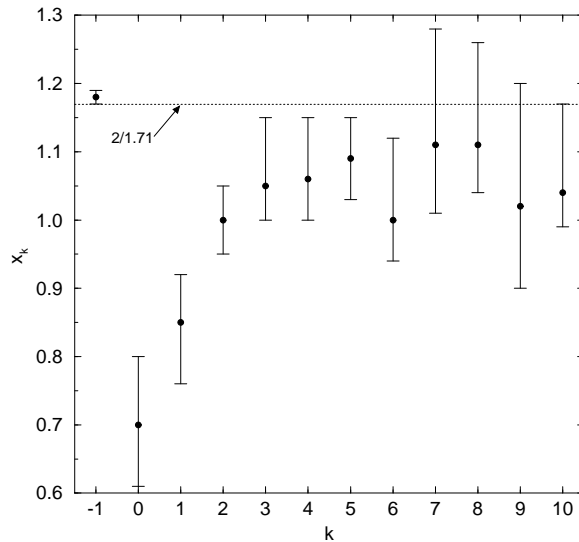


Figure 6.3: The scaling exponents of the Laurent coefficients:  $\langle |F_{-k}|^2 \rangle \sim n^{x_k}$ . The values are obtained by averaging 400 independent realizations of 10,000 particle clusters.

Taking history averages we find

$$\langle F_1^{(n)} \rangle = \left\langle \prod_{k=1}^n [1 + \lambda_k]^a \right\rangle \quad (6.28)$$

$$\ln \langle F_1^{(n)} \rangle \approx a \sum_{k=1}^n \langle \lambda_k \rangle \quad (6.29)$$

$$d \ln \langle F_1^{(n)} \rangle / dn \approx a \langle \lambda_n \rangle. \quad (6.30)$$

The last two equations are obtained by expanding the logarithm and keeping only divergent sums. Both the mean of  $F_1^{(n)}$  and the mean of the sum of  $\lambda_k$  increase as a function of  $n$ . All other sums of powers of  $\lambda_k$  converge as a function of  $n$ : cf. subsection B. Thus, if we assume that  $\langle F_1^{(n)} \rangle \propto n^{1/D}$ , fractal scaling of the radius (see below), implies that [10]

$$\langle \lambda_n \rangle = 1/naD. \quad (6.31)$$

In the next subsection we show that this is indeed supported by the simulations. Note that  $\langle \lambda_n \rangle$  is inversely proportional to  $n$  for any value of the fractal dimension  $D$ . On the other hand, if we assume the property of self-averaging, Eq. (6.31) implies

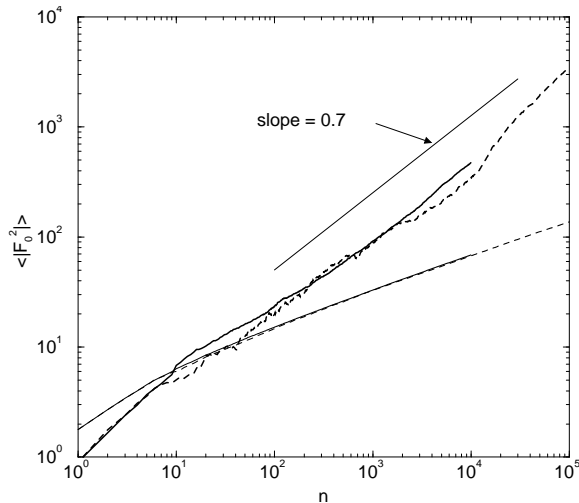


Figure 6.4: The scaling of  $\langle |F_0^{(n)}|^2 \rangle$  (thick lines) and the sum of diagonal terms (thin lines, see Eq.(51)) with size  $n$ . Clearly the two have different scaling exponents. The solid lines are averages over 400 clusters of size 10,000, the dashed lines are averages over 30 clusters of size 100,000.

a relationship between the generalized dimension  $D_3$  and the fractal dimension  $D$ .

Comparing Eqs. (6.25) and (6.31) leads immediately to the relation

$$D_3 = D/2. \quad (6.32)$$

This scaling relation was derived by Halsey [15] using much more elaborate considerations. We see that in the present formalism this scaling relation is obtained very naturally. In fact the present formulation is more powerful since Eq.(6.31) predicts not only the exponent of the third moment of the electric field, but also the prefactor. It is also noteworthy that the scaling relation (6.32) results simply from the existence of a power law behavior for the radius  $F_1^{(n)}$ .

### Scaling of $F_0$

We found the exponent of  $\langle |F_0|^2 \rangle$  to be  $x_0 = 0.7 \pm 0.1$ , see Fig. 6.4. To estimate

the scaling behaviour of  $F_0$  theoretically we note that

$$F_0 = \frac{1}{2\pi} \int_0^{2\pi} \Phi^{(n)}(\theta) d\theta = \frac{1}{2\pi} \int_0^L z(s) |E(s)| ds . \quad (6.33)$$

Accordingly we can write

$$\begin{aligned} \overline{|F_0|^2} &= (1/4\pi^2) \int_0^L ds \int_0^L ds' \overline{z(s)z(s')^* |E(s)||E(s')|} \\ &\sim \lambda_0 R^2 \int_0^L ds \langle |E(s)|^2 \rangle \end{aligned} \quad (6.34)$$

In writing the second line we assumed that the main contribution to the correlation function is short ranged,

$$\langle z(s)z(s')^* |E(s)||E(s')| \rangle \sim \lambda_0 R^2 \overline{|E(s)|^2} \delta(s - s') . \quad (6.35)$$

The justification for this is that the field is expected to exhibit wild variations as we trace the boundary  $z(s)$ . In addition the main contribution to the integral is expected to come from the support of the harmonic measure where the radius is of the order of  $R$ . From the estimate (6.34) and Eq.(6.23) we then find

$$x_0 = \frac{2 - D_2}{D} \approx 0.64 \quad (6.36)$$

in agreement with our measurement of  $x_0$ . (We used here  $D_2 = 0.90$  in correspondence with the numerical finding reported in Section IV C. Any of the values of  $D_2$  quoted in the literature would yield  $x_0$  in the range  $0.7 \pm 0.1$ .)

### Scaling of $F_{-k}$

The exponents  $x_k$  for  $k < 0$  are smaller than  $2/D$  but approach it asymptotically, see Fig. 6.3. This behavior is expected from the area theorem, and also from a direct estimate of the integral representation of the coefficient for large  $k$

$$\begin{aligned} \overline{|F_{-k}|^2} &= \frac{1}{4\pi^2} \int_0^L ds \\ &\times \int_0^L ds' \overline{z(s)z(s')^* |E(s)||E(s')| e^{ik(\theta(s) - \theta(s'))}} . \end{aligned} \quad (6.37)$$

In Appendix B we show that this integral can be estimated using the multifractal formalism of the harmonic measure with the final result

$$\overline{|F_{-k}|^2} \sim (R/4k)^2 \int d\alpha (2k/\pi)^{f(\alpha)/\alpha}, \quad (6.38)$$

where  $\alpha$  and  $f(\alpha)$  are the strength of singularities of the harmonic measure and the dimension of the sets of points that exhibit these singularities respectively [9]. For our purposes the important consequence of Eq.(6.38) is the scaling relation (assuming self-averaging)

$$\langle |F_{-k}|^2 \rangle = \lambda_0 n^{2/D} g(k) \quad (6.39)$$

with  $g(k) \sim 1/k^2 \int d\alpha k^{f(\alpha)/\alpha}$ . One knows from the theory of multifractals that  $f(\alpha)/\alpha \leq 1$ , and therefore we can bound  $g(k)$  from above and from below,  $Ak^{-2} < g(k) < Bk^{-1}$ . This is in accord with our numerical simulations in the range  $3 \leq k \leq 10$ , although the calculation in the appendix is only valid for large values of  $k$ . We found agreement with Eq.(6.26) with  $x_k \rightarrow 2/D$  and  $a_k \sim k^{-\alpha}$  with  $1 < \alpha < 2$ .

Note that this scaling behaviour has important consequences for both the area theorem and for conformality. Absolute convergence of the sum  $\sum_{k=1}^{\infty} k |F_{-k}^{(n)}|^2$  in the area theorem requires  $\alpha > 2$  which is not the case. The situation is even more serious for the existence of conformality. To insure the latter the sum  $\sum_{k=1}^{\infty} k |F_{-k}^{(n)}|$  must exist. This would require  $\alpha > 4$ . The reason that the sums exist in the theory is only due to the ultraviolet cutoff at  $\sqrt{\lambda_0}$ . This cutoff introduces a highest  $k$  in the Laurent expansion which we estimate as  $2\pi k_{max} \approx L/\sqrt{\lambda_0} \sim n$  where  $L$  is the perimeter of the cluster.

#### 6.4.2 Multi-fractal exponents

Here we test Eq.(6.25). In Fig. 6.5 we display double-logarithmic plots of  $\langle \lambda_n^q \rangle$  vs.  $n$  for  $q = 0.5, 1, 1.5, 2, 2.5, 3$  and  $3.5$ . The values of the generalized dimensions

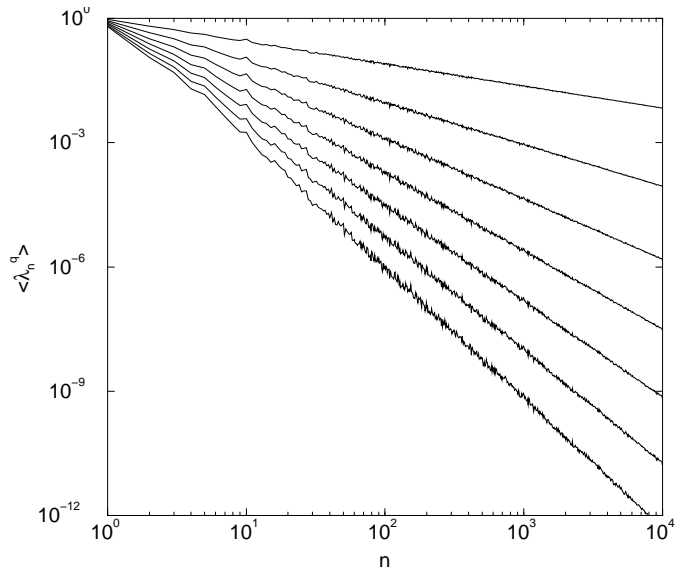


Figure 6.5: Scaling of the moments  $\langle \lambda_n^q \rangle$  with powers of  $n$ . The curves from top to bottom correspond to  $q = 0.5, 1, 1.5, 2, 2.5, 3$  and  $3.5$ . The exponents  $-2qD_{2q+1}/D$  are in agreement with theoretical predictions (see text) and with numerical values for the generalized dimensions in the literature.

$D_q$  obtained from our simulations agree very well (within the uncertainties) with the generalized dimensions  $D_q$  obtained in the past [5] for  $D_2, \dots, D_8$  using standard methods. In addition we reproduce numbers in agreement with the theoretical prediction of  $D_0 = D \approx 1.71$  and  $D_3 = D/2$ . This agreement is a strong indication for self averaging at least for the purpose of computing moments of  $\lambda_n$  (i.e.  $\langle \lambda_n^q \rangle \sim \bar{\lambda}_n^q$ ).

### 6.4.3 Fluctuations of the averages

We previously discussed the scaling behavior of  $|F_{-k}^{(n)}|^2$  and showed that their history averages obey Eq. (6.26). However  $|F_{-k}^{(n)}|$  are random variables with broad scaling distributions. Fig. 6.6 describes the rescaled standard deviation  $\sigma_k^{(n)}$  of the Laurent coefficients,

$$\sigma_k^{(n)} = \sqrt{\langle |F_k^{(n)}|^4 \rangle - \langle |F_k^{(n)}|^2 \rangle^2} / \langle |F_k^{(n)}|^2 \rangle, \quad (6.40)$$

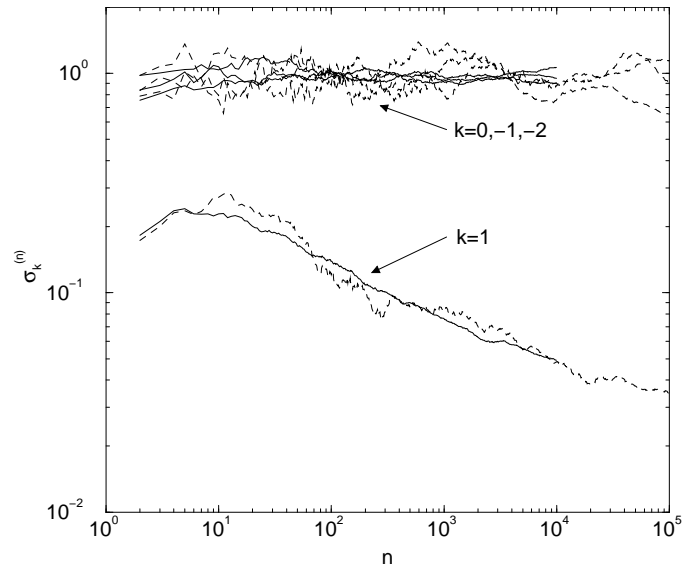


Figure 6.6: The rescaled standard deviation  $\sigma_k^{(n)}$  of the Laurent coefficients of the map (see definition in text). For  $k \neq 1$ ,  $\sigma_k^{(n)}$  fluctuates around unity, corresponding to broad distributions. But for  $k = 1$  it tends to zero as  $n \rightarrow \infty$ , demonstrating the asymptotic sharpness of the distribution of  $F_1$ . The solid lines are averages over 400 clusters of size 10,000, the dashed lines are averages over 30 clusters of size 100,000.

for  $k = 1, 0, -1, -2$  as a function of the cluster size  $n$ . As is seen clearly from the graphs the widths of the distributions for all  $k \leq 0$  tend asymptotically to a finite value. This is the normal behaviour for scaling distributions. The exceptional case is  $k = 1$ . Even though it exhibits a scaling law of the type (6.26) (see Section III), with

$$x_1 = \frac{2}{D} \approx 1.18,$$

the rescaled distribution width of  $|F_1^{(n)}|^2$  tends to zero as  $n$  goes to infinity. This means that the rescaled distribution function of  $F_1^{(n)}$  tends asymptotically to a delta function. The importance of this result for the evaluation of the fractal dimension of the cluster warrants an immediate discussion of this sharpening phenomenon.

The conclusion of the numerics on  $F_1$  is that there exists a universal constant  $c(\lambda_0)$  such that

$$n^{-1/D} F_1^{(n)} \rightarrow c(\lambda_0) \quad (6.41)$$

where  $c(\lambda_0)$  is cluster independent! Moreover, we found that  $c(\lambda_0) = c\sqrt{\lambda_0}$ , which is in accordance with the role played by  $\sqrt{\lambda_0}$  as an ultraviolet inner lengthscale, which is the only lengthscale that appears in the mappings. Note that the constant  $c$  in Eq. (6.41) depends on the parameter  $a$ . We measured  $c$  values of 0.6, 0.87, 1.2 and 1.8 for  $a$  values of  $1/3$ ,  $1/2$ ,  $2/3$  and  $4/5$  respectively.

The observed sharpening is not obvious since we know that  $F_1^{(n)}$  is built from a product of random variables  $\lambda_n$ , whose moments change with  $n$  in multi-fractal manner according to Eq. (6.25).

One could attempt to connect the sharpening of  $F_1^{(n)}$  to the existence of other sharp functions of  $n$ . Considering the full expansion of Eq.(6.27) we find

$$\frac{1}{a} \ln F_1^{(n)} = \sum_{i=1}^n \ln(1 + \lambda_i) \quad (6.42)$$

$$= \sum_{i=1}^n \lambda_i - \frac{1}{2} \sum_{i=1}^n \lambda_i^2 + \frac{1}{3} \sum_{i=1}^n \lambda_i^3 + \dots . \quad (6.43)$$

We could understand Eq. (6.41) easily if all the sums of all the powers of  $\lambda_i$  converged to constants,

$$\sum_{i=1}^n \lambda_i - \frac{2}{D} \ln n \rightarrow c_1 \quad (6.44)$$

$$\sum_{i=1}^n \lambda_i^2 \rightarrow c_2 \quad (6.45)$$

$$\dots \quad (6.46)$$

with  $c_i$  cluster independent. In fact, this is not the case. The sums of powers are not cluster independent. A clear demonstration of this is a simulation which begins with initial conditions which are very far from the circle. The individual sums in Eq. (6.43) are very different from the average values, but nevertheless  $\sum_{i=1}^n \ln(1 + \lambda_i)$  seems to converge to the right value. It is our conclusion that each of the sums in (6.43) is not cluster independent, and yet somehow the resummed form is cluster independent.

This remarkable sharpening calls for further discussion; it appears that its interpretation requires better understanding of the time correlations of the field: an independent choice of random realization of a series of  $\lambda_i$  according to their multifractal distribution can only generate  $F_1^{(n)}$  with the proper scaling exponent but cannot trivially yield a highly peaked distribution of  $F_1^{(n)}$ . Therefore we consider now some evidence for the existence of temporal correlations.

The first outstanding evidence appears in the context of the scaling behavior of  $F_0$ , which was discussed in the first subsection. We show that if we assume that there exist no correlations between different growth stages, the exponent  $x_0$  will be very different from the measured and calculated value. From the recursion relations

of the Laurent coefficients (Eq. 6.14) we can estimate, in the limit of large  $n$  when  $\lambda_n$  is very small on the average,

$$\langle |F_0^{(n)}|^2 \rangle \sim \sum_{m=1}^n \sum_{m'=1}^n \langle F_1^{(m)} F_1^{(m')} \lambda_m \lambda_{m'} e^{i(\theta_m - \theta_{m'})} \rangle \quad (6.47)$$

$$\sim \sum_{m=1}^n \sum_{m'=1}^n \langle F_1^{(m)} F_1^{(m')} \rangle \langle \lambda_m \lambda_{m'} e^{i(\theta_m - \theta_{m'})} \rangle \quad (6.48)$$

The second line is obtained because  $F_1^{(m)}$  is proportional to the radius of the whole cluster and should not be correlated with  $\lambda_m$ . The crucial approximation comes next: if  $\lambda_m$  and  $\lambda_{m'}$  can be treated as independent for  $m \neq m'$ , then (since  $\theta_m$  and  $\theta_{m'}$  are independent) Eq.(6.48) simplifies to

$$\langle \lambda_m \lambda_{m'} e^{i(\theta_m - \theta_{m'})} \rangle \approx \langle \lambda_m^2 \rangle \delta_{m,m'} \quad (6.49)$$

$$\begin{aligned} \langle |F_0^{(n)}|^2 \rangle &\sim \\ &\sum_{m=1}^n \langle (F_1^{(m)})^2 \rangle \langle \lambda_m^2 \rangle \sim n^{1+2/D-4D_5/D} \sim n^{0.3} \end{aligned} \quad (6.50)$$

The numerical simulation resulted in an exponent of the order of 0.7, in serious disagreement with Eq. (6.50). We think that the assumption of independence, Eq. (6.49) is the culprit.

Another fact which illustrates the importance of the time-angle correlation (see Eq. (6.49)) is the difference between the exponents of  $F_0$  and  $F_{-1}$  ( $\langle |F_0|^2 \rangle \sim n^{0.7}$  whereas  $\langle |F_{-1}|^2 \rangle \sim n^{0.9}$ ). Their equations of motion (6.14) differ, for small  $\lambda_n$ , by two terms only. The first one is the term  $\lambda_n F_{-1}^{(n-1)}$  in the RHS of the equation for  $F_{-1}$  which is absent in the equation for  $F_0$ . We checked numerically that neglecting this term leads to a very small change in the exponent. The second difference between is that the term  $\lambda_n \lambda_{n-k} e^{i(\theta_n - \theta_{n-k})}$  in Eq. (6.48) is replaced by  $\lambda_n \lambda_{n-k} e^{2i(\theta_n - \theta_{n-k})}$ . The change in the exponent can therefore be directly attributed to the existence of important time-angle correlations.

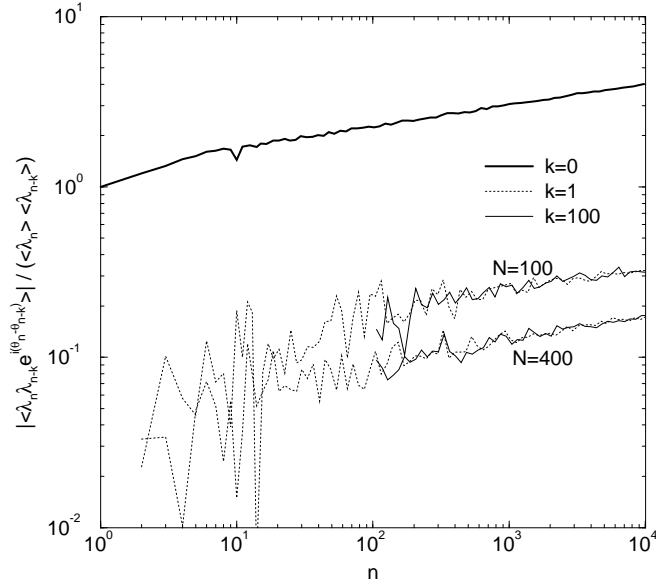


Figure 6.7: Time-angle correlations of the field. In order to reduce statistical noise, the values plotted are averaged in bins  $[n, 1.1n]$ .

We tried to analyze numerically the time-angle correlations  $\langle \lambda_n \lambda_{n-k} e^{i(\theta_n - \theta_{n-k})} \rangle$ . The results for some  $k$ 's are shown in Fig. 6.7. It appears that as we increase the size of the ensemble,  $\langle \lambda_n \lambda_{n-k} e^{i(\theta_n - \theta_{n-k})} \rangle \rightarrow 0$  with the usual  $N^{-1/2}$  dependence on the ensemble size. If we believe these numerical results (doubts may exist due to the relative smallness of the ensemble analyzed), then the previous results must be related to more subtle correlation of higher order nature.

Lastly we would like to discuss the importance of early stages of the growth.  $\langle F_1^{(n)} \rangle$  might be written in the following way

$$\langle F_1^{(n)} \rangle = \left\langle \prod_{i=1}^n (1 + \lambda_i)^a \right\rangle. \quad (6.51)$$

(see Eq. (6.13)). Neglecting the correlations in time in the above product one may approximate

$$\left\langle \prod_{i=1}^n (1 + \lambda_i)^a \right\rangle \approx \prod_{i=1}^n \langle (1 + \lambda_i)^a \rangle. \quad (6.52)$$

Numerical evaluation of the two objects in Eq.(6.52) shows that they differ by a

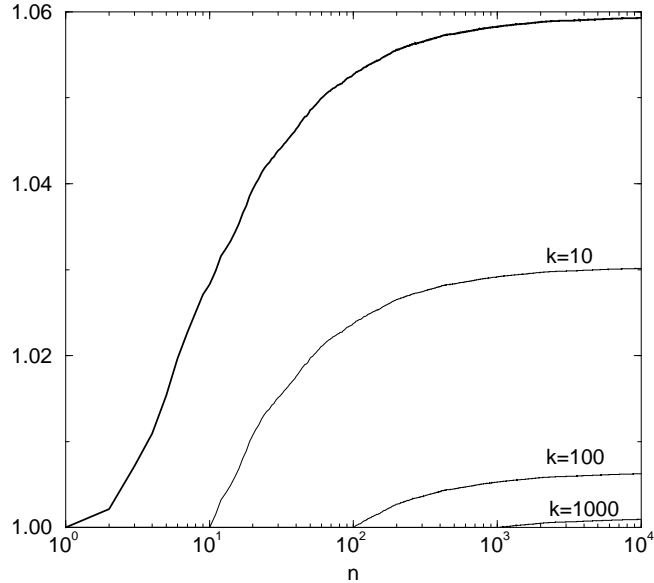


Figure 6.8: The ratio of  $F_1$  with time correlations neglected and the full  $F_1$ :  $\prod_{i=1}^n \langle (1 + \lambda_i)^a \rangle / \langle \prod_{i=1}^n (1 + \lambda_i)^a \rangle$  (thick line). The quantities  $\langle \prod_{i=1}^k (1 + \lambda_i)^a \rangle \prod_{i=k+1}^n \langle (1 + \lambda_i)^a \rangle$  are also plotted for  $k = 10, 100$  and  $1000$ .

few percent (see Fig. 6.8). The numerics indicate the scaling laws

$$\langle \prod_{i=1}^n (1 + \lambda_i)^a \rangle = c \lambda_0 n^{2/D}, \quad (6.53)$$

$$\prod_{i=1}^n \langle (1 + \lambda_i)^a \rangle = c_1 \lambda_0 n^{2/D}, \quad (6.54)$$

where  $c_1/c \geq 1.06$ .

To get further intuition we checked also the object

$$\langle \prod_{i=1}^k (1 + \lambda_i)^a \rangle \prod_{i=k+1}^n \langle (1 + \lambda_i)^a \rangle$$

for various values of  $k$ . The results are shown in Fig. 6.8. As it seems from this graph, time correlations in the initial stages of the growth are much more important than local correlations in the late stages.

We checked also two-point time correlations  $\langle \lambda_n \lambda_{n-k} \rangle$  for some  $k$ 's. The results are plotted in Fig. 6.9. As it turns out from this graph,  $\langle \lambda_n \lambda_{n-k} \rangle \approx \langle \lambda_n \rangle \langle \lambda_{n-k} \rangle$  up to statistical fluctuations.

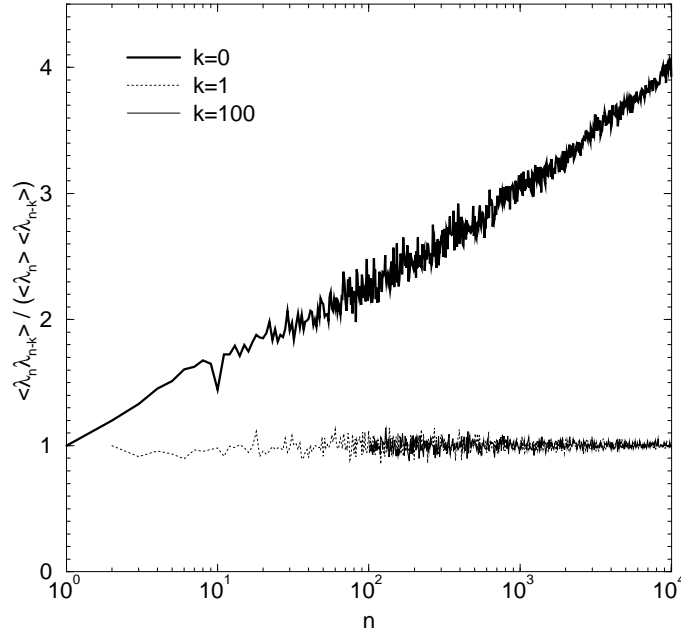


Figure 6.9: Correlations of the field. In order to reduce statistical noise, the values plotted are averaged in bins  $[n, 1.01n]$ .

## 6.5 Summary and discussion

The language proposed by Hastings and Levitov appears to offer many appealing features. It generates DLA clusters in such a way that the conformal map  $\Phi^{(n)}$  from the circle to the boundary of the cluster is known at every instant. In this chapter we examined carefully the numerical procedure used to generate the conformal maps, and pointed out the advantages and the shortcoming of the algorithm.

The new results of this chapter pertain to the scaling behavior of the Laurent coefficients  $|F_k|$  of the conformal map  $\Phi^{(n)}$  and of the moments of  $\lambda_n$  which are related to moments of the field. We presented a theoretical discussion of the exponents characterizing moments of  $|F_k|$  and  $\lambda_n$ . We pointed out the relations to the multifractal analysis of the harmonic measure, and derived scaling relations. Of particular interest is the scaling relation  $D_3 = D/2$  that was derived first by Halsey and which

appears here as a very natural consequence of the formalism.

One important results which is not adequately interpreted in this chapter is the sharpness of the distribution of  $F_1$ . This coefficient is proportional to the radius of the cluster, and its sharpness is directly related to the existence of a universal fractal dimension independently of the details of the shape of the cluster. Understanding the sharpness appears to be connected to understanding the existence of universal fractal dimension, and we believe that it poses a very worthwhile and focussed question for the immediate future.

This work has been supported in part by the Israel Science Foundation founded by the Israel Academy of Sciences and Humanities. LMS and ES are supported by DOE grant DEFG-02-95ER-45546, and would like to thank the Weizmann Institute of Science for hospitality.

## References

- [1] T.A. Witten and L.M. Sander, *Phys. Rev. Lett.* **47**, 1400 (1981).
- [2] L. Niemeyer, L. Pietronero and H.J. Wiessmann, *Phys. Rev. Lett.* **52**, 1033 (1984).
- [3] L. Paterson, *Phys. Rev. Lett.* **52**, 1621 (1984).
- [4] R. M. Brady and R. C. Ball, *Nature* **309**, 225 (1984); D. Grier, E. Ben-Jacob, R. Clarke, and L. M. Sander, *Phys. Rev. Lett.* **56**, 1264 (1986)
- [5] P. Meakin, in *Phase Transitions and Critical Phenomena*, eds. C. Domb and J. L. Lebowitz, Vol.12 (Academic, NY, 1988).
- [6] A. Erzan, L. Pietronero, A. Vespignani, *Rev. Mod. Phys.* **67**, 545 (1995)
- [7] T.C. Halsey, M. Leibig, *Phys. Rev. A* **46**, 7793 (1992); T.C.Halsey, *Phys. Rev. Lett.* **72**, 1228 (1994)
- [8] T.C. Halsey, P. Meakin and I. Procaccia, *Phys. Rev. Lett.* **56**, 854 (1986).
- [9] T.C. Halsey, M.H. Jensen, L.P. Kadanoff, I. Procaccia and B.Shraiman, *Phys. Rev. A* **33**, 1141 (1986).
- [10] M. B. Hastings and L. S. Levitov, *Physica D* **116**, 244 (1998).
- [11] M. B. Hastings, *Phys. Rev. E* **55**, 135 (1997)
- [12] R.C. Ball, and R. M. Brady, *J. Phys. A* **18** L809 (1985); S. Tolman and P. Meakin, *Phys. Rev. A* **40**, 428 (1988).
- [13] P. L. Duren, *Univalent Functions*, (Springer-Verlag, New York, 1983)
- [14] H.G.E. Hentschel and I. Procaccia, *Physica D* **8**, 435 (1983).
- [15] T.C. Halsey, *Phys. Rev. Lett.* **59**, 2067 (1987).

## CHAPTER 7

### Conclusion

In this thesis we investigated various problems in nonequilibrium statistical physics. Common to these problems is that they are all related to pattern formation, and scaling concepts are essential to their thorough understanding. Our methods were mostly discrete: we modeled individual atoms, blocks of material, particles, and studied discretized partial differential equations.

In general, we did not attempt to closely mimic experimental conditions. Rather, we were interested in the basic principles. The exception is the case of epitaxial processes, where our models were closer to experiments—here we were also successful explaining the observations.

To summarize our results, we observed two different scaling regime, depending on growth parameters, in multilayer heteroepitaxial systems. In heteroepitaxial systems we studied how the elastic effects modify the growth process. To better understand the formation of river networks, we proposed a coarse grained theory, which couples the equation of the surface erosion with the conservation law of surface water flow. In the area of Laplacian growth, using diffusion-limited aggregation clusters grown in wedge geometry, we showed the existence of angular building blocks. And finally, using a conformal map approach to DLAs, we studied the relation between the

Laurent coefficients of the map, the generalized dimensions of the harmonic measure and other relevant physical quantities, and their scaling.

## APPENDIX

## APPENDIX A

### Fast off-lattice DLA algorithms

In this Appendix we explain the current best algorithms to simulate off-lattice DLA clusters. The details given here are for the 2-dimensional case, but can be generalized to higher dimensions.

When simulating DLA, in each step a particle is added to the cluster: we have to compute the first contact position of the random walker (or Brownian path) with the cluster using the smallest amount of resources (CPU time, memory) possible.

#### A.1 Efficient random walk

Ideally the walker is released at infinity. However, before it gets in contact with the cluster, it has to cross a circle of arbitrary radius enclosing the cluster, centered around the origin. Suppose we select the smallest circle enclosing the cluster, denoted by  $C$ . Because of symmetry considerations, the first contact point of the walker with this circle is uniformly distributed on the circle. Thus we can model the path of the walker from infinity to the point of first contact to the circle in one step: place it on the circle with uniform probability.

Now suppose that at some point  $P$  on its path the walker is at some distance from the cluster. One can select a bounded region  $D$ , which contains the walker and does

not intersect with the cluster. Before the walker contacts the cluster, it has to come out of this region, specifically there will be a point  $P'$  in the path where it first crosses the boundary of the region. Given the position  $P$  of the walker and the region  $D$ , this segment  $PP'$  of the path is independent of the cluster, and can be in principle calculated in one step. The goal is to select an appropriate region  $D$  such that the distribution of  $P'$  is easily computable. One such choice is a circle centered around  $P$  with radius  $r$  strictly smaller than the distance of  $P$  from the cluster (but the bigger the circle, the more efficient is the simulation). Then  $P'$  would be uniformly distributed on the circle. Given the cluster and  $P$ , an efficient selection of the radius  $r$  is not easy, but a good method will be given later in this Appendix.

An exception from this difficulty is the case when  $P$  is outside the smallest enclosing circle  $C$ : then a quick choice for  $r$  is the distance of  $P$  from the circle. However, if the walker wanders too far away from the cluster then this method becomes inefficient. Early works used to kill the walker when it got too far away (say 5 times the radius of  $C$ ) and start over with a new walker. This solution is not exact (may introduce artificial correlations) and in addition not the most efficient. Instead, we can define an outer circle  $C'$ , also centered around origin but larger than  $C$ . When the walker gets outside  $C'$ , we solve the problem of first contact with  $C$ : place it back to the smallest enclosing circle in one step.

This problem is no longer rotational symmetric as the first-contact-from-infinity case, but solvable[1]. Suppose the radius of  $C$  is  $R_C$ , and the walker is at position  $(r, \theta)$  in polar coordinates, outside  $C'$ . The new position will be at radius  $R_C$  (on circle  $C$ ) and at azimuthal angle

$$\theta' = \theta + 2 \tan^{-1} \left( \frac{r - R_C}{r + R_C} \tan(\pi \mathcal{R}) \right), \quad (\text{A.1})$$

where  $\mathcal{R}$  is a uniform random number from  $[0, 1]$ .

Since this method is exact for any  $C'$  larger than  $C$ , we can optimize the radius of  $C'$  for computational efficiency. In our simulations we used

$$R_{C'} = 1.1 \cdot R_C + 3 \cdot R_{\text{walker}}, \quad (\text{A.2})$$

but the performance did not depend strongly on this selection.

It has to be noted that for simplicity in the above discussion we neglected the radius of the walker. In practice it has to be taken into account, and the size of the jumps need to be decreased, and  $R_C$  increased, by a particle diameter to prevent overlap.

To summarize the procedure we do the following steps to add a particle. First the walker is deposited on the smallest enclosing circle  $C$  with uniform probability. Then it is allowed to take jumps in uncorrelated random directions, where the size of the steps is a lower estimate of the current distance of the walker from the cluster. If at any point it gets outside of the outer circle  $C'$ , then it is redeposited to  $C$  according to Eq. (A.1). However, we do not allow jumps smaller than the particle radius to actually achieve contact: in case the walker overlaps with the cluster after such a jump, it is pulled back on the path of this last jump until just touches the cluster, and becomes part of it.

## A.2 Hierarchical maps

We are still facing the problem of giving a lower estimate of the walker–cluster distance in an efficient way. The naive approach of evaluating the minimum of the  $n$  clusterparticle–walker distances is prohibitively slow: for a cluster of  $n$  particles, each jump of the walker would take  $O(n)$  time, making the overall time complexity at least  $O(n^2)$ .

The technique of hierarchical maps[2] has a better solution: if the walker is “far away” from the cluster, then it provides with a quick lower estimate of the distance without even accessing the coordinates of cluster particles; if the walker is “close” then it provides a list of the nearby particles so that the exact distance can be calculated. The computational time in both cases depends very weakly (logarithmically) on cluster size.

The cluster is put on an adaptively refined square mesh. Each square – which we call *map* –, and possibly its sub-squares, are subdivided into 4 sub-maps (*lower level maps*), if the cluster is “sufficiently close” to it. The rule is the following: initially each map adjacent to the origin is subdivided up to a predefined maximum depth. In addition, when a map on any level contains cluster particles (through its sub-maps), the surrounding 8 maps on the same level must exist, i.e. their parent maps must be subdivided (except when this would go off the mapped area). This has two consequences. First, all particles of the cluster will be in lowest level (smallest) maps; the list of the contained particles is attached to these maps. Second, if a certain (above lowest level) map is not subdivided, then its distance from the cluster is at least half of its side length.

To see this, suppose map  $M$  is above lowest level, and there are particles closer to it than half its side. Then there should be an adjacent (possibly subdivided) map  $M'$  containing particles, one level lower than  $M$ . According to the rule,  $M'$  has to be surrounded by same level maps as itself, therefore  $M$  has to be subdivided.

As the aggregate grows, the maps are updated. Each time a particle is added to a previously empty lowest level map, it and its ancestors are checked whether they satisfy the rule — if not, then the appropriate subdivisions take place.

When a walker lands somewhere, we find the smallest map containing the point.

If it is higher than lowest level, then we are considered to be “far away” from the cluster, and half of the side of the map is a lower estimate of the walker’s distance from the aggregate. If, on the other hand, the walker lands in a lowest level map, then it is “close” to the cluster: the particle lists of the map and of the neighboring lowest level maps are checked to calculate the exact distance of the walker from the aggregate.

The size of the smallest maps is an adjustable parameter, the optimum is around 8 particle diameters. The CPU time used for a single distance estimate is only logarithmically depends on the cluster size: for larger cluster more map levels have to be used. Overall, the memory requirements are linear to the size of the cluster, and the computational time is close to linear (empirically  $time \sim n^{1.1}$  in a range  $10^3$ — $10^7$  particles); the stronger than logarithmic correction is probably due to the fact that for larger cluster the walkers take more jumps.

## References

- [1] E. Sander, L. M. Sander and R. Ziff, *Computers in Physics* **8**, 420 (1994).
- [2] R. C. Ball and R. M. Brady, *J. Phys. A* **18**, L8009 (1985).